

A LEADING ORDER QCD COMPUTATION OF  
 $\pi\pi$  ELASTIC SCATTERING

Thesis by  
Sarbmmeet Singh Kanwal

In Partial Fulfillment of the Requirements  
for the Degree of  
Doctor of Philosophy

California Institute of Technology  
Pasadena, California

1983

(Submitted on November 2, 1982)

- ii -

I wish to dedicate this thesis

to my dear and respected parents

Mr. and Mrs. P. S. Kanwal

and

to the loving memory of my grandmother

"Beji"



## **Acknowledgements**

I would like to take this opportunity to whole heartedly thank my thesis advisor Dr. Geoffrey Fox, who not only suggested this research topic to me in the first place but continued to offer me encouragement and support throughout the duration of the work reported in this thesis. His insight into the relative merit of the various approaches to solving the computational problem was very useful, and discussions with him on the physics of the problem helped me overcome many a stumbling block. I feel that I owe a large part of my success to his able guidance and unflagging moral support.

I would also like to thank my institution, California Institute of Technology, for providing me with the computational facilities, the financial support and the intellectual environment, all of which was vital to the successful completion of my research. My gratitude also extends to my teachers at Caltech, who through various courses taught me physics and inspired me to think about and to investigate the unsolved problems in my chosen area.

I feel the most amount of pleasure in acknowledging the important role played by my friends and my family in helping me get to the long awaited day of the completion of my thesis. My parents, even though they were separated from me by half the circumference of the globe, were an immense source of encouragement and emotional strength all through my stay at Caltech. Their unfailing love and constant support is one factor without which not even a single one of my achievements could have been possible. My brothers Jagmeet and Gurmeet were very generous with their support at times when I most needed it. I can recollect many a time when the successful completion of my thesis seemed hopeless and both of them came to the rescue with their bounties of good cheer.

Eventually, I feel, it was the circle of close friends that I am blessed with that won the battle for me, the battle to finish writing my thesis before a deadline that seemed all but impossible. Their love and warmth and understanding were indeed invaluable to me. I feel very grateful to Madeleine Herold who, each time I felt badly about the progress in my work, was somehow able to convince me that I lead a charmed existence and therefore had nothing to worry about. No amount of thanks can begin to express my feelings toward Duncan Still and Kris Yotter who prayed constantly for my success and were ever willing to give their time when I needed companionship and encouragement. My apartment mate and best friend Michael Weimer proved to be an unending source of encouragement and support to me, and a word of thanks hardly begins to touch the extent of appreciation that I feel for his companionship during these difficult years. Jack and Cecile Wisdom, Kim Aaron, Camille Kunze, Daphne Wilcox, Jeff White, Lloyd Mcaffery, Alan Gates, Norm Bobroff and Rajan Gupta are some of my other friends towards whom I feel a similar sense of gratitude. I wish to thank also our computer operators David Iskander and Norman Wilson who were always willing to answer my questions concerning the working of our Department computer.

## ABSTRACT

This thesis presents the results of a detailed computation of the leading order scattering amplitude and cross-section for the elastic reaction  $\pi^+ \pi^+ \rightarrow \pi^+ \pi^+$ , in the context of the quark model and perturbative QCD. The calculation is based on the recently demonstrated applicability of QCD-factorization and the renormalization group to exclusive hadronic processes at large momentum-transfers. We show that a large fraction of the hard subprocess diagrams have a pinch singularity in them, which means that the amplitude resulting from these diagrams cannot be proved to be short-distance dominated. This contribution to the scattering amplitude is computed separately and, even after including a Sudakov factor, it is shown to be comparable in magnitude to the hard-scattering contribution. We calculate the energy and angular dependence of the pinch contribution and point out that some of the systematic deviations from power-law scaling, observed in high- $P_T$  meson-baryon and baryon-baryon elastic scattering data, can be explained by assuming that the cross-section for these reactions is dominated by pinch, rather than hard, effects. By normalizing the pion distribution amplitude with the help of the pion decay constant, we have also determined the absolute normalization of the  $\pi\pi$  elastic cross-section.

## Table of Contents

<b>Chapter I.</b>	<b>Introduction</b>	<b>1</b>
<b>Chapter II.</b>	<b>High <math>P_T</math> Elastic Hadron Scattering: Review of Theory</b>	<b>5</b>
2.1	The QCD Approach to High $P_T$ Scattering	
2.2	Exclusive Processes in Perturbative QCD	
2.3	High- $P_T$ Elastic Hadron Scattering	
<b>Chapter III.</b>	<b>High <math>P_T</math> Elastic Hadron Scattering: Review of Experiment</b>	<b>55</b>
3.1	Intermediate Energy, Wide Angle Data	
3.2	High Energy, Small Angle Data	
3.3	Concluding Remarks	
<b>Chapter IV.</b>	<b>Results of the <math>\pi\pi</math> Calculation '86'</b>	
4.1	Setting the Stage	
4.2	Fixed Angle Energy Dependence	
4.3	The Normalization for 90° Scattering	
4.4	Angular Dependence at Wide Angles	
4.5	Small Angle Behavior	
<b>Chapter V.</b>	<b>Summary and Conclusions</b>	<b>158</b>
<b>APPENDIX</b>	<b>Details of Method</b>	<b>163</b>
<b>REFERENCES</b>		<b>202</b>

# CHAPTER I

## INTRODUCTION

The last few years of theoretical work in the field of perturbative quantum chromodynamics (QCD) has led to the view that high momentum-transfer exclusive processes are calculable, in the framework of the renormalization group, to the same level of rigor that exists for the calculability of inclusive processes. This development in the theory has provided a firm theoretical basis to the dimensional counting rules of Brodsky and Farrar. These simple rules had long been known to provide a reasonably good description of the energy fall-off of high- $P_T$  data from several different exclusive reactions. The progress in our understanding of these processes has also created the possibility of making and testing detailed predictions of various other features of exclusive scattering, thus opening up a new testing ground for QCD. *The present thesis is an attempt to add to the growing list of detailed predictions emerging from this advancement, and to confront these predictions with existing experimental data.*

Precise and unassailable tests of QCD are as yet lacking, and our faith in the theory rests on a large number of qualitative agreements with spectroscopic and scattering data. This situation is likely to remain unchanged until the non-perturbative domain of the theory yields to a quantitative understanding. In the meantime the best we can do is to broaden the range of phenomenon that show a definite "consistency" with QCD and to keep a look out for experimental observations that can be shown to constitute a clear-cut refutation of the theory. The

opportunities created by the successful application of well established QCD-techniques to exclusive processes are therefore very welcome and should be exploited as far as possible. Moreover, the investigation of exclusive processes promises to throw some light on the short distance structure of hadron wave functions, in a way that is not possible through a study of inclusive phenomenon. A better knowledge of the hadron wave function in the short distance domain could serve as a unifying link between perturbative and non-perturbative treatments of QCD and help make contact with low momentum-transfer reactions, whose understanding lies in the long distance regime of the wave function.

Detailed calculations of the hard subprocesses involved in exclusive reactions are usually more difficult than those for inclusive reactions because these subprocesses usually involve more than two in-going partons. The excess in the number of partons involved in the subprocess leads to a proliferation in the number of diagrams contributing to even the leading order amplitude and adds to the inherent difficulty of computing this subprocess. Because of this problem, detailed calculations of exclusive processes exist only for some elastic and transition form factors and for the two photon reaction ( $\gamma\gamma \rightarrow M\bar{M}$ ), all of which involve the constituents of a single hadron. Unfortunately, the available high- $P_T$  data for these processes are rather limited and usually have large errors, thus preventing a good comparison of theory and experiment. On the other hand there are plenty of accurate data at high momentum-transfers for elastic scattering reactions between pairs of hadrons. Thus, a detailed calculation of the hard subprocesses involved in these reactions should furnish excellent opportunities of testing the predictions of perturbative QCD.

Because of the obvious unavailability of meson targets, experimental data are confined to meson-baryon and baryon-baryon elastic scattering. The leading order amplitudes corresponding to the hard subprocesses for both these cases

involve diagrams numbering in excess of 10,000. Before tackling the task of computing such an enormous number of diagrams, each involving five or six quarks as the case may be, it is advisable to start out with the simpler, but still physically realizable, case of meson-meson scattering. Even though the results of such a calculation cannot be directly compared with experimental data, they can provide a thorough understanding of the complications involved in the calculation of hadron-hadron elastic scattering cross-sections. Hopefully, once the various difficulties and qualitative features of the meson-meson case are identified and understood the calculation of the more complex reactions will be easier and faster. In this thesis we limit ourselves to computing and understanding *same-charge  $\pi\pi$  elastic scattering*, leaving the calculation of  $\pi p$  and  $pp$  elastic scattering to future efforts. As we shall see later, the results of  $\pi\pi$  scattering can be used for making rough extrapolations to  $\pi p$  and  $pp$  scattering, thus allowing us to check if QCD can account for the absolute magnitude and the qualitative behavior of these *measured* elastic cross-sections.

One complication that does not exist in the calculation of hadronic form factors, or of exclusive processes involving photons, is the persistence of a *pinch singularity* in the integrated amplitude. The presence of this soft gluon singularity in the QCD analysis of elastic scattering has been acknowledged for a long time and it is usually presented in its manifestation as a different mechanism of elastic scattering (the multiple scattering mechanism). The diagrams associated with this mechanism are called Landshoff diagrams, after the person who first pointed them out as legitimate contributors to elastic scattering. The multiple scattering mechanism is *not* dominated by short distance interactions and the extent of its contribution to elastic scattering at available energies has been an area of much controversy. A Sudakov factor, obtained by the summation of leading double-logs in the perturbation expansion of the scattering amplitude, is

claimed by many authors to effectively suppress the pinch contribution. However the summation of double-logs in perturbative QCD has been an ill-understood subject and is under intensive investigation even at present. In our calculation we use the most recent understanding of the proper way to incorporate Sudakov effects in an exclusive scattering calculation, and we carefully investigate the effect of the Landshoff mechanism on the  $\pi\pi$  elastic scattering cross-section. The suppression, or lack thereof, of the pinch contribution has very important consequences for the qualitative behavior of the resulting cross-section. *The investigation of this phenomenon and the exploration of its consequences for the resulting cross-section, are perhaps the most important contributions of this project to the understanding of high- $P_T$  elastic hadron scattering.*

The thesis also contains a comprehensive review of the present day theoretical understanding of exclusive hadronic processes, and in particular of elastic scattering, in the context of perturbative QCD. This review brings together the work of several authors on this subject and attempts to put into proper perspective the relationship between Landshoff's multiple scattering mechanism and the pinch singularity encountered in computing the contribution of connected hard-scattering diagrams. The theoretical review is followed by a detailed review of the experimental data on high- $P_T$  elastic scattering. This review critically examines the available data for evidence of power-law scaling, and points out several features which do not uphold the assumption of short-distance dominated constituent scattering. Some of these features have been regularly ignored in the comparison of QCD predictions with experiment, and as we shall see in Chap. IV the results of our calculation could prove instrumental in gaining a better understanding of the source that leads to these features. The final chapter summarizes the conclusions following from our calculation and suggests a path for future investigations.



## CHAPTER II

### HIGH $P_T$ ELASTIC HADRON SCATTERING: REVIEW OF THEORY

In this review, we confine our analysis of elastic hadron scattering to within the context of perturbative quantum chromodynamics. No other approach has proved as universally successful as QCD in understanding high momentum-transfer scattering phenomenon involving hadrons. A short report on alternative approaches can be found in a comprehensive review of high- $P_T$  physics by Sivers *et al.* [1].

#### 2.1. THE QCD APPROACH TO HIGH $P_T$ SCATTERING

##### 2.1.1. INTRODUCTION

The success of using perturbative QCD to analyze high momentum-transfer hadronic scattering processes, whether they be inclusive or exclusive, depends crucially on being able to write the scattering amplitude or cross-section as a product of separate parts, each possessing well defined momentum flow properties. The purpose of this "factorization" is to isolate the hadronic scattering mechanism from the bound state physics of the hadrons. The scattering subprocess that is actually responsible for the transfer of high momentum between the two colliding particles is called the *hard subprocess*. The internal propagators in the Born diagrams for this hard-scattering subprocess are typically off shell by  $O(Q^2)$ ,  $Q^2$  being the invariant associated with the momentum-transfer involved in

the process ( $Q^2 = |(p_f - p_i)^2|$ ). If  $Q^2$  is large enough, then the amplitude for this subprocess has the possibility of being evaluated through a perturbative expansion in the running coupling constant  $\alpha_s(Q^2)$ . The full hadronic cross-section invariably includes other factors which involve, in some way or another, the bound state physics of hadrons and are referred to as *soft parts*. These parts involve internal momenta which are typically of the order of the renormalization scale of the theory and they cannot therefore be completely determined by perturbative methods. However, they do have the property of being *process independent* and can often be extracted from the measurement of one process and used to predict the result of another one. Furthermore, perturbative QCD can be used to analyze the far-off-shell tail of the soft parts, and this leads to a prediction for how they evolve with a change in the  $Q^2$  associated with the scattering process. Such predictions have been used to explain the observed scale breaking of deep inelastic structure functions and to determine the strong interaction scale  $\Lambda$ . Perturbative calculations of the hard subprocess have been used, in some cases, to directly determine  $\alpha_s(Q^2)$  and to verify other properties of the QCD interaction.

We present below a brief discussion of the fundamental basis for the QCD approach used in the analysis of high- $P_T$  hadron scattering.

### 2.1.2. THE PARTON PICTURE

In breaking down the amplitude or cross-section of a high momentum-transfer hadronic process into subprocesses we assume a microscopic picture that was first developed for the naive parton model. A hadron is here viewed as a superposition of Fock states, each consisting of a *finite* number of *on-shell* partons which, in the context of QCD, can be assumed to be quarks and gluons in color singlet combinations. In this picture a hadron interacts with another

particle only through the individual interactions of one or more of its partons with that particle. The parton model further assumes that these interactions can be treated in the same way that we treat the interaction of fundamental bare fields in any renormalizable field theory, e.g. QED, using free-field boundary conditions, even though the quarks and gluons are confined in bound states and cannot be isolated in nature. The asymptotic freedom property of QCD is now used as a justification for this assumption.

To get the final cross-section for a hadronic scattering process we must take into account the information contained in the bound state wave functions of the hadrons involved in the process. If the constituents of a hadron interact coherently in a process, preserving the identity of their parent through the interaction, then the initial and final hadron *wave functions* must be folded into the hard-subprocess amplitude to obtain the final amplitude. If the constituents interact incoherently, resulting in the breaking up of the incoming hadron, then the *probability distribution function* of the struck constituent (obtained by squaring the wave function and integrating over the spectator constituents) must be folded into the hard-subprocess cross-section to obtain the final cross-section. If the process involves the detection of an outgoing hadron produced by the "hadronization" of a parton emerging from the hard-interaction region, then we need to fold into the cross-section the so called *fragmentation function* for this hadron (obtained from the overlap of the hadron wave function with the cascading shower of partons produced by the soft radiation of quarks and gluons from the emerging parton).

We see then, that the parton model assumptions naturally lead to a factorized expression for the scattering cross-section. Fig. 2.1 illustrates this factorization for the single-particle inclusive hadron-hadron scattering process  $AB \rightarrow CX$ . The cross-section can be expressed as follows:

$$d\sigma^{AB \rightarrow CX} = \int_0^1 dx_a dx_b dz_c G_A^a(x_a) G_B^b(x_b) D_C^c(z_c) d\sigma^{ab \rightarrow cd}(x_a, x_b, z_c)$$

where  $G$  represents the distribution function and  $D$  the fragmentation function and  $x_a, x_b, z_c$  are longitudinal momentum fractions on which these functions mainly depend.  $ab \rightarrow cd$  is the underlying hard subprocess which causes the high- $P_T$  event to occur.

### 2.1.3. QCD FACTORIZATION

If QCD is assumed to be the theory that defines the interaction between partons then  $d\sigma^{ab \rightarrow cd}$  should be computable as a sum of Feynman diagrams. However, this sum contains terms like  $\alpha_s(Q^2) \ln(Q^2/m^2)$  which are divergent in the limit of the quark mass  $m$  going to zero, and further theoretical understanding is necessary in order to do a meaningful computation. These divergent terms are generated by the collinear region of the loop integrals in some of the higher order diagrams and should actually belong to the nonperturbative part of the cross-section. This mishap can be corrected by theoretical techniques which involve, successively, the summation of the leading logarithms in the perturbation series, their absorption into the uncalculable soft-subprocess functions and finally the derivation and solution of evolution equations to determine the  $Q^2$ -evolution of these functions. A more formal treatment of this theoretical technique uses the *operator product expansion* and the *renormalization group interpretation*.

These general methods have been rewardingly used, for almost a decade now, to analyze inclusive hadronic processes. In the last few years this approach has been successfully extended to cover high momentum-transfer exclusive processes [2], creating a new range of QCD predictions. Here one needs a deeper

understanding of the hadronic wave function which, till recently, was generally considered to be off-limits to perturbative QCD. In the next section of this chapter, we shall discuss in detail the diagrammatic approach to proving QCD factorization for exclusive processes and the derivation of evolution equations for quark distribution amplitudes associated with hadron wave functions.

## 2.2. EXCLUSIVE PROCESSES IN PERTURBATIVE QCD

### 2.2.1 PARTON MODEL ANALYSIS

As a relatively simple example of an exclusive process, that serves to clarify the application of parton model ideas and QCD factorization to such processes, we shall analyze the elastic hadron form factor. Consider the proton's magnetic form factor  $G_M(Q^2)$  at large  $Q^2$  ( $Q^2 = -q^2$  where  $q$  is the four-momentum transferred to the proton by the virtual photon). In general a baryon has two independent form factors,  $F_1(Q^2)$  and  $F_2(Q^2)$ , but for high momentum-transfers  $F_2$  is suppressed with respect to  $F_1$  by a factor of  $O(m/Q)$  where  $m$  is the quark mass. In the limit  $Q^2 \rightarrow \infty$ , or equivalently  $m \rightarrow 0$ ,  $F_2$  vanishes and the magnetic form factor, which is a linear combination of  $F_1$  and  $F_2$ , becomes identical to  $F_1$ . Then  $G_M(Q^2)$  can be identified with the amplitude for the constituents of the proton to absorb the virtual photon while keeping the proton intact.

Consider the simplest Fock state of the proton which contains only the three valence quarks, all moving roughly parallel with the proton. Let  $T$  be the amplitude for the incoming three-quark state to absorb the photon and produce the three quarks in the outgoing state. Since this amplitude depends on the initial and final momenta of the quarks in addition to the photon momentum  $q$ , we must convolve it with the initial and final proton wave functions in order to get

the final amplitude. The proton wave function  $\psi$  is best expressed in terms of the infinite-momentum frame variables; longitudinal momentum fractions,  $x_i$ , for each of the three quarks, and their transverse momenta,  $k_{\perp i}$ . Then the scalar function  $\psi(x_i, k_{\perp i})$  represents the space-time part of the full hadron wave function. It is assumed that the well known color, flavor, spin and Dirac structure of the full wave function has been absorbed in the amplitude  $T$ . It will be seen later that the more complicated nonvalence Fock states in the proton (i.e.,  $qqqq\bar{q}$ ,  $qqqg$ , . . . ) are unimportant as  $Q^2 \rightarrow \infty$ . Then the proton's magnetic form factor can be written as (see Fig. 2.2a):

$$G_M(Q^2) = \int_0^1 [dx] [dy] \int_{-\infty}^{\infty} [d^2 k_{\perp}] [d^2 l_{\perp}] \psi^*(y_i, l_{\perp i}) T(x_i, y_i, k_{\perp i}, l_{\perp i}, q) \psi(x_i, k_{\perp i}) \quad (2.1a)$$

where

$$[dx] \equiv \delta\left(1 - \sum_{i=1}^3 x_i\right) \prod_{i=1}^3 dx_i \quad (2.1b)$$

and

$$[d^2 k_{\perp}] \equiv 16\pi^3 \delta^{(2)}\left(\sum_{i=1}^3 k_{\perp i}\right) \prod_{i=1}^3 \frac{d^2 k_{\perp i}}{16\pi^3} \quad (2.1c)$$

Being the amplitude for the hard subprocess,  $T$  is expected to have a perturbation expansion in  $\alpha_s(Q^2)$  and it can therefore be analyzed in terms of Feynman diagrams. *The lowest order term in  $T$  is the sum of all tree diagrams in which the spectator quarks are all connected to the struck quark through gluons* (Fig. 2.2b). The connectedness prevents any conditions from having to be imposed on the transverse momenta of the incoming or outgoing quarks and ensures that all the hard momenta are exchanged inside  $T$  and not inside any of

the wave functions.

Intuitively, we expect the wave function  $\psi(x_i, k_{\perp i})$  to be peaked at low  $k_{\perp i}$  since a composite particle has little amplitude for existing while its constituents are flying apart with large transverse momentum. In the *parton model picture* the  $k_{\perp i}$  distribution was, in fact, assumed to be a Gaussian with a width of about 300-500 Mev. Thus for  $|k_{\perp i}| \gtrsim \Lambda$  the integrand is exponentially damped and the important contribution to the integral comes from the region,  $k_{\perp i}^2 \lesssim \Lambda^2$ . If we further assume that, to all orders,  $T$  has no singularities in the region where the constituents become collinear with each other then, for  $Q^2 \gg \Lambda^2$ , we can put  $k_{\perp i}, l_{\perp i} = 0$  in  $T$  since the error introduced is of  $O(\Lambda/Q)$ . The wave functions can now be integrated over their own transverse momentum to give

$$G_M(Q^2) = \int_0^1 [dx] [dy] \varphi^*(y_i) T(x_i, y_i, q) \varphi(x_i), \quad (2.2a)$$

where

$$\varphi(x_i) \equiv \int_{-\infty}^{\infty} [d^2 k_{\perp}] \psi(x_i, k_{\perp i}) \quad (2.2b)$$

with a similar definition for  $\varphi(y_i)$ . Since the color singlet nature of the wave functions prevents any infrared singularities in  $T$ , we can see now that, aside from the UV scale parameter in  $\alpha_s(Q^2)$ ,  $q$  is the only momentum scale in the amplitude. This leads immediately to a *dimensional scaling law* for the proton form factor,  $G_M(Q^2) \propto 1/(Q^2)^2$ , which is consistent with the  $Q^2$ -dependence of the Born term in  $T$  and agrees with the *constituent counting rules* of Brodsky and Farrar.

As we shall see, a rigorous treatment using perturbative QCD, does not support the parton model assumptions. The integral of the wave function over its

transverse momentum is in fact unbounded and the higher order corrections to the Born amplitude for  $T$  have logarithmic divergences as the quarks become collinear. Thus we need a much more careful analysis of these processes to justify and improve the parton model predictions.

It can at least be seen now that nonvalence Fock states in the proton are unimportant since all such states contain four or more constituents, each of which must be turned towards the final direction through the means of a hard gluon in the Born term of  $T$ . Thus the amplitude for these states falls as  $1/(Q^2)^3$  or faster and is negligible relative to the valence contribution as  $Q^2 \rightarrow \infty$ . Thus nonvalence ("sea") quarks and gluons in the proton do not contribute in this limit. Actually this observation is strictly true only in the light-cone gauge. In a general covariant gauge, higher Fock states, containing nonphysical, longitudinally polarized gluons, produce the same  $Q^2$ -dependence in the scattering amplitude as the valence state, and must be included in the form factor. It is possible to overcome this problem by defining an effective valence Fock state which essentially sums all the Fock states contributing to the form factor.

### 2.2.2. THE HADRON WAVE FUNCTION

In order to treat the form factor more rigorously we first analyze the hadron wave function in perturbative QCD. The Bethe-Salpeter equation provides the most systematic way to study a bound state in the context of a renormalizable field theory. It is not possible to solve this equation exactly even for a two-particle bound state, but it enables us to use perturbative QCD to analyze the large transverse momentum tail of the hadron wave function  $\psi(x_i, k_{\perp i})$ , in much the same way that we use it to analyze high momentum-transfer scattering. Since we are taking an approach where the other particles interact with a hadron through its on-shell Fock state constituents the appropriate version of



the Bethe-Salpeter bound state equation to be used for this wave function is the one derived in non-covariant, time-ordered perturbation theory. Since we are assuming both quarks and gluons to be massless it is also advantageous to use light-cone variables and light-cone quantization in these perturbative calculations. The longitudinal momentum fractions  $x_i$ , of the constituents are then defined to be  $x_i = k_i^+ / p^+ = (k_i^0 + k_i^3) / (p^0 + p^3)$ . The bound state equation is

$$\psi(x_i, k_{1i}) = S(x_i, k_{1i}) \int_0^1 [dy] \int_{-\infty}^{\infty} [d^2 l_{1i}] K(x_i, y_i, k_{1i}, l_{1i}) \psi(y_i, l_{1i}) , \quad (2.3a)$$

where  $S$  is the renormalized  $n$ -particle propagator and the kernel  $K$  is the sum of all  $n$ -particle irreducible graphs with  $n$  incoming and  $n$  outgoing legs. If all  $k_{1i}^2$  are large so that  $\alpha_s(k_{1i}^2)$  are small we can organize these graphs into a perturbation expansion for  $K$  in powers of  $\alpha_s$ . The leading-order term in this series is the sum of all one-gluon-exchange graphs. Graphs with a self-energy correction on one constituent line, which are also of leading order, are not needed in  $K$  because they are already included in the renormalized propagator  $S$ .

If we now make the parton model assumptions, i.e.  $\psi(y_i, l_{1i})$  is peaked at low  $l_{1i}$  and  $K$  has a well behaved perturbation series with no collinear singularities in higher order terms, then  $l_{1i}$  can be set to zero in  $K$  and  $\psi(y_i, l_{1i})$  can be replaced by  $\varphi(y_i)$ , as defined by Eq. (2.2b). Then Eq. (2.3a) becomes

$$\psi(x_i, k_{1i}) = S(x_i, k_{1i}) \int_0^1 [dy] K(x_i, y_i, k_{1i}) \varphi(y_i) . \quad (2.3b)$$

Consider first, the simplest case, where  $n=2$ . Then  $S$  and  $K$  depend on only one independent transverse momentum,  $k_{1i}$ , and, either by looking at the one-gluon-exchange graph or by a straightforward dimensional analysis, we immediately get the prediction that  $\psi(x, k_{1i}) \propto 1/(k_{1i}^2)$ . With similar arguments and using

symmetry one can also prove that for the  $n$ -particle case  $\psi(x_i, k_{1i}) \propto 1/(k_{1i}^2)$ . Thus the hadron wave function falls as a power of the quark transverse momentum and not as an exponential as was assumed in the parton model. We still need to correct or justify the assumptions made above but, as we shall see, a rigorous analysis leads only to an additional logarithmic factor and does not change the power-law prediction obtained from the simpler model.

Eq. (2.3a) is a self-consistent integral equation for the  $n$ -particle bound state wave function with  $K$  being given by an infinite series in powers of  $\alpha_s$ . Since we want to treat this equation perturbatively it is important to identify the leading order terms in the kernel. These may not necessarily be limited to the terms with the least power of  $\alpha_s$ . If we are working in a covariant gauge then graphs with higher powers of  $\alpha_s$  have collinear divergences which manifest themselves as powers of  $\ln(k_{1i}^2/m^2)$ . Each such factor tends to cancel one power of  $\alpha_s(k_{1i}^2)$ , effectively reducing the order of the term. The perturbative analysis of  $K$  is made much more transparent and simpler if we work in an axial gauge such as the light-cone gauge. In this gauge the collinear divergences are confined to  $n$ -particle reducible graphs and the terms in the kernel are therefore completely free of these divergences. Thus for a two-particle wave function (see Fig. 2.3), the leading order term in the kernel is the single-gluon-exchange graph which, when iterated through the bound state equation, generates an infinite-rung "ladder" of gluons between the constituent lines of the wave function. Thus perturbative QCD provides us with the leading order structure of the wave function at large transverse momentum.

Having studied the hadron wave function to some extent we can now analyze the perturbation expansion for  $T$ . As mentioned earlier, the higher order terms in this expansion do have collinear divergences which tend to spoil the convergence of the series. If, however, we work again in the light-cone gauge, then the

only graphs in  $T$  which have these divergences are the ones which are  $n$ -particle reducible on either side of the photon vertex. For example, in the two-particle case, all the graphs which have a ladder structure with two or more gluon-rungs between the constituent lines, are collinear-divergent. As a result their contribution is of the same order as the one-gluon Born term and therefore cannot be ignored in the leading order calculation of the form factor at large  $Q^2$ . But we now see that the extra gluons in the ladder graph can be absorbed into either of the two wave functions since the wave functions satisfy the bound state equation to leading order in perturbation theory. This means that the contribution of the reducible graphs to the perturbation expansion of  $T$  is already accounted for by the structure of the hadron wave function. Therefore we can redefine  $T$  to consist only of two-particle irreducible graphs. This reduced amplitude, henceforth denoted by  $T_H$ , is called the *hard-scattering amplitude* because it is free of soft and collinear divergences and is dominated by the far-off-shell region of the internal propagator momenta. We shall see later that, that part of the contribution from reducible graphs which comes from the non-collinear region of loop integration can still be retained in  $T_H$ . One way to rephrase the substitution of  $T_H$  for  $T$  is to say that the leading logarithms in the perturbation series for  $T$ , that come from the non-perturbative near-on-shell region of the internal propagator momenta, have been summed and absorbed into the "bare" wave function, which then obeys the integral equation (2.3a) with  $K$  replaced by the one-gluon-exchange kernel.

### 2.2.3. THE QUARK DISTRIBUTION AMPLITUDE

Having analyzed the wave function and the hard subprocess amplitude we can now go back to a more rigorous treatment of the proton form factor. For the sake of simplicity let us look instead at the pion form factor, where the wave function depends on only two independent variables,  $x$  and  $k_\perp$  of the quark. The momentum of the anti-quark is then given by  $(1-x)$  and  $-k_\perp$ . In analogy to the case of the proton, (Eq. 2.1a), and with  $T$  replaced by  $T_H$ , we have

$$F_\pi(Q^2) = \int_0^1 dx dy \int_{-\infty}^{\infty} \frac{d^2 k_\perp d^2 l_\perp}{(16\pi^3)^2} \psi^*(y, l_\perp) T_H(x, y, k_\perp, l_\perp, q) \psi(x, k_\perp) . \quad (2.4)$$

We would still like to do away with the transverse momenta integrals so that we do not have to deal with the unknown  $k_\perp$ -distribution in the near-collinear region, and also so that we can concentrate on the dependence of  $T_H$  on the momentum scale set by  $q$ . As shown in Sec. 2.2.2,  $\psi(x, k_\perp) \propto 1/k_\perp^2$  (modulo logarithms) and therefore the integral of  $\psi(x, k_\perp)$  over  $|k_\perp|$  is no longer bounded but diverges logarithmically with its upper limit. If we now examine the Born term of  $T$  we find that it can provide further damping of the integrand at large  $|k_\perp|$  through its denominator which, for the diagram with the photon hitting the quark, has a factor of the form  $[(1-x)q_\perp + k_\perp]$ , where  $q_\perp$  is the component of  $q$  transverse to the direction of the incident pion. Thus for  $|k_\perp| \gg Q$ , ( $q_\perp^2 = Q^2$ ), the integrand falls with a higher power of the transverse momentum than was the case with the wave function. The transition in the power of the fall-off with  $|k_\perp|$  takes place around  $|k_\perp| = (1-x)Q$  and one way to express this  $Q$ -dependence of the integral is to carry it out to the finite upper limit,  $(1-x)Q$ . The error made in this approximation can be shown to be of  $O(1/\ln Q^2)$  when the logarithmic factors in the  $k_\perp$ -dependence of  $\psi(x, k_\perp)$  are included. This correction is therefore of higher order in  $\alpha_s(Q^2)$ . Furthermore, provided the region,  $x \sim 1$ , does not result

in a singularity in the amplitude,  $(1-x)Q$  can be replaced by  $Q$  to leading order accuracy. The  $l_1$ -integral in Eq. (2.4) can be treated in the same way as the  $k_1$ -integral.

The hadron wave function is still peaked at small transverse momenta,  $|k_1| \lesssim \Lambda$ , and having used the large  $k_1$  behavior of  $T_H$  to cut off the integral at  $Q$ , we can again make the approximation of setting  $k_1, l_1 = 0$  in  $T_H$ . This is now safe to do because  $T_H$  is free of collinear divergences. The error introduced because of this approximation is of  $O(\Lambda/Q)$ . The pion form factor can now be rewritten as

$$F_\pi(Q^2) = \int_0^1 dx dy \varphi^*(y, Q^2) T_H(x, y, Q^2) \varphi(x, Q^2), \quad (2.5a)$$

where

$$\varphi(x, Q^2) \equiv \int_0^{Q^2} \frac{dk_1^2}{16\pi^2} \psi(x, k_1) \quad (2.5b)$$

and a similar definition holds for  $\varphi(y, Q^2)$ . In general, for a hadron with  $n$  constituents,  $\varphi(x_i, Q^2)$  is defined as the integral of  $\psi(x_i, k_{1i})$  over all  $k_{1i}$  up to the same upper limit  $Q^2$  and is called the quark *distribution amplitude*. It is the amplitude for finding the constituents with longitudinal momentum fractions  $x_i$ , in the hadron, which are all collinear up to the scale  $Q$ .

#### 2.2.4. THE $Q^2$ -EVOLUTION EQUATION

We are now in a position to see the approximate validity of the dimensional scaling law for the pion form factor and also to determine the modification caused by the detailed structure of perturbative QCD. The dependence of  $T_H$  on  $Q^2$  follows immediately because of the absence of any other mass-scale in it.

Counting dimensions,  $T_H \propto 1/Q^2$ , except for the logarithms coming from the coupling constant  $\alpha_s(Q^2)$ . The formalism developed so far is also sufficient to determine the logarithmic modification caused by the  $Q^2$ -evolution of the quark distribution amplitudes. In order to derive an evolution equation for the distribution amplitude we must go back to the bound state equation for the wave function. We consider the case of the two particle wave function and we make the replacement  $k_1 \rightarrow q_1$ . Then Eq. (2.3a) becomes

$$\psi(x, q_1) = S(x, q_1) \int_0^1 dy \int_{-\infty}^{\infty} \frac{d^2 l_1}{16\pi^3} K(x, y, q_1, l_1) \psi(y, l_1). \quad (2.6)$$

We can now approximate the transverse momentum integral in this equation in exactly the same way that we used for the pion form factor equation. The kernel  $K$  now provides additional damping of the integrand for  $l_1 \gg q_1$ , and we can truncate the  $l_1$ -integral at  $l_1^2 = q_1^2 = Q^2$ . We can then put  $l_1 = 0$  in  $K$  since it is known to be collinear-finite. The errors involved in these approximations are of  $O[\alpha_s(Q^2)]$  and  $O(\Lambda/Q)$  respectively. The bound state equation then becomes

$$\psi(x, q_1) = S(x, Q^2) \int_0^1 dy K(x, y, Q^2) \varphi(y, Q^2)$$

which can be rewritten as

$$\psi(x, q_1) = 8\pi \frac{\alpha_s(Q^2)}{Q^2} \int_0^1 dy V(x, y) \varphi(y, Q^2), \quad (2.7)$$

where  $V(x, y)$  is the  $Q^2$ -independent part of the the product  $SK$ .  $V(x, y)$ , in fact, describes the amplitude for a collinear  $q\bar{q}$  pair with momentum fractions  $y$  and  $1-y$  to evolve by gluon exchange into a collinear  $q\bar{q}$  pair with fractions  $x$  and  $1-x$ . If  $q_1^2 \gg \Lambda^2$  then the leading order term in the perturbative expansion of

$V(x,y)$  is determined by the one-gluon-exchange kernel and the renormalized two-particle propagator. If we identify  $V(x,y)$  with its Born contribution then it can be shown to be given by

$$V(x,y) = C_F \left\{ \frac{1-y}{1-x} \left( 1 + \frac{1}{x-y} \right) \theta(x-y) + \frac{x}{y} \left( 1 + \frac{1}{y-x} \right) \theta(y-x) \right\}_+ \quad (2.8)$$

where the "+" function" is defined in a way similar to the one used for the Altarelli-Parisi functions, which arise in the evolution equations for quark and gluon probability distributions in a hadron. By definition

$$\int_0^1 dy ( )_+ \varphi(y, Q^2) \equiv \int_0^1 dy ( ) [\varphi(y, Q^2) - \varphi(x, Q^2)] .$$

The "+" function" serves to regularize the singularity that would otherwise occur in  $V(x,y)$  at  $x=y$ , but is now canceled by a contribution arising from self-energy corrections to the quark and anti-quark propagators (which occur only at  $x=y$ ). These self-energy graphs are present in  $V(x,y)$  because of the inclusion of the renormalized propagator  $S$  in its definition.

From the definition, (2.5b), of the distribution amplitude we have,

$$\frac{\partial}{\partial Q^2} \varphi(x, Q^2) = \frac{\psi(x, Q)}{16\pi^2} .$$

Since, in all our applications,  $Q^2 \gg \Lambda^2$ , we can use Eq. (2.7) to substitute for  $\psi(x, Q)$  in the above equation. We then finally arrive at the evolution equation that the distribution amplitude,  $\varphi(x, Q^2)$ , must satisfy if the wave function is described by the bound state equation. The evolution equation is

$$Q^2 \frac{\partial}{\partial Q^2} \varphi(x, Q^2) = \frac{\alpha_s(Q^2)}{2\pi} \int_0^1 dy V(x,y) \varphi(y, Q^2) . \quad (2.9)$$

If we approximate  $V(x,y)$  by the lowest order term in its expansion, which is given by Eq. (2.8), then the above differential equation can be solved exactly for  $\varphi(x, Q^2)$  in terms of an initial condition  $\varphi(x, Q_0^2)$  at some reference momentum  $Q_0$ . Both  $Q^2$  and  $Q_0^2$  must be large so that the higher order corrections are small.

We sketch here, very briefly and without any attempt at mathematical rigor, the method used for the solution of this equation. We first expand  $\varphi(x, Q^2)$  on the basis provided by Gegenbauer polynomials of order  $3/2$ .  $[x(1-x)]$  is the appropriate weight function for the chosen argument,  $[x-(1-x)]$ , of the polynomials. Then we have

$$\varphi(x, Q^2) = x(1-x) \sum_{n=0}^{\infty} \varphi_n(Q^2) G_n^{3/2}(2x-1), \quad (2.10)$$

where the coefficients  $\varphi_n(Q^2)$ , also called Gegenbauer moments, can be determined by inverting the above equation using the orthogonality of the polynomials. This expansion results in a set of differential equations for the  $\varphi_n(Q^2)$ 's which can be easily solved to give

$$\varphi_n(Q^2) = \left[ \frac{\alpha_s(Q^2)}{\alpha_s(Q_0^2)} \right]^{d_n} \varphi_n(Q_0^2), \quad (2.11)$$

where

$$d_n \equiv -\frac{2A_n^{\text{NS}}}{\beta_0}.$$

Here  $A_n^{\text{NS}}$  are the familiar non-singlet anomalous dimensions first encountered in the  $Q^2$ -evolution of non-singlet quark distributions  $G_{p \rightarrow q_i}^{\text{NS}}(x, Q^2)$  in deep inelastic scattering. The final solution for  $\varphi(x, Q^2)$  can now be written as



$$\varphi(x, Q^2) = x(1-x) \sum_{n=0}^{\infty} \left[ \frac{\alpha_s(Q^2)}{\alpha_s(Q_0^2)} \right]^{d_n} G_n^{3/2}(2x-1) \varphi_n(Q_0^2), \quad (2.12)$$

where

$$\varphi_n(Q_0^2) = \frac{4(2n+3)}{(n+1)(n+2)} \int_0^1 dx G_n^{3/2}(2x-1) \varphi(x, Q_0^2). \quad (2.13)$$

Thus given the wave function,  $\varphi(x, Q_0^2)$ , at some  $Q_0^2$ , one can compute it at any other  $Q^2$  provided one knows the UV scale parameter  $\Lambda$ . In Eq. (2.12), except for  $n=0$ , in which case  $d_0=0$ , all terms die off like fractional powers of  $\alpha_s(Q^2)/\alpha_s(Q_0^2) = \ln(Q_0^2/\Lambda^2)/\ln(Q^2/\Lambda^2)$  (e.g.  $d_1=0.427$  with  $n_f=4$ ). In general, for all such evolution equations  $d_n > d_0$  for all  $n$ . This means that as  $Q^2$  becomes much larger than  $Q_0^2$ ,  $\varphi(x, Q^2)$  approaches the first term in the infinite series, and is given by

$$\begin{aligned} \varphi(x, Q^2) &= x(1-x) \left[ \frac{\ln(Q_0^2/\Lambda^2)}{\ln(Q^2/\Lambda^2)} \right]^{d_0} \varphi_0(Q_0^2) \\ &= x(1-x) \varphi_0(Q_0^2), \end{aligned} \quad (2.14)$$

where we have used the property,  $G_0^{3/2}(x)=1$ , of Gegenbauer polynomials. The approach to this limiting expression for  $\varphi(x, Q^2)$  is, however, extremely slow and needs a much larger  $Q^2$  than is presently available.

In general  $\varphi(x, Q_0^2)$  is an unknown function essentially non-perturbative in its character. However, if we take a hint from Eq. (2.14) and assume that it has the particularly simple form, given by

$$\varphi(x, Q_0^2) = c_\pi x(1-x), \quad (2.15)$$

then from Eq. (2.13) we see that

$$\varphi_n(Q^2) = \begin{cases} c_n & \text{for } n=0 \\ 0 & \text{for } n>0 \end{cases} \quad (2.16)$$

For this choice  $\varphi(x, Q^2)$  does not evolve with  $Q^2$  even if we retain all the terms in the Gegenbauer series and is given by

$$\varphi(x, Q^2) = c_\pi x(1-x) . \quad (2.17)$$

Since this distribution amplitude is involved in the decay of a pion into leptons, we can use the pion decay constant to determine  $c_\pi$ . The pion form factor is then completely determined in this  $Q^2 \rightarrow \infty$  limit. To first order in  $\alpha_s$  it is given by,

$$F_\pi(Q^2) = 8\pi f_\pi^2 \frac{\alpha_s(Q^2)}{Q^2} . \quad (2.18)$$

## 2.2.5. END-POINT SINGULARITIES

The above analysis has shown the hard-scattering amplitude,  $T_H$ , to be free of soft and collinear divergences that arise from loop integrals in higher order terms. However, the integration of  $T_H$  over the longitudinal momentum fractions of the constituents may still lead to singularities in the final amplitude. The Born contribution to  $T_H$  for the pion form factor can be shown to be

$$T_H(x, y, Q^2) = \frac{16\pi C_F \alpha_s(Q^2)}{Q^2} \left[ \frac{e_q}{(1-x)(1-y)} + \frac{e_{\bar{q}}}{xy} \right] \quad (2.19)$$

where  $e_q$  and  $e_{\bar{q}}$  are the charges carried by the quark and anti-quark. For the case of the photon hitting the quark, the amplitude blows up at the end-points,

$x=1$  and  $y=1$ , of the intervals of integration. This singularity in the amplitude is a result of the gluon propagator, in the Born diagram, going on shell. In the end-point region the quark, which absorbs the photon, carries almost all the longitudinal momentum of the pion. The gluon, that connects the two constituents, does not need to transfer large transverse momentum to the anti-quark to make it collinear with the direction of motion of the final state pion. Thus the gluon becomes either soft or collinear, causing the amplitude to diverge. We need to study the contribution from this singularity more carefully.

Note that  $(1-x)Q$  is a measure of the transverse momentum that must flow from the quark to the anti-quark. As long as  $(1-x)Q \gg \Lambda$ , the whole perturbative analysis, which allows the factorization of soft and hard parts, is still valid. As was pointed out in Sec. 2.2.3, the momentum scale that goes into the argument of the distribution amplitude is in fact  $(1-x)Q$  and not  $Q$ . The same is true for the argument of the running coupling constant. Integration of  $T_H$  over this factorizable regime,  $1 < (1-x) \ll \Lambda/Q$ , has the potential to generate an additional logarithmic factor,  $\ln(Q/\Lambda)$ , in the leading order form factor result. However, it can be shown by a perturbative analysis of the Bethe-Salpeter bound state equation in the region  $x \sim 1$ , that the pion distribution amplitude vanishes as  $x \rightarrow 1$ ; specifically,  $\varphi(x, Q^2) \sim (1-x)^{\varepsilon(Q^2)}$ , with  $\varepsilon(Q^2) > 0$ , irrespective of the initial condition  $\varphi(x, Q_0^2)$ . Furthermore, we can see from Eq. (2.14) that, as a consequence of the evolution equation,  $\varepsilon(Q^2) \rightarrow 1$  as  $Q^2 \rightarrow \infty$ . Thus the presence of the distribution amplitudes in the integrand eliminates the possibility of a logarithmic factor from the region  $1 \ll (1-x)$  or  $(1-y) \ll \Lambda/Q$ . The same can be shown to be true in the case of a baryon form factor.

In the end-point region,  $(1-x) \lesssim \Lambda/Q$ , so that large transverse momentum does not flow through the gluon connecting the two constituents and the perturbative analysis used for the derivation of Eq. (2.19) is no longer obviously valid.

Furthermore, the  $1/Q^2$  suppression from the hard gluon propagator is now expected to be absent from the amplitude. The contribution from this region of integration could be significant and must therefore be analyzed separately. For this analysis it is best to absorb the soft or near-collinear gluon connecting the two constituents into the closest wave function so that, in leading order, the fast constituent alone absorbs all the momentum of the photon while the slow one acts as a mere spectator. To this lowest order then, the form factor can be expressed purely as a convolution of the initial and final wave functions. Using this representation for the *whole* range of momentum fractions, the form factor becomes (see Fig. 2.4a):

$$F_{\pi}(Q^2) = \int_0^1 dx \int_{-\infty}^{\infty} \frac{d^2 k_{\perp}}{16\pi^3} \psi^*(x, k_{\perp} + (1-x)q_{\perp}) \psi(x, k_{\perp}) , \quad (2.20)$$

where, as before,  $q_{\perp}$  is the component of the photon momentum transverse to the incident pion. In this representation all gluon corrections which can be separated away from the photon vertex are considered to be buried in either of the two wave functions which still obey the bound state equation (2.3a).

As an aside, we can now see that, when  $(1-x)Q \gg \Lambda$ , the constituents in at least one of the wave functions are constrained to have large transverse momentum. Then, since  $\psi(x, k_{\perp}) \propto 1/k_{\perp}^2$ , the amplitude falls with  $Q$  as  $1/Q^2$ . Furthermore, the bound state equation can be used to separate out one or more of the hard gluons ( $k_{\perp}^2 \sim (1-x)^2 Q^2$ ) in the wave functions, so that the pion constituents no longer have any constraints on their transverse momentum. Since only those gluons that contribute to imparting large transverse momentum to the constituents are to be extracted out of the wave functions, the loop momenta involved in the resulting ladder diagrams must be restricted to be greater than  $Q$ , so that all gluons extracted remain hard. This analysis, together with gluon

corrections to the photon vertex, results in building up the hard scattering amplitude,  $T_H$ , and leaves behind, the  $Q^2$ -dependent distribution amplitudes. This is a slightly different but equivalent way to derive the factorized amplitude of Eq. (2.5a).

In the end-point region, where  $(1-x)Q \lesssim \Lambda$ , the amplitude falls as  $1/k_1^4$  and the integral over the transverse momentum is then convergent for all  $k_1$ . It is therefore dominated by the near-collinear region ( $|k_1| \lesssim \Lambda$ ) of both wave functions, and we need no longer define a distribution amplitude to do away with the explicit  $k_1$ -integral. Instead we can approximate this integral by replacing  $|k_1| = \Lambda$  in the wave functions. Thus the contribution to the form factor from the end-point region is governed only by the  $x$  behavior of  $\psi(x, \Lambda)$  as  $x \rightarrow 1$ , i.e.

$$\begin{aligned} \Delta F_\pi(Q^2) &\sim \int_{1-\Lambda/Q}^1 dx |\psi(x, \Lambda)|^2 \\ &\rightarrow (\Lambda/Q)^{1+2\delta}, \end{aligned} \tag{2.21}$$

where  $\psi(x, \Lambda) \sim (1-x)^\delta$  as  $x \rightarrow 1$ .

In time-ordered, light-cone perturbation theory, in place of the Feynman propagators for internal lines, we have "energy denominators", where the energy used is the "light-cone energy"  $k^- = k^0 - k^3 = (k_1^2 + m^2)/k^+$ . The magnitude of these denominators is analogous to the "off-shellness" of the internal lines in covariant perturbation theory, and provides the scale for the argument of the running coupling constant relevant to the diagram. For a one-gluon-exchange kernel in light-cone perturbation theory, with the gluon traveling from anti-quark to quark, the "off-shellness" is approximately given by  $k_1^2/(1-x)$ . Therefore, even though  $k_1^2$  ( $\sim \Lambda^2$ ) is small in the region  $(1-x) \lesssim \Lambda/Q$ , the off-shellness is

typically  $\Lambda^2/(\Lambda/Q)=\Lambda Q$ , and is large for large  $Q$ . This enables us to analyze the end-point region perturbatively in a way similar to the hard scattering region. The kernel in the end-point region can be organized in a power series in  $\alpha_s(\Lambda Q)$ . Then, to leading order, the wave function can be represented by a convolution of itself with the one-gluon-exchange kernel. This kernel vanishes linearly as  $x \rightarrow 1$ , and the wave function in this region can then be approximated by

$$\psi(x, k_1) \propto \alpha_s(\Lambda Q) \frac{(1-x)}{k_1^2 + \Lambda^2}.$$

This implies that  $\delta=1$ , and thus the contribution to the form factor from the end-point region is suppressed, compared to the hard scattering contribution, by a factor of  $\alpha_s(\Lambda Q)(\Lambda/Q)$ , making it negligible. Higher order corrections to the kernel result only in the modification of the leading order  $x$  dependence of  $\psi(x, k_1)$  by factors of  $[\ln(1-x)]^n$ . The end-point contribution to the baryon form factor can also be shown to be similarly suppressed; in this case by a factor of  $\alpha_s^2(\Lambda Q)$ .

In writing Eq. (2.20) to analyze the end-point contribution to the form factor, we ignored the higher order corrections to the photon-quark vertex. Since the renormalization group approach is no longer applicable these corrections are not obviously small. The most important contributions come from radiative corrections involving only the struck quark (Fig. 2.4b). The off-shellness of the struck quark is given by  $\Delta^2 \sim \Lambda^2/(1-x) \sim \Lambda Q \ll Q^2$ , and the soft and collinear divergences encountered in each loop integration result in double logarithmic factors of  $\ln^2(Q^2/\Delta^2) \sim \ln^2(Q/\Lambda)$ . As pointed out earlier, it is no longer possible to absorb the collinear divergences into factorized distribution amplitudes. Furthermore, the cancellation of soft divergences in the vertex corrections, against similar divergences coming from other diagrams (a result of the hadrons

being color singlets), is no longer true in the end-point region. Notice that a gluon joining the struck quark to a spectator quark (Fig. 2.4c) must transfer finite longitudinal momentum to it if the loop integral is to result in a soft-logarithm. This forces the amplitude to move away from the end-point singularity, thereby killing the logarithm which would otherwise cancel the one coming from the vertex correction. These double logarithms, then, persist at each order of the calculation and seem to spoil the convergence of the perturbation series. However, it is well known that the logarithms from successive orders of the vertex correction combine to produce the so called Sudakov factor, which in this case works out to be  $\exp[-(\alpha_s(\Lambda Q)/2\pi)\ln^2(Q/\Lambda)]$ . This factor, after simplification, is equivalent to  $(\Lambda/Q)^{2/\beta_0}$  and causes further suppression of the end-point contribution.

## 2.3. HIGH- $P_T$ ELASTIC HADRON SCATTERING

### 2.3.1. DIMENSIONAL SCALING LAWS

The techniques developed in the previous sections can be applied to a study of exclusive hadron-hadron scattering. The cross-section for the case of a two-particle final state,  $AB \rightarrow CD$ , depends solely on the Mandelstam invariants  $s$  and  $t$ . We can study this cross-section perturbatively in the limit  $s \rightarrow \infty$  at fixed  $t/s$  or equivalently, fixed center-of-mass angle,  $\theta_{c.m.}$  ( $\cos\theta_{c.m.} = 1 + 2t/s$ ). Since  $t/s$  is fixed, the large  $s$  limit is also the high momentum transfer limit of the scattering. The momentum transferred from a quark in one hadron to a quark in the other has to be distributed amongst the other valence quarks in order to form the final state hadrons. This necessitates a hard gluon interaction between the quarks of each hadron and allows us to factor out a perturbative hard scattering

amplitude,  $T_H$ , by absorbing the collinear divergences into the distribution amplitudes associated with each hadron. The final amplitude is a convolution of  $T_H$  with the four distribution amplitudes and can be written as (Fig. 2.5a):

$$M_{AB \rightarrow CD}(s, \theta_{c.m.}) = \int_0^1 [dx_a][dx_b][dx_c][dx_d] \varphi_C^*(x_c, Q^2) \varphi_D^*(x_d, Q^2) \\ \times T_H(x_a, x_b, x_c, x_d, s, \theta_{c.m.}) \varphi_A(x_a, Q^2) \varphi_B(x_b, Q^2) \quad (2.22)$$

where  $x_a, \dots, x_d$  represent *sets* of momentum fractions ( $x_a = [x_{a1}, x_{a2}, \dots]$ ) corresponding to the sets of valence quarks in each of the hadrons  $A, \dots, D$ , and  $[dx_a], \dots, [dx_d]$  are defined as in Eq. (2.1b). To leading order accuracy, we can take  $Q^2$  to be given by

$$Q^2 = -t = \frac{s}{2}(1 - \cos \theta_{c.m.}).$$

In leading order,  $T_H$  is the sum of all connected tree diagrams in which each hadron is replaced by collinear valence quarks (Fig. 2.5b). The connectedness is necessary so that the quarks belonging to each of the final state hadrons can rearrange themselves to be collinear after having absorbed large transverse momentum through the inter-hadron interaction. Since  $T_H$  is free of soft and collinear divergences to all orders and, at fixed angle, depends on only one momentum scale,  $s$  (ignoring the dependence on the running coupling constant), its dependence on this scale can be immediately determined by counting dimensions. As  $s \rightarrow \infty$  with  $\theta_{c.m.}$  fixed, it follows that

$$T_H \propto \frac{1}{s^{n/2-2}} \quad (2.23)$$



where  $n = n_A + n_B + n_C + n_D$  is the total number of constituents in the initial and final states together. The evolution of each of the distribution amplitudes in Eq. (2.22), with  $Q^2$ , is completely determined by evolution equations similar to Eq. (2.9). As  $s \rightarrow \infty$  these amplitudes tend to their asymptotic forms, as in Eq (2.14) for the pion amplitude. Then, in this limit, the leading order contribution to the cross-section can be written down as:

$$\frac{d\sigma}{dt}_{AB \rightarrow CD}(s, \theta_{c.m.}) = \left[ \frac{\alpha_s(Q^2)}{s} \right]^{n-2} \left[ \ln \frac{Q^2}{\Lambda^2} \right]^{-2(d_0^A + d_0^B + d_0^C + d_0^D)} f(\theta_{c.m.}) . \quad (2.24)$$

If  $s$  is not large enough for the asymptotic form of the distribution amplitudes to be valid, then we need to replace them with the full series solution like the one obtained in Eq. (2.12) for the case of the pion. The modification caused to the power-law dependence on  $s$  is *still* only through a multiplicative, slowly varying (logarithmic) function of  $s$ .

This analysis provides a rigorous basis for the dimensional counting rules predicted by Brodsky and Farrar and also determines the logarithmic modification to the power-law fall-off. In the "very large  $s$ " limit, the function,  $f(\theta_{c.m.})$ , which contains the angular dependence of the cross-section, can also be calculated up to an overall normalization constant. This is a direct consequence of the fact that the  $x$ -dependence of each distribution amplitude is known, in this limit, up to a normalization constant. The normalization of the distribution amplitudes can, in principle, be determined from the form factor data for the hadrons involved, and Eq. (2.24) can then be used to make a QCD prediction for the *absolute* normalization of the elastic cross-section.

### 2.3.2. THE PINCH SINGULARITY

We now want to focus our discussion on high momentum transfer elastic scattering processes,  $AB \rightarrow AB$ . As in the case of elastic form factors, the integration over the longitudinal momentum fractions in Eq. (2.22) can lead to singularities in the scattering amplitude. This in turn can generate, through the introduction of a new mass scale, a logarithmic or even a power-law violation of the scaling laws derived above. The first such possibility that needs to be examined is that of end-point singularities, which were discussed in Sec. 2.2.5 for the case of form factors. These make their appearance in elastic scattering when one of the quarks in either or both hadrons carries almost all the longitudinal momentum of that hadron, causing some of the internal propagators to go on shell. In the region where both hadrons contain such a quark one must also consider the diagram where the scattering takes place through the exchange of these two quarks. The analysis of these singularities in Sec 2.2.5 can be carried over, with almost no change, to the present case and the contribution of the end-point region to the elastic scattering amplitude can be shown to be suppressed by powers of  $\alpha_s(\Lambda Q)$  and also by a Sudakov factor generated in this region.

Far more significant is Landshoff's *pinch* singularity, which is a new feature, not found in form factors. It turns out that in the case of elastic scattering the hard scattering amplitude can become infinitely large, not only in the end-region of the integration space, but also in regions in the middle of this space. Let us, for the moment, assume that we are working in covariant perturbation theory. Then each of these singular regions is defined by a given relationship between the longitudinal momentum fractions of the various quarks which, when obeyed, causes one of the internal propagators in a particular Born diagram to go on shell, resulting in the vanishing of the denominator of  $T_H$ . Assuming that

the propagators have a small imaginary part,  $i\varepsilon$ , these singularities in  $T_H$  can be viewed as poles in the complex plane associated with *one* of the integration variables; and they merely lead to an imaginary (absorptive) part in the integrated amplitude, corresponding to the presence of real intermediate states. However, as the *other* variables change their values these poles move along trajectories in this complex plane and two or more of them may coincide with each other for some particular values of these other variables. If this coincidence occurs between poles on the same side of the integration contour then it is harmless and still leads to a finite integral. It turns out that, for some Born diagrams in  $T_H$ , two poles on opposite sides of the integration contour coincide with each other and as  $\varepsilon$  is taken to zero this coincidence leads to a "pinch singularity" in the integrated amplitude, so named since it is a result of the integration contour being pinched between the two poles.

In order to be able to calculate the contribution of these singular diagrams we must regulate the singularity. This can be done by re-introducing the quark transverse momentum into the propagators, which in Eq. (2.5a) had been set to zero as an approximation. We now replace the transverse momentum squared by its average value,  $\Lambda^2$ . (The singularity can also be regulated by introducing a quark mass in the quark propagators). After the regulated integral is carried out one finds that the pinch singularity manifests itself as a power of  $s/\Lambda^2$  in the integrated amplitude. Thus the effect of the mass scale  $\Lambda$  persists even at high energies and the dimensional scaling law for the scattering process no longer holds for the contribution of the "pinch diagrams" to the cross-section.

As a simple example consider the case of  $\pi\pi$  elastic scattering. Fig. 2.6a represents an example of a hard-subprocess Born diagram which has a pinch singularity in its contribution to the amplitude. The two quark propagators,  $q_1, q_2$ , and the gluon propagator,  $g_1$ , are the ones that go on shell in the middle of

the integration space. The denominators of these propagators, in covariant perturbation theory, can be shown to have the following representation:

$$q_1: \quad -x_c(x_b - x_d)s - x_b(x_c - x_d)t + i\varepsilon$$

$$q_2: \quad (1 - x_c)(x_b - x_d)s + (1 - x_b)(x_c - x_d)t + i\varepsilon$$

$$g_1: \quad (x_a - x_c)(x_b - x_d)s + (x_a - x_b)(x_c - x_d)t + i\varepsilon$$

The three poles, corresponding to each of these propagators going on shell, coincide in the region defined by  $x_b = x_c = x_d$ , and give rise to a pinch singularity in the integrated amplitude corresponding to this diagram. After regulation, the contribution to the amplitude from the singular region of this diagram can be shown to contain a factor,  $(s/\Lambda^2)^{1/2}$ , over and above the  $s$ -dependence expected from dimensional counting [3]. For large enough  $s$ , the "pinch contribution" will dominate the amplitude obtained from this diagram, and furthermore, the contribution of the "pinch diagrams" will dominate the total Born amplitude for the process. Thus the power-law of the cross-section will change from the dimensional counting prediction of  $1/s^6$  to a slower fall-off with  $s$  given by  $1/s^5$ . Moreover, to calculate the absolute normalization of the cross-section, we now need to know, with good accuracy, the mass scale that regulates the singularity. This scale must be of the same order of magnitude as the QCD scale parameter,  $\Lambda$ , used in the definition of the running coupling constant, but it does not have to be equal to it.

We shall see in the next section that the above calculation of the pinch contribution is not entirely fair. It does provide the correct  $s$ -dependence but it does not reveal the full uncertainty of the absolute normalization.

### 2.3.3. THE MULTIPLE SCATTERING MODEL

The transverse momentum that flows through the gluon connecting the two constituents of the incident pion in Fig. 2.6a, can be shown to be given by  $(x_c - x_b)\sqrt{t} + (x_d - x_b)\sqrt{u}$ . For large angle scattering  $s$ ,  $t$  and  $u$  are all of the same order. Thus in the region defined by  $(x_c - x_b) \approx (x_d - x_b) \approx \Lambda/\sqrt{s}$ , the gluon does not transfer large transverse momentum from one constituent to another. (Note that this gluon need not be soft; it may transfer longitudinal momentum from one constituent to another if it is collinear with the pion momentum). The contribution of the pinch singularity to the amplitude corresponding to this diagram comes from integration over exactly this region, which is therefore called the "pinch region". Because of the absence of hard gluon interactions amongst the constituents within any of the participating hadrons, the perturbative analysis used in the derivation of Eq. (2.22), is no longer obviously valid in this region. The calculation described in the previous section is therefore based on wrong assumptions and the contribution from the pinch region must be analyzed separately.

Since the gluon  $g_1$  in Fig. 2.6a is not necessary for the hard scattering of the hadrons in the pinch region, we can absorb it in the wave function of the incident pion, as was done for the end-point region of the form factor. The leading order contribution to the hard scattering process in the pinch region can now be given a different interpretation. The hadrons transfer large transverse momentum to each other through the independent scattering of each constituent of one hadron against a different constituent of the other hadron. This is illustrated in Fig 2.6b for the case of meson-meson scattering which consists of two independent scatterings. The baryon-baryon case will similarly involve three such scatterings. Meson-baryon scattering has to be handled separately since the two hadrons contain a different number of constituents. Note that the

scatterings take place between nearly on-shell quarks and, after undergoing independent hard scatterings, the momenta of the quarks are so aligned that they can readily recombine to make up the final state hadrons.

The above picture of elastic hadron scattering is sometimes called the *multiple-scattering model*. It was first proposed by Landshoff as an alternative mechanism for high momentum transfer elastic scattering [4]. The  $1/Q^2$  suppression of the amplitude, caused by the presence of an additional hard gluon in the *hard-scattering model* diagrams for  $\pi\pi$  scattering, is absent in the case of multiple scattering. On the other hand, the multiple scattering contribution is suppressed because the phase space available to the constituents, if they are to recombine after being scattered independently, is limited. In the multiple scattering model, it is the scale which defines the limit on the transverse momentum of the hadronic constituents, (again denoted by  $\Lambda$ ), that causes the scale breaking of the cross-section to occur.

As a first step towards calculating the pinch contribution (which is now identified with the multiple scattering contribution) let us express the elastic scattering amplitude for  $\pi\pi$  scattering as a convolution of the multiple scattering amplitude with the wave functions for the initial and final hadronic states. Then, working once again in the infinite momentum frame and using time-ordered perturbation theory, this representation of the amplitude, assumed to hold for the *whole* range of momentum fractions, becomes

$$M_{\pi\pi}(s, \theta_{c.m.}) = \int_0^1 [dx_a] \dots [dx_d] \int_{-\infty}^{\infty} [dk_{1a}] \dots [dk_{1d}] \psi_C^*(x_c, k_{1c}) \psi_D^*(x_d, k_{1d}) \\ \times T_{MS}(x_a \dots x_d, k_{1a} \dots k_{1d}, s, \theta_{c.m.}) \psi_A(x_a, k_{1a}) \psi_B(x_b, k_{1b}), \quad (2.25)$$

where  $T_{MS}$  is the leading order multiple scattering amplitude. The independent conservation of momentum in each of the two scatterings in Fig. 2.6b imposes restrictions on the independence of the longitudinal and transverse momenta of the quarks belonging to different hadron states. The restrictions are:

$$x_a + x_b = x_c + x_d \quad (2.26a)$$

$$|k_{1a} + k_{1b} - k_{1c} - k_{1d}| = (x_c - x_b)\sqrt{t} + (x_d - x_b)\sqrt{u} \quad (2.26b)$$

For most values of  $x_a, \dots, x_d$ , at least one of  $k_{1a}^2, \dots, k_{1d}^2$  is of order  $s = |t| + |u|$ , and a hard scattering amplitude can be built up by extracting the hard gluons from the wave functions. However, we are interested in the contribution from the pinch region (or the multiple scattering region) which is now defined by the equations,  $x_a \approx x_b \approx x_c \approx x_d$ , all equalities being true to within  $\Lambda/\sqrt{s}$ . In this region  $|k_{1a} + k_{1b} - k_{1c} - k_{1d}| \approx \Lambda$  and all quark transverse momenta can be small. The large transverse momentum region of each wave function will be damped by the large transverse momentum that must necessarily flow through at least one of the other wave function. The transverse momentum integrals in Eq. (2.25) are then convergent for all  $|k_{1i}| \lesssim \Lambda$  and it is no longer possible to factor out distribution amplitudes and to use them to absorb collinear divergences in the higher order corrections to  $T_{MS}$ . It is, however, possible to show that the  $s$ -dependence of the pinch contribution obtained from integrating the unfactored, leading order amplitude in Eq. (2.25) is the same as the one obtained from the integral in Eq. (2.22).

Because of their rapid convergence in the pinch region, the transverse momentum integrals in Eq. (2.25) can be approximated by replacing each of the  $k_{1a}, \dots, k_{1d}$  in the wave functions, and in  $T_{MS}$ , by  $\Lambda$ . After a simple analysis of the energy-denominators, the pinch singularity in  $T_{MS}$  can be factored out in the

form of a  $\delta$ -function. The multiple scattering contribution then becomes

$$\begin{aligned}
 M_{\pi\pi}(s, \theta_{c.m.}) &\propto \int_0^1 dx_a \int_{-\Lambda/\sqrt{t}}^{\Lambda/\sqrt{t}} d(x_c - x_b) \int_{-\Lambda/\sqrt{u}}^{\Lambda/\sqrt{u}} d(x_d - x_b) \psi_C^*(x_c, \Lambda) \psi_D^*(x_d, \Lambda) \\
 &\quad \times M_{qq}^2 \frac{4\pi}{i} \delta[(x_c - x_b)t + (x_d - x_b)u] \psi_A(x_a, \Lambda) \psi_B(x_b, \Lambda) \\
 &\approx -\frac{8\pi i \Lambda}{(stu)^{\frac{1}{2}}} \int_0^1 dx_a \psi_C^*(x_a, \Lambda) \psi_D^*(x_a, \Lambda) \psi_A(x_a, \Lambda) \psi_B(x_a, \Lambda) \\
 &\quad \times M_{qq}^2(x_a, s, \theta_{c.m.}) , \tag{2.27}
 \end{aligned}$$

where  $M_{qq}$  is the quark-quark elastic scattering amplitude. This amplitude can be easily computed and it turns out to be independent of  $x_a$ ,

$$M_{qq} = 8\pi\alpha_s \times \begin{cases} s/t & \text{for equal quark helicities ,} \\ u/t & \text{for opposite helicities ,} \end{cases}$$

In lowest order, the contribution to the  $\pi\pi$  cross-section from the pinch region can now be written as

$$\begin{aligned}
 \frac{d\sigma}{dt}^{MS}_{\pi\pi \rightarrow \pi\pi}(s, \theta_{c.m.}) &\propto \alpha_s^4 \frac{(s^2 + u^2)^2}{s^3 t^5 u} \\
 &= \frac{\alpha_s^4}{s^5} f(\theta_{c.m.}) , \tag{2.28}
 \end{aligned}$$

We now see that the fixed-angle  $s$ -dependence of this contribution agrees with the  $s$ -dependence of the pinch contribution calculation described in the previous section. The above calculation completely determines the energy dependence and the angular dependence of the multiple scattering cross-



section but the absolute normalization depends, not only on the little known constant  $\Lambda$ , but also on the non-perturbative, and therefore completely unknown, part of the pion wave function. *If the elastic cross-section is dominated by the pinch contribution, then any hopes of determining its absolute normalization, using only perturbative QCD, are lost.* Furthermore, the higher order corrections to this lowest order result are no longer obviously small because the scattering amplitude in the pinch region does not yield to a renormalization group approach.

#### 2.3.4. THE SUDAKOV FACTOR

The above analysis of the multiple scattering mechanism ignores the presence of infrared divergences in higher order corrections to the amplitude. These divergences tend to spoil the convergence of the perturbation series. It is important to examine these corrections to see if they lead to a modification of the  $s$ -dependence of the leading order result stated in Eq. (2.28). The higher order corrections to  $T_{MS}$  can be divided into two distinct classes: (a) those where the extra propagators added to the Born diagram just modify the individual quark-quark scatterings, and (b) those where they connect different scatterings. Fig. 2.7 shows examples of both classes of diagrams for the case of a single-gluon insertion into the  $\pi\pi$  multiple scattering diagram of Fig. 2.6b. Within the class-(a) diagrams, important contributions come from radiative corrections to the quark-gluon vertices and from the exchange of additional gluons between the two quarks. The loop integrals in these diagrams have divergences, which come from the region where the inserted gluons become soft or collinear. If the coupling constant is assumed to be independent of the gluon momentum then each loop integral contributes a double logarithm. The double-log term in the first order correction to  $T_{MS}$ , from the diagrams in class-(a), can be shown to be

given by  $(4C_F\alpha_s/\pi)\ln^2(s/\Delta^2)$  times  $T_{MS}$ , where  $\Delta^2$  is the off-shellness of the quarks involved in the scatterings. In the pinch region we can take  $\Delta^2$  to be equal to  $\Lambda^2$ . The error caused by assuming the coupling constant to be fixed only affects the non-leading logs. It is well known that the leading double-logs in each order of fermion-fermion scattering can be summed into an exponential factor (*Sudakov factor*) that multiplies the leading order amplitude.

The diagrams in class-(b) do not have loops but they do contain extra degrees of freedom to be integrated over, since the restrictions imposed by the independent conservation of momenta in each scattering are now absent. These degrees of freedom can be translated into the longitudinal and transverse momentum of the connecting gluon. Since we are interested in the corrections to the pinch contribution of the scattering amplitude the momentum of this gluon should be routed through the wave functions in such a way that the pinch singularity of the remaining amplitude is preserved during the integration over this momentum. This is equivalent to ensuring that the amplitude still involves nearly on-shell quarks, so that we keep away from the hard scattering regime. (Notice that class-(b) diagrams are also the diagrams involved in the leading order hard scattering mechanism.) The soft-collinear region of this integration then yields double logarithms with the same argument as the ones from the loop integrals of class-(a) diagrams. The color singlet nature of the pion implies that these double-logs should *exactly cancel* the previous ones. However, the integration over the component of the gluon momentum which is perpendicular to the plane of scattering is suppressed by the  $1/k_\perp^2$  factor from the pion wave function, thus reducing the double-log contribution from the class-(b) diagrams to half their expected value. This prevents a complete cancellation and the remaining double-log terms still exponentiate to give a Sudakov factor. In the leading log approximation, the Sudakov factor for  $\pi\pi$  scattering can be shown to

be

$$S_{\pi\pi}(s) = \exp\left(-\frac{2C_F\alpha_s}{\pi} \ln^2 \frac{s}{\Lambda^2}\right). \quad (2.29)$$

This factor severely damps the contribution of the scattering amplitude coming from the pinch region. Even for moderate values of  $s$  the Sudakov factor works out to be much smaller than  $\Lambda/\sqrt{s}$ , and for a fixed coupling constant, the factor falls with  $s$  faster than any fixed power of  $s$ . Thus, despite the slower fall-off with  $s$  of the multiple scattering mechanism, its contribution seems to be negligible because of the suppression from the Sudakov factor. It seems then, that the hard scattering mechanism may still provide the dominant contribution to elastic hadron scattering. The application of the renormalization group to elastic scattering would then be justified, and a calculation of the first order, hard scattering contribution, for large enough  $s$ , should yield a reliable cross-section.

*This conclusion, despite popular belief, is wrong! The ability to sum leading double-logs to generate a Sudakov factor is not confined to the pinch region of the integration space.* Double-log factors of  $\ln^2(s/\Delta^2)$  are generated whenever the off-shellness of the quarks, undergoing high momentum transfer scattering, is held fixed at some  $\Delta^2$ . Thus the factor derived in Eq. (2.29), when generalized by replacing  $\Lambda^2$  by  $\Delta^2$ , holds for all regions of the integration space. As one moves from the hard scattering region,  $\Delta^2=O(s)$ , to the pinch region,  $\Delta^2=O(\Lambda^2)$ , the effect of the Sudakov factor changes from no suppression to maximum suppression. In calculating the contribution from a connected pinch diagram, such as the one in Fig. 2.6a, we must now include the Sudakov factor in the integration over the momentum fractions of the quarks. The pinch region is then automatically suppressed and the factorized representation of the scattering amplitude, as displayed in Eq. (2.22), is valid for the whole range of

integration.

Before we discuss further the pinch diagram calculation, let us go back and improve the Sudakov factor by allowing the coupling constant to run with the gluon momentum, as is the case in QCD. Mueller [3] has studied this in detail and he has shown that the leading divergence in the class-(a) diagram loop-integrals can be reduced to the following integral over gluon transverse momentum:

$$\int_{\Delta^2}^s \frac{dk_{\perp}^2}{k_{\perp}^2} \frac{\alpha_s(k_{\perp}^2)}{2\pi} \ln \frac{s}{k_{\perp}^2} = \frac{2}{\beta_0} \left[ \ln \frac{s}{\Lambda^2} \left( \ln \ln \frac{s}{\Lambda^2} - \ln \ln \frac{\Delta^2}{\Lambda^2} \right) - \ln \frac{s}{\Delta^2} \right] \quad (2.30)$$

where  $\beta_0 = 11 - (2/3)n_f$ ,  $n_f$  being the number of quark flavors. This contribution can be summed into an exponential, in a manner similar to the double-logs, and yields a more accurate Sudakov factor. In order to use this factor to carry out the integration for an amplitude corresponding to a given pinch diagram we need to express  $\Delta^2$  in terms of the integration variables. Taking the diagram of Fig. 2.6a as an example, we see that only two of the eight quark legs go off shell as we move away from the pinch region. Mueller has shown that the end result of adding all the leading log contributions from this diagram is the same as that derived in Eq. (2.30) for a simple loop integral, except that  $\Delta^2$  is now replaced by the minimum of the absolute value of the off-shellness of the three propagators that go on shell in the pinch region. The off-shellness of each of these three propagators can be expressed as a function of the momentum fractions, as shown in Sec. 2.3.2. Then, expressing the minimum off-shellness as a fraction of  $s$ , i.e.  $\Delta_{\min}^2 = Xs$ , so that  $X = X(x_a \dots x_d, \theta_{c.m.})$ , the  $\pi\pi$  Sudakov factor becomes

$$S_{\pi\pi}(s, x_a \dots x_d, \theta_{c.m.}) = \exp \left\{ -\frac{8C_F}{\beta_0} \left[ \ln \frac{s}{\Lambda^2} \left( \ln \ln \frac{s}{\Lambda^2} - \ln \ln \frac{Xs}{\Lambda^2} \right) - \ln \frac{1}{X} \right] \right\} \quad (2.31)$$

We can now replace  $T_H$  by the product  $S_{\pi\pi}T_H$  in the integrand of Eq. (2.22) and carry out the integral over the momentum fractions. The pinch region is again severely suppressed. In this region  $Xs=O(\Lambda^2)$  and the Sudakov factor reduces to the following,

$$S_{\pi\pi}(s) = \text{const.} \exp \left\{ -\frac{8C_F}{\beta_0} \ln \frac{s}{\Lambda^2} \ln \ln \frac{s}{\Lambda^2} \right\} \quad (2.32)$$

The constant multiplying this Sudakov factor is unpredictable because it arises from the non-perturbative, low  $k_1^2$  part of the integration range. However, the contribution from the pinch region again falls with  $s$  faster than any fixed power of  $s$  and becomes negligible compared to the rest of the contribution. Even though the integrated amplitude is now free of the pinch singularity, and no regulation of the integrand is necessary, it is not clear that the amplitude will obey the dimensional scaling law, because the Sudakov factor in Eq. (2.31) contains a mass scale of its own! The factorization of the  $s$ -dependence from the angular dependence, observed in Eq. (2.24), is also no longer obvious because the Sudakov factor itself depends on  $\theta_{c.m.}$ . In general, one can express the Sudakov-modified multiple scattering amplitude for the  $\pi\pi$  case as follows:

$$M_{\pi\pi}(s, \theta_{c.m.}) \sim \frac{1}{s^2} g(s/\Lambda^2, \theta_{c.m.}) \quad (2.33)$$

where we have ignored the logarithmic factors present in the amplitude, and the function  $g$  is the result of carrying out the integral over momentum fractions.

Mueller [3] has made an analytical approximation to the Sudakov-modified integral for the amplitude corresponding to the diagram in Fig. 2.6a. His result contradicts the naive expectations of previous authors, who assumed that after Sudakov suppression the  $s$ -dependence of the integrated amplitude should

correspond to the dimensional scaling laws. It turns out that, in Mueller's approximation, the scattering amplitude still falls as a power of  $s$  but the power is intermediate between the one predicted for hard scattering and the one for multiple scattering. Technically, this happens because the region that dominates the integral is given by  $\Lambda^2 \ll \Delta^2 \ll s$ , which is intermediate between the hard scattering and pinch regions. The renormalization group is applicable in this region but the mass scale in the Sudakov factor causes a deviation from the scaling prediction. Mueller's result, derived in the limit  $s \rightarrow \infty$ , can be expressed as follows:

$$M_{\pi\pi} \propto \frac{1}{s^2} \left[ \frac{s}{\Lambda^2} \right]^{(1/2) - c \ln((2c+1)/2c)} \quad (2.34)$$

where  $c = (8C_F/\beta_0) = 32/25$  for SU(3) with 4 flavors. The power of  $s/\Lambda^2$  for this value of  $c$  works out to be about 0.08, independent of  $\theta_{c.m.}$ . Thus the deviation from the hard scattering prediction seems to be quite small. However, the assumptions made by Mueller in order to get the above result are not at all obvious and one needs an accurate numerical integration to find the true effect of the Sudakov factor on the  $s$ -dependence of the cross-section. In fact our result (discussed later), obtained by a numerical treatment of the same integral, show Mueller's result to be quantitatively incorrect but in reasonable qualitative agreement. Meanwhile, there is still an uncertainty in the absolute normalization because of the lack of knowledge of the exact mass scale that goes into the Sudakov factor.

Not all the diagrams that contribute to  $T_H$  have a pinch singularity in them. For some Born diagrams the poles associated with propagators going on shell do not pinch the integration contour and the integrated amplitude has no singularity. A Sudakov factor cannot be extracted for the amplitude corresponding to

these diagrams and their contribution obeys the dimensional scaling law. Thus the elastic scattering amplitude consists of two separate components; the hard scattering component, which falls with  $s$  according to dimensional scaling and the multiple scattering component which, even after Sudakov suppression, probably has a softer dependence on  $s$ . For  $\pi\pi$  scattering there are about as many diagrams with a pinch singularity in them as there are without it. For  $\pi p$  and  $pp$  scattering the two numbers are again estimated to be comparable. Whether one contribution dominates over the other or not, at a given energy and angle, depends on the as yet uncalculated functions  $f(\theta_{c.m.})$  and  $g(s/\Lambda^2, \theta_{c.m.})$ , and on the magnitude of  $\Lambda$ . Our analysis up to now allows us to represent the elastic scattering cross-section as follows:

$$\frac{d\sigma}{dt} \sim \frac{1}{s^n} \left[ f(\theta_{c.m.}) + g(s/\Lambda^2, \theta_{c.m.}) \right]^2 \quad (2.35)$$

( $n=6$  for  $\pi\pi$ ,  $n=8$  for  $\pi p$  and  $n=10$  for  $pp$ ).

If, as we are led to believe from Mueller's analysis,  $g(s/\Lambda^2, \theta_{c.m.})$  is an increasing function of  $s$  at fixed angle, then the non-scaling multiple scattering component will dominate the cross-section at large enough energy. Thus the suppression of Landshoff diagrams, which has become a widely believed proposition, is *not at all obvious* in this more careful analysis. This crucial question can only be answered by a detailed calculation of the functions  $f$  and  $g$ .

### 2.3.5. ANGULAR DEPENDENCE

The calculation of the angular dependence of the elastic scattering cross-section, in the "QCD model" discussed above, is a very complicated task. It involves the detailed computation of a very large number of Feynman diagrams followed by a multi-dimensional integral over the momentum fractions of the

participating hadrons. The only case in the past literature where such an attempt has been made is a calculation by Farrar and Wu [5], wherein they calculate the angular dependence of a very limited set of Feynman diagrams for pp elastic scattering. Their calculation is restricted to the multiple-scattering pp diagrams, and that too without a Sudakov factor (the naive Landshoff contribution). Therefore, their result does not shed much light on the predictions of the above section.

All other attempts in this direction have been made in the context of a once moderately popular but now quite untenable model, the so called *constituent interchange model* (CIM) [6]. This model does have its foundation in QCD but it includes within it some extra assumptions that have no theoretical basis but were added on, in order to provide a quick and simple explanation of some high- $P_T$  exclusive and inclusive data. The basic assumption of this model is that the interchange of quarks between two hadrons provides the dominant mechanism for their interaction in scattering reactions. This further implies that the hard subprocess in a high- $P_T$  scattering amplitude consists, not of quark-quark interactions but of quark-hadron interactions. Consequently, one has to introduce dimensional coupling constants and the scaling property of QCD amplitudes is destroyed. *For the case of elastic hadron scattering this model implies that the diagrams with any gluon exchange between quarks of different hadrons are suppressed.* Thus the only diagrams that survive are the ones involving interchange of two or more quarks with all gluon interaction restricted to within the quarks of an incoming or outgoing hadron. Making some further simplifying assumptions about the structure of hadron wave functions, one can calculate the angular dependence of this special set of diagrams without having to do any complicated trace calculations. The CIM prediction for pp elastic scattering, for  $\theta_{c.m.}$  not too small, is given by (see Ref. [6]):



$$\frac{d\sigma}{dt}_{pp} \sim \frac{1}{s^{12}} \frac{J(\sin\theta_{c.m.})}{\sin^{12}\theta_{c.m.}} \quad (2.36)$$

where  $J$  is a slowly varying function. The agreement with data of this angular dependence is satisfactory but not convincingly good. Moreover, the calculation is quite sensitive to the assumed spin structure of the proton wave function.

Almost all the successes of the CIM model have now been explained by a more careful analysis of the quark-quark subprocess, and in some cases detailed QCD calculations of the CIM diagrams have shown that the assumptions of the model are not true in perturbative QCD. The only reason that we mention this over-simplified model in this review is because the data on pp elastic scattering seem to favor the strong dominance of quark exchange diagrams over diagrams involving only gluon exchange between hadrons. It is important to see if we can find any clue to this unexpected behavior in our QCD model developed in the above sections. The number of quark exchange diagrams for pp scattering is somewhat larger than the number of gluon exchange diagrams but certainly not enough to explain the experimental data. The way to settle the question of whether or not the CIM assumptions hold true in perturbative QCD again lies in a detailed computation of the Feynman diagrams, a task that has been avoided by theorists because of the large number and the extreme complexity of these diagrams.

Even though, finding the angular dependence of an elastic scattering diagram needs a detailed calculation, one can quite easily deduce the asymptotic form of the amplitude as the scattering angle tends to zero. If the amplitude corresponding to a given diagram is represented by  $A(s,t)$ , then this analysis is equivalent to finding the limiting form of  $A$  as  $t/s$  goes to zero. The study of Feynman diagrams in this limit has its origin in Regge theory which is

useful for analyzing amplitudes at small, fixed  $t$  as  $s \rightarrow \infty$ . In this so called Regge limit, the amplitude can be shown to take the form  $A(s, t) \sim \beta(t) s^{\alpha(t)}$ . For large  $t$  the coupling constant is small, the Born term dominates the scattering amplitude and  $\alpha$  tends to an integer or a half-integer equal to the spin of the exchanged particle. Now in QCD the Born terms for hadron scattering are always box diagrams and never single particle exchange, because of color conservation. (The Born terms can also involve more than two exchanged particles). We then need to derive an asymptotic form for the box diagram given the form for the single particle exchange. One can use the unitarity equation to show, that for the box diagram amplitude,

$$A(s, t) \sim s^{\alpha_1(t_1) + \alpha_2(t_2) - 1} \quad (2.37)$$

where  $t_1, t_2$  are integrated over the allowed kinematic region and  $\alpha_1$  and  $\alpha_2$  are the spins of the two exchanged particles.

We can now apply Eq. (2.37) to the  $\pi\pi$  scattering box diagrams (Fig. 2.8). We immediately see that the behavior of quark-exchange and gluon-exchange diagrams is completely different and serves as a way to tell them apart while analyzing angular dependence data. For quark-exchange each  $\alpha_i = 1/2$  and so the resultant box has  $\alpha = 1/2 + 1/2 - 1 = 0$ . For gluon-exchange each  $\alpha_i = 1$  and the power of  $s$  in the amplitude is given by  $\alpha = 1 + 1 - 1 = 1$ . One can now treat the new power,  $\alpha$ , as an effective spin of the combination of the two exchange particles and use the formula in Eq. (2.37) once again to find the power of  $s$  when a third exchange particle is added to the diagram. We then see that adding additional exchange gluons to the two diagrams in Fig. (2.3) does not change the values of  $\alpha$  calculated above. If the scattering amplitude goes like  $s^\alpha$  then the cross-section will go like  $s^{2\alpha-2}$ . The results obtained above, for fixed  $t$ ,  $s \rightarrow \infty$ , can then be summarized as follows:

$$\text{quark-exchange:} \quad A \sim \text{const.} \quad \frac{d\sigma}{dt} \sim \frac{1}{s^2} \quad (2.38a)$$

$$\text{gluon-exchange:} \quad A \sim s \quad \frac{d\sigma}{dt} \sim \text{const.} \quad (2.38b)$$

If we further assume that dimensional scaling is valid for the scattering diagrams considered above, then the  $t$ -dependence of the amplitude can be immediately deduced from the  $s$ -dependence. Thus for  $\pi\pi$  scattering the quark-exchange amplitude goes like  $1/t^2$  while the one for gluon-exchange goes like  $s/t^3$ . We can then express the  $\pi\pi$  elastic scattering cross-section at small angles (i.e. small  $t/s$ ) in terms of two calculable constants:

$$\frac{d\sigma}{dt}_{\pi\pi} \sim \frac{1}{s^2} \left[ c_g \frac{s}{t^3} + c_q \frac{1}{t^2} \right]^2 \quad (2.39)$$

If there is any truth at all in the CIM assumptions for elastic hadron scattering then we would expect  $c_q/c_g \gg 1$ . This ratio is independent of the coupling constant and the distribution amplitudes and can be accurately computed in our QCD model.

**FIGURE CAPTIONS**

- Fig. 2.1      Factorization of the underlying hard subprocess ( $ab \rightarrow cd$ ) from the soft subprocess functions in the inclusive reaction  $AB \rightarrow CX$ .
- Fig. 2.2      (a) The factorized representation of the proton's magnetic form factor. (b) Some lowest order diagrams that contribute to  $T$ .
- Fig. 2.3      (a) Diagrammatic representation of the Bethe Salpeter bound state equation for a pion. (b) Some terms in the perturbative expansion of the kernel.
- Fig. 2.4      (a) Representation of the proton form factor in the end-point region. (b) A radiative correction to the photon-quark vertex. (c) A higher order correction involving the spectator quark.
- Fig. 2.5      (a) The factorized representation of the exclusive process  $AB \rightarrow CD$ . (b) Some leading order contributions to the hard scattering amplitude for meson-baryon elastic scattering.
- Fig. 2.6      (a) A connected hard-subprocess diagram for  $\pi\pi$  scattering which contains a pinch singularity. (b) A multiple scattering diagram resulting from the absorption of the soft gluon into the wave function of pion A.

Fig. 2.7 Higher order corrections to the multiple scattering amplitude: (a) some diagrams where the extra gluon only modifies an individual quark-quark scattering; (b) some diagrams where the gluon connects the two individual scatterings.

Fig. 2.8 Box diagrams for  $\pi\pi$  elastic scattering: (a) quark exchange (b) gluon exchange.

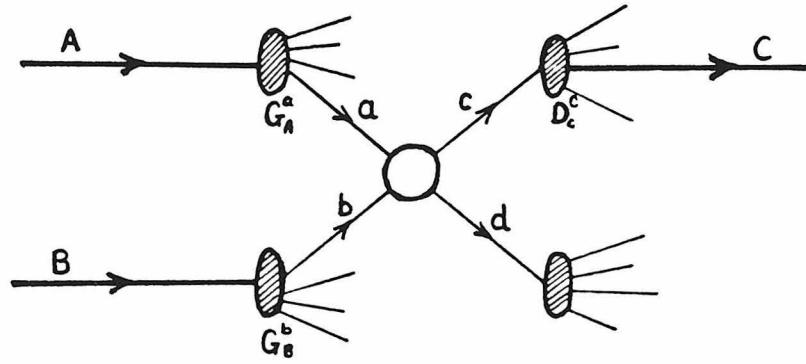
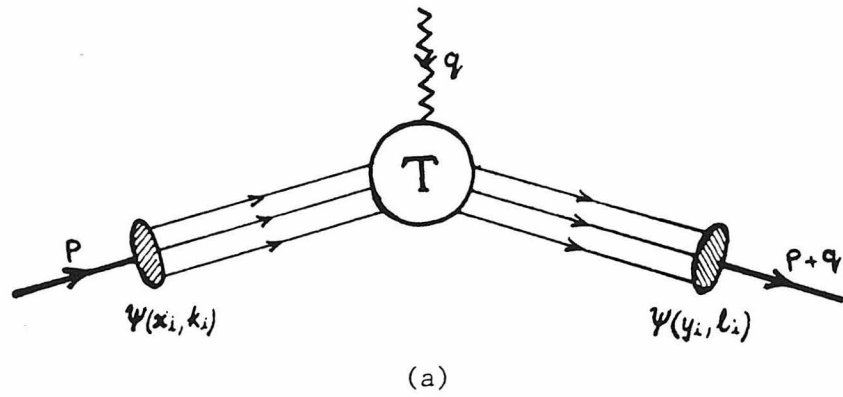


Fig. 2.1



$$T = \begin{array}{c} \begin{array}{ccc} x_1 \rightarrow & \begin{array}{c} \text{wavy } q \\ \downarrow \end{array} & \rightarrow y_1 \\ x_2 \rightarrow & \begin{array}{c} \text{wavy } q \\ \downarrow \end{array} & \rightarrow y_2 \\ x_3 \rightarrow & \begin{array}{c} \text{wavy } q \\ \downarrow \end{array} & \rightarrow y_3 \end{array} + \begin{array}{ccc} x_1 \rightarrow & \begin{array}{c} \text{wavy } q \\ \downarrow \end{array} & \rightarrow y_1 \\ x_2 \rightarrow & \begin{array}{c} \text{wavy } q \\ \downarrow \end{array} & \rightarrow y_2 \\ x_3 \rightarrow & \begin{array}{c} \text{wavy } q \\ \downarrow \end{array} & \rightarrow y_3 \end{array} + \dots \end{array}$$

(b)

Fig. 2.2

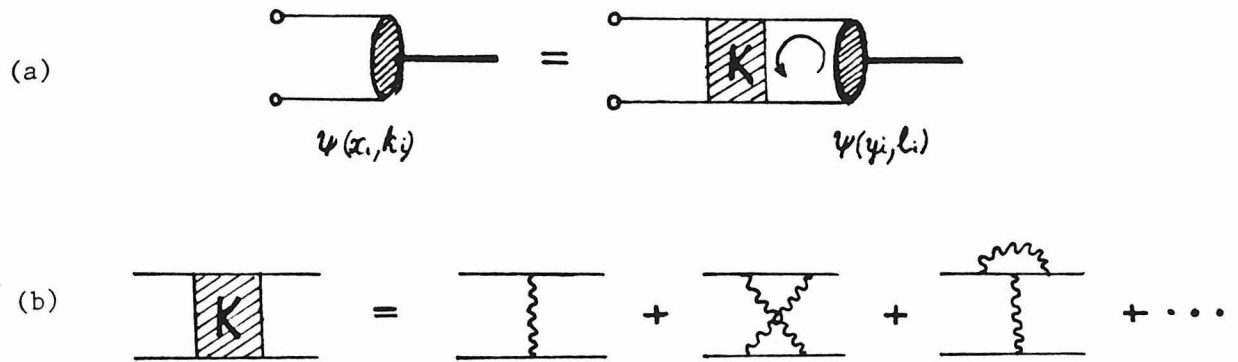


Fig. 2.3

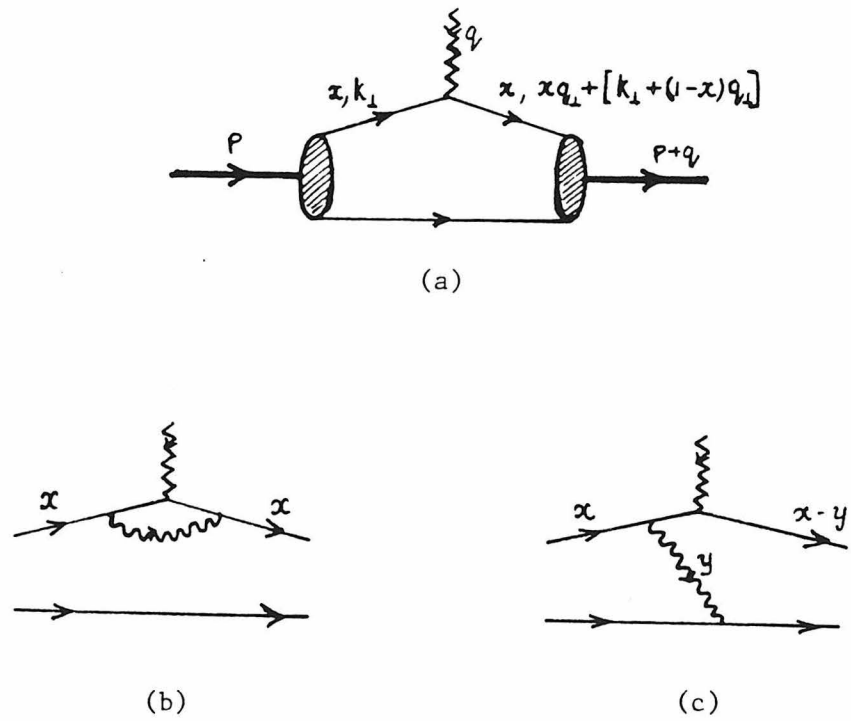


Fig. 2.4

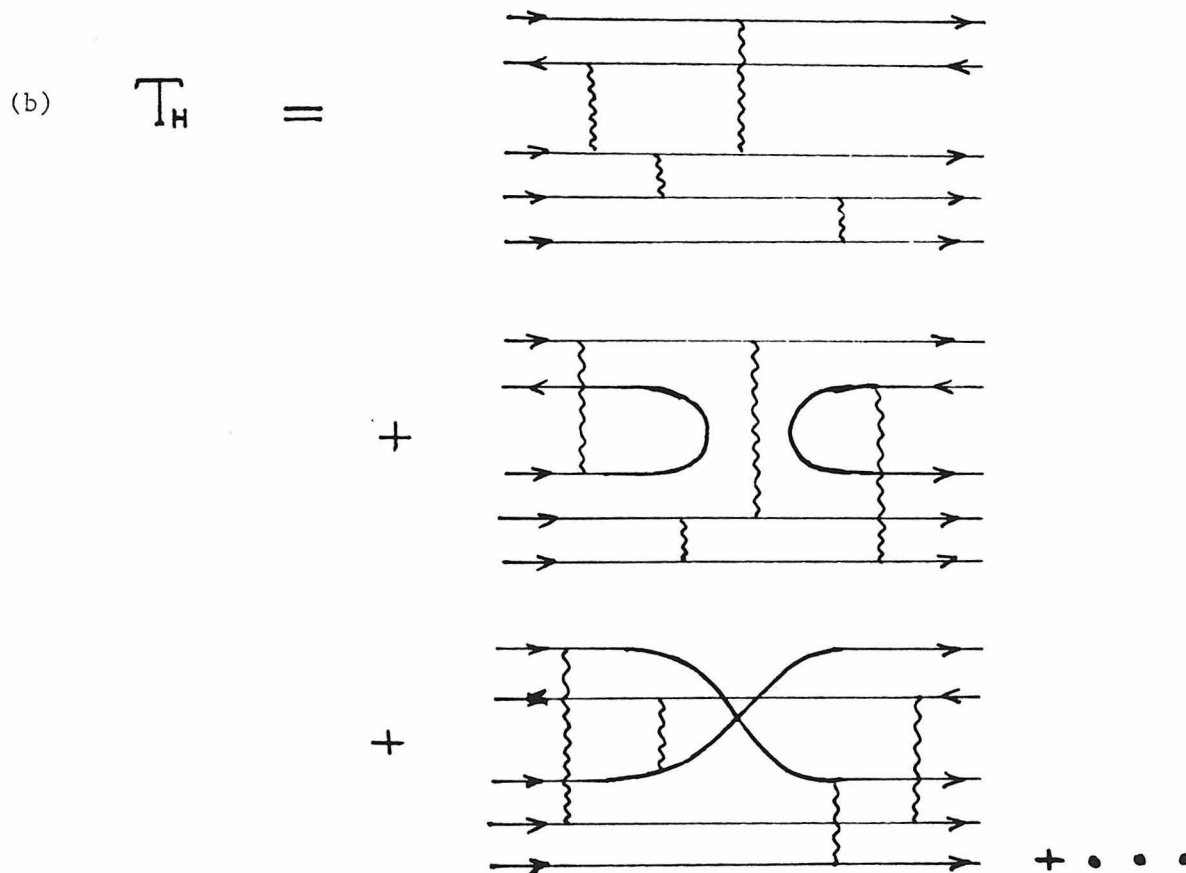
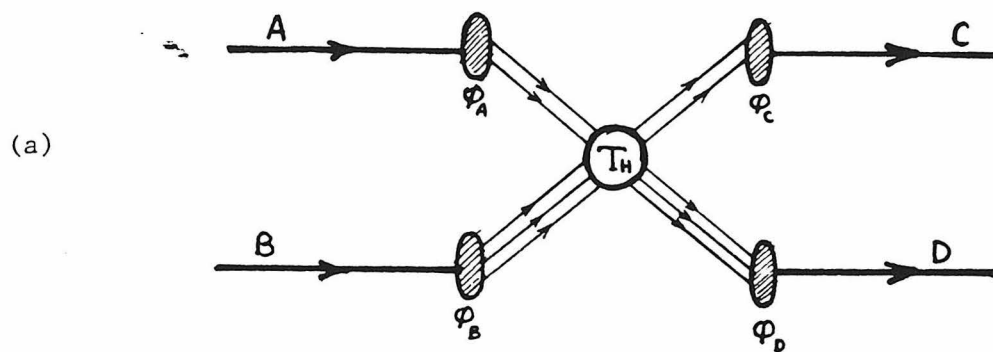


Fig. 2.5



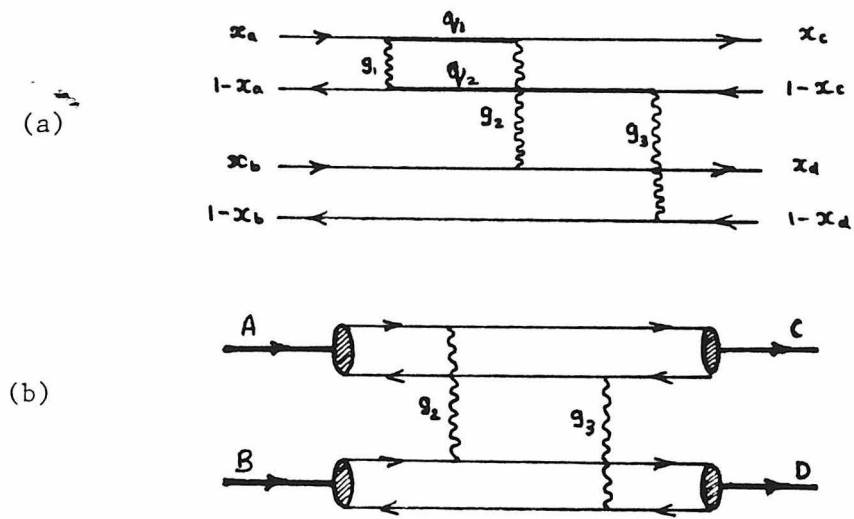


Fig. 2.6

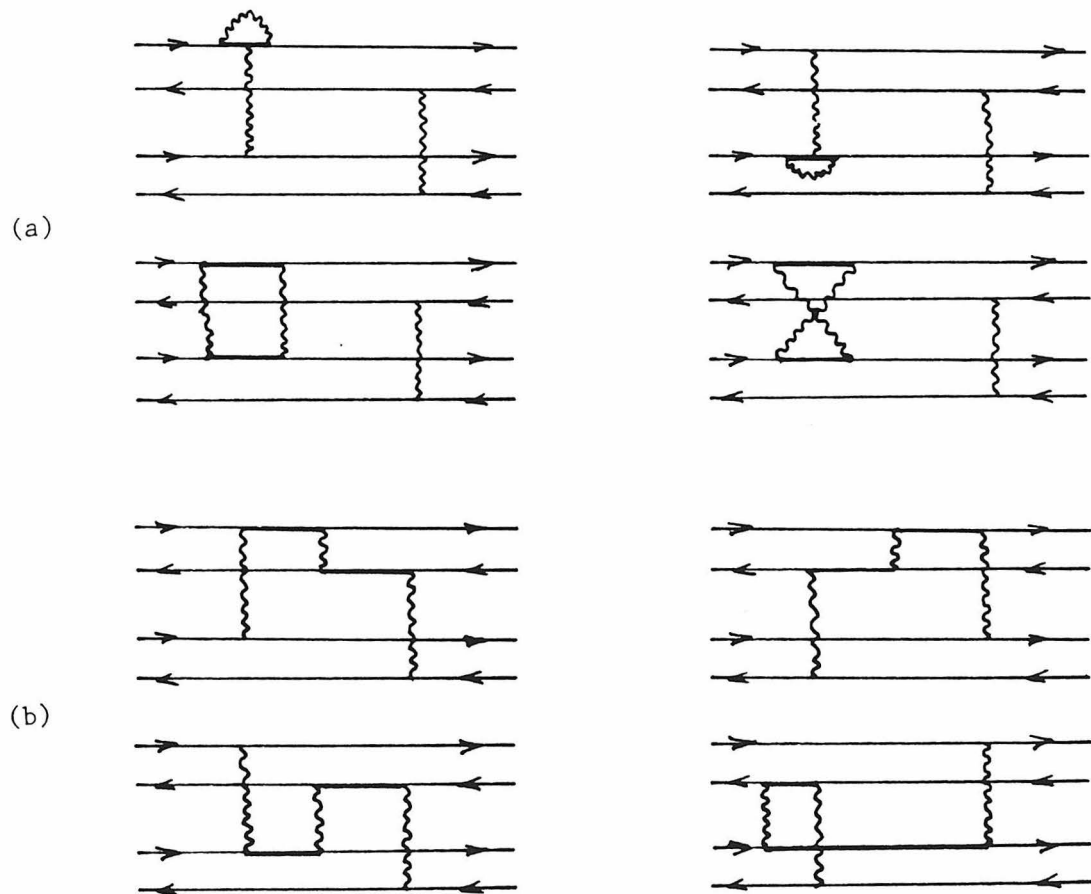


Fig. 2.7

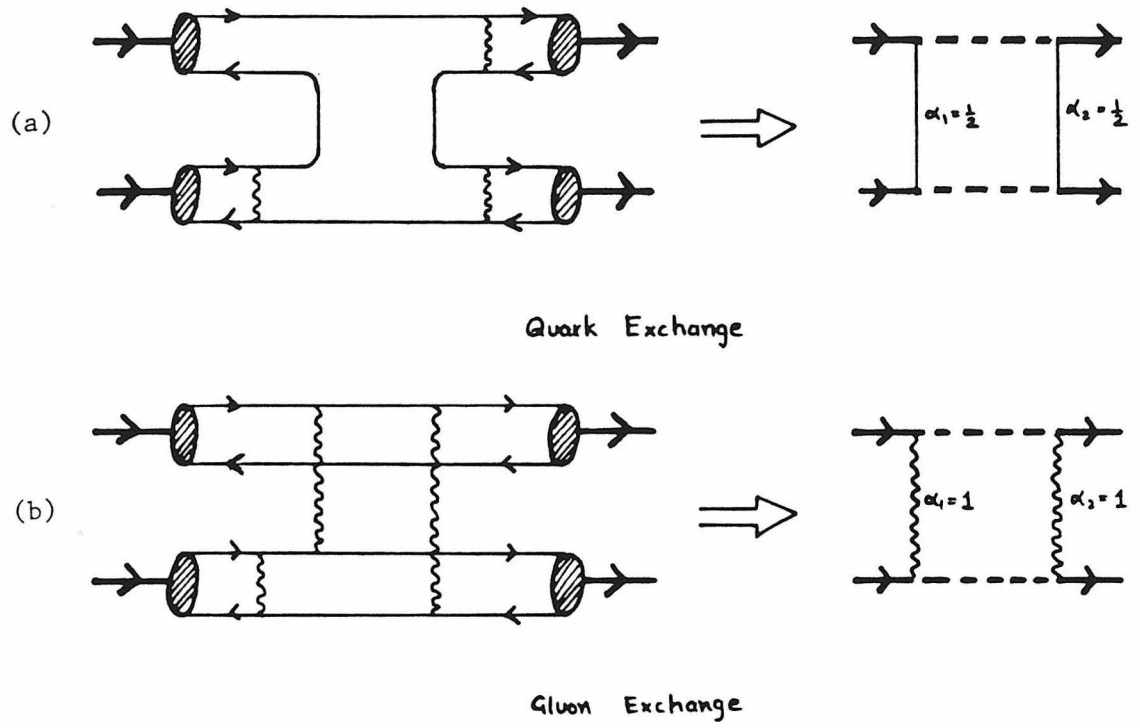


Fig. 2.8

## CHAPTER III

### HIGH $P_T$ ELASTIC HADRON SCATTERING: REVIEW OF EXPERIMENT

Differential cross-sections for high- $P_T$  elastic hadron scattering have been measured for several pairs of hadrons and for various ranges of center-of-mass energy and center-of-mass angle. Data in this area of hadronic phenomenon have been accumulating for a span of almost two decades now. For this review it is useful to divide the available data into two broad classes: (a) - *intermediate energy data* spanning the whole range of c.m. angles and useful for our purposes in the domain of relatively large angles; these data come from experiments at Argonne, Brookhaven and the CERN-PS. (b) - *high energy data* measured at small c.m. angles in experiments at Fermilab and the CERN-ISR. We shall examine the two classes of data one by one since they shed light on different aspects of the theory.

#### 3.1. INTERMEDIATE ENERGY, WIDE ANGLE DATA

Scaling of the structure functions in deep inelastic scattering seems to hold for values of  $Q^2$  as low as a couple of  $\text{Gev}^2$ . We should therefore expect that elastic scattering data for  $|t|$ -values above a few  $\text{Gev}^2$  will prove to be useful for comparison with the QCD model developed in the previous chapter. Large  $|t|$  (which in this case implies wide-angle) data, is available for several different elastic scattering reactions, enabling us to put the theory to a fairly stringent test. Some of the reactions for which wide-angle data have been used for such

tests are listed below, along with the *maximum* energy up to which wide-angle measurements exist in each case. The values of  $n$  shown are the predictions for the power-law fall-off with  $s$  assuming dimensional scaling to hold true in this energy range.

$pp \rightarrow pp$	$s \lesssim 60 \text{ GeV}^2$	$n=10$
$np \rightarrow np$	$s \lesssim 24 \text{ GeV}^2$	$n=10$
$\pi^-p \rightarrow \pi^-p$	$s \lesssim 60 \text{ GeV}^2$	$n=8$
$\pi^+p \rightarrow \pi^+p$	$s \lesssim 40 \text{ GeV}^2$	$n=8$
$K^-p \rightarrow K^-p$	$s \lesssim 20 \text{ GeV}^2$	$n=8$
$K^+p \rightarrow K^+p$	$s \lesssim 20 \text{ GeV}^2$	$n=8$

The intermediate energy data naturally separate into two different regimes: the *small angle* regime which is dominated by diffractive effects and is characterized by an exponential drop-off in transverse momentum; and the *wide angle* regime where one can hope to look for evidence for constituent models characterized by power-law scaling behavior. While the exponential drop-off and any fine structure in the small angle data is controlled by a length scale characteristic of the hadron size ( $\sim 1$  fermi), the wide angle data should be free of such a scale if they are indeed dominated by hard scattering, or equivalently short-distance, interaction between constituents.

Most of the analysis of the wide angle elastic scattering data has been carried out with a view to claim support for the predominance of the hard scattering mechanism at the available momentum transfers. The predictions of the "hard scattering model" can be restated in the form of two easily verifiable statements; (a) - *there is a factorization of the angular dependence and the energy dependence of the cross-section*, (i.e. the angular dependence is a universal function of  $\theta_{c.m.}$  independent of energy) and (b) - *the cross-section falls with*

energy as a fixed, integral power of  $s$  (the model also predicts this power for any given pair of hadrons). This "power-law scaling" hypothesis for the elastic cross-section can be expressed very simply:

$$\frac{d\sigma}{dt} \sim \frac{1}{s^n} f(\theta_{c.m.}) \quad (3.1)$$

As shown in the last chapter, the exact expression includes some logarithmic scale breaking which weakly modifies the power-law.

Figures 3.1 through 3.5 show the comparison of the above mentioned hard scattering predictions with the wide angle elastic data. It is quite remarkable that none of the data show any alarming deviations from these predictions. The fall-off with  $s$  at fixed large angles, of all the elastic cross-sections (Figs. 3.1-3.3), seems to be consistent with the value of  $n$  predicted by the hard scattering model. It should be mentioned, however, that the data do not allow an accurate determination of  $n$ . The errors in a fit to determine  $n$  can be anywhere between  $(\pm 0.5)$  to  $(\pm 1)$  depending on the set of data and the method used for estimating the error. The energy independence of the angular distributions can only be checked for rather small ranges of energy (Figs. 3.4, 3.5). Again there seems to be no major inconsistency between data and prediction, but again the errors are quite large, leaving room for other possibilities. Taken individually, it is difficult to take any set of data as convincing evidence for power-law scaling. However, if we consider all the elastic data and add to it the scaling observed in electromagnetic form factors, photon-hadron exclusive reactions and charge-exchange hadron scattering, then it *may* be safe to conclude that we are seeing the effects of *constituent interaction* in exclusive processes similar to those seen in high- $P_T$  data on inclusive processes. To see if the data lend strong support to any particular constituent model for elastic scattering requires a much more

Careful analysis, which we shall attempt in the remaining chapter.

By far the most extensively measured elastic scattering reaction is  $pp$  scattering. Not only are the data for this reaction the most accurate but they also extend to a much higher energy than the other cases. These features make  $pp$  data more suitable than others for a more careful analysis to look for evidence for any particular constituent model or even any other type of model. A quick perusal of the past literature shows that many different authors have analyzed  $pp$  data, and interestingly, they have arrived at widely differing conclusions about what model they support. In the recent past, the discovery of QCD factorization in exclusive processes and the success of hard scattering models in explaining many inclusive measurements has led to the wide spread belief, that power-law scaling in exclusive processes is a well established fact. However, it is important to study the different interpretations of the data and resolve the disagreements, before one can place confidence in the power-law scaling behavior of elastic scattering.

The often cited work on the analysis of  $pp$  data, that claims strong support for power-law scaling is the one carried out by Landshoff and Polkinghorne [7]. They use all the available data and plot the cross-section against  $s$  (on a logarithmic scale) for several different fixed c.m. angles (Fig. 3.6). The data seem to fit parallel straight lines very well, provided the following restrictions are imposed on them:

$$|t| \gtrsim 2.5 \text{ Gev}^2, \quad s \gtrsim 15 \text{ Gev}^2.$$

The slope of the straight lines corresponds to  $n=9.7$ . The lines were in fact positioned by eye and the error in  $n$  is approximately estimated to be  $\pm 0.5$ . These authors also carry out a fit to the data on angular dependence and they show

that for wide angles ( $0.6 \lesssim \sin \theta_{c.m.} \lesssim 1.0$ ) the cross-section falls with increasing angle as  $(\sin \theta_{c.m.})^{-14}$  (Fig. 3.7). Their analysis can then be summarized by the following expression for the elastic pp cross-section at wide angles:

$$\frac{d\sigma}{dt} \sim \frac{1}{s^{9.7}} \frac{1}{\sin^{14} \theta_{c.m.}} \quad (3.2)$$

The restriction imposed on  $|t|$  for the above fits is a reasonable one since we expect the data below  $|t|$ -values of 2.5 to be dominated by diffractive effects and Regge behavior. *However*, the restriction on  $s$  seems to be quite arbitrary, dictated by the desire to have a good fit for  $n$ . Theoretical arguments strongly suggest that the onset of hard scattering behavior should be determined by a threshold in  $t$ . Since fixing  $t$  determines  $s$  for a given angle one does not expect to have to impose a separate restriction on  $s$ . For  $90^\circ$  scattering this implies that scaling should begin at  $s \simeq 7 \text{ GeV}^2$  instead of  $s \simeq 15 \text{ GeV}^2$ .

The above comment is only meant to draw the attention of the reader to a possible shortcoming of the data analysis. We shall now examine some of the more serious criticisms of the scaling interpretation of elastic scattering data.

#### A. ABSENCE OF LOGARITHMIC SCALE BREAKING

A very serious defect in the scaling interpretation of pp data is the complete lack of evidence of logarithmic scale breaking expected from the running of the coupling constant (the cross-section contains a factor of  $\alpha_s^{10}$ ) and from the  $Q^2$ -evolution of the proton distribution amplitudes. Even the authors who quote the above data analysis as lending strong support to the hard scattering model for elastic scattering, qualify their positive statements with a mention of the puzzling absence of logarithmic deviations from the power-law fall-off. Brodsky [2] has been pushing the point of view that the lack of visible scale breaking

in the data implies that the QCD scale,  $\Lambda$ , is somewhat smaller than the value that has been extracted from the analysis of scale breaking in inclusive processes. He claims that  $\Lambda \lesssim 0.1 \text{ GeV}$  is consistent with all the elastic data. This should be compared with  $\Lambda \sim 0.2 \text{ GeV}$  favored by deep inelastic muon scattering and  $\Lambda \sim 0.4 \text{ GeV}$  favored by deep inelastic electron scattering. It is perhaps possible that part of the scale breaking in inclusive processes can be explained by the proper treatment of higher-twist effects and the inconsistency thereby avoided. However, our own analysis shows that the data do not allow  $\Lambda$  to be as high as Brodsky's claim, making the situation much more serious.

Considering the  $90^\circ$  fit to pp data, which extends through the range  $15 \lesssim s \lesssim 50$ , and using  $\Lambda = 0.1$  one can show that the coupling constant factor  $([\alpha_s(t)]^{10})$  in the cross-section changes by a factor of about 5, raising the predicted value of  $n$  by about 1.3. The data are *certainly* inconsistent with a line corresponding to  $n = 11.3$  ( $10.0 + 1.3$ ). If we assume that the data can tolerate  $n = 10.5$ , which is still beyond the quoted error in estimating  $n$ , then it can be shown that only  $\Lambda \lesssim 0.001$  ( $\Lambda^2 \lesssim 10^{-6}$ ) is allowed. If we use  $t/9$  (i.e. the average  $Q^2$  of the gluons in a hard scattering diagram) instead of  $t$  in the argument of  $\alpha_s$ , then the value of  $\Lambda$  goes down even further. *Such a small value of  $\Lambda$  is not acceptable in our present picture of hadronic phenomenon.*

If the above analysis leaves any doubts about the existence of a problem then a look at some recently measured, high statistics pp elastic scattering data (not used in the above mentioned analysis) should help to drive home the point even further. This is the data of Jenkins *et al.* (1979) [8] taken in an experiment at ANL. A mathematically rendered fit to the  $90^\circ$  data for the range  $12 \lesssim s \lesssim 19 \text{ GeV}^2$  (see Fig. 3.8) gives  $n = 10.07 \pm 0.11$  (with a  $\chi^2$  of 30 for 24 degrees of freedom). If we again assume  $\Lambda \sim 0.1$  then the coupling constant factor raises the expected value of  $n$ , in this energy range, by 1.5 units above the dimensional



counting prediction. This means that hard scattering should result in  $n=11.5$ , which differs from the experimental value of  $n$  by more than *ten* times the error quoted on the fit. The hard scattering interpretation of these data analysis will force a ridiculously small limit on the value of  $\Lambda$ .

A comment on the qualitative features of the data may also be of some relevance to this issue. Since logarithms change faster at smaller values of their argument, we should expect to see a small downward-pointing convexity in these high statistics data, if the prediction of the hard scattering model is indeed being followed by it. This does not seem to be the case at all. If anything, the data seem to suggest a slight upward convexity. If we further argue that data below  $12 \text{ GeV}^2$  should also be in the hard scattering regime, then there is a definite upward convexity shown by the data, which is opposite of what logarithmic scale breaking leads us to expect. Proponents of power-law scaling must resolve this problem if they are to maintain their optimism. We shall return to this anomaly later in the review.

## B. PERSISTENCE OF FINE STRUCTURE

Another source of controversy in the interpretation of pp data stems from the *fine structure* that seems to be present in the high- $P_T$  data all the way up to the highest energies measured for wide angle scattering. A closer look at the fixed angle plot of  $\ln(d\sigma/dt)$  vs  $\ln(s)$  shows that the data slowly oscillate around the straight line fit. This oscillation cannot be discounted as a random fluctuation, and its systematics have been studied by more than one author. Though they differ in detail, the general conclusion of these analyses is that the oscillations are a strong indication of the presence of a *length scale* in the wide angle data, and that this scale is the same as the one that manifests itself in the small angle regime ( $R \sim 1$  fermi). We mention, below, some details of two different

analyses of this fine structure.

Schrempp and Schrempp [9] claim that fixed angle pp data are better described by a falling exponential in transverse momentum ( $\exp(-bp_1)$ ) than by a power-law fall-off in  $s$ . Their fit does look just as good as the power-law fit (Fig. 3.9) and it has the extra advantage of not requiring an arbitrary restriction on the energy-range used for the fit (power-law fit needs  $s \gtrsim 12 \text{ GeV}^2$ ). The length scale in the exponent,  $b$ , varies slowly with the angle. The authors then show that the oscillations around this line can be fit by a sinusoidal curve (Fig. 3.10) with a period corresponding to the hadronic radius ( $\sim 1$  fermi). This behavior of exclusive data (exponential drop-off with regular oscillations) is characteristic of a *geometrical* picture rather than a *constituent* one. One way to make a compromise between the two different interpretations is to state that we are in a transition region where the constituent effect provides a power-law fall-off in the higher energy region, but the effect of the hadronic size is not completely lost and manifests itself in the oscillating fine structure. It is interesting to note that similar oscillations can also be observed in  $\pi^-p$  data (Fig. 3.11), though the range and accuracy of the data is not sufficient for a good analysis.

The second author, A.P.Hendry [10], is also of the opinion that wide angle pp data *does not* provide convincing evidence for the power-law scaling prediction,  $d\sigma/dt \sim s^{-n} f(\theta)$ . He interprets the oscillations in the fixed angle plot as breaks or small dips in the pp scattering cross-section (see Fig. 3.12), of the same kind that have been recognized and interpreted in low energy data for a long time. These breaks are constant in  $t$  as we change the scattering angle and Hendry shows that they can be explained in the context of an optical model with diffractive and peripheral pieces. This interpretation again suggests the presence of a non-negligible *geometrical (soft subprocess dominated)* component in the wide angle high energy data. The same model as above is also shown, by the

author, to work for wide angle  $\pi^+p$  and  $\pi^-p$  elastic scattering. As to the possibility of a power-law scaling description for the averaged out  $s$ -dependence of fixed angle data, Hendry points out that rough lines through the whole range of data are convex up, (as are the segments between any two breaks in the data). *This suggests that  $(d\sigma/dt)_\theta$  falls slightly faster than a fixed power of  $s$ .* In addition the author notices that the rough lines for different angles are not quite parallel and therefore *the factorization of the  $s$  and  $\theta$  dependence of the cross-section is only rather approximate.*

Even if the fine structure merely indicates the presence of a small non-scaling component in the elastic scattering amplitude, which will eventually disappear as we go to even higher energies, the two observations stated at the end of the last paragraph present further obstacles to the hard-scattering-model enthusiasts. Both of these *systematic deviations* from power-law scaling in elastic scattering data have been noticed by several authors in the past. We shall review them, one by one.

### C. CHANGE OF $n$ WITH ENERGY

The increase in the value of  $n$  for a power-law fit to  $(d\sigma/dt)_\theta$  with increasing energy was first pointed out in the analysis of Barger *et al.* [11]. They show that for a power-law fit to the wide angle data, changing the low energy cut-off from  $s \gtrsim 7 \text{ GeV}^2$  to  $s \gtrsim 18 \text{ GeV}^2$  changes the value of  $n$  from  $\sim 9.3$  to  $\sim 10$  (see Fig. 3.15). This fact, by itself, could be interpreted as just a delay in the asymptotic approach to power-law scaling, but it has been noticed that the data-points at the highest energies systematically lie below the power-law fits and seem to prefer an even higher value of  $n$ . In two different analyses, one by Schrempp and Schrempp [9] (Fig. 3.13) and the other by Gunion *et al.* [6] (Fig. 3.14), it is shown that straight lines with  $n=12$  describe the highest energy data

( $s \gtrsim 30 \text{ GeV}^2$ ) extremely well. (This was once cited as evidence for the CIM mechanism!)

A similar observation has been made by Jenkins *et al.* [8] for  $\pi^-p$  scattering, though the energy range of the data used in their analysis is rather limited and does not permit an equally confident statement. The following is a result of power-law fits, to  $90^\circ$  data, with three different low-energy cut-offs:

$10 \leq s \leq 19 \text{ GeV}^2$	$n = 5.69 \pm 0.12$
$12 \leq s \leq 19 \text{ GeV}^2$	$n = 6.67 \pm 0.22$
$14 \leq s \leq 19 \text{ GeV}^2$	$n = 8.32 \pm 0.33$

These numbers suggest that the energy dependence becomes steeper with increasing energy and, furthermore, there is no indication that  $n$  stops increasing at 8. This trend is also present in their  $\pi^-p$  data at *other* large angles.

A very recent measurement of  $\pi^-p$  elastic scattering at  $s = 40 \text{ GeV}^2$  and  $s = 60 \text{ GeV}^2$  by Almas *et al.* (1980) [12] confirms this trend without leaving any room for doubt. They combine their  $90^\circ$  data at these two high energies with the  $90^\circ$  data at  $s \sim 19 \text{ GeV}^2$  from Ref.[13] and compute  $n$  to be  $9.5 \pm 0.5$ ! There is thus a close parallel between the  $\pi^-p$  and  $pp$  data, and in each case *the predicted value of  $n$  is only obtained if one restricts the fit to a small energy range in the middle*. The data for other elastic reactions are too limited to look for similar trends, but one should note in passing that the isolated data point at  $s = 20 \text{ GeV}^2$  in  $K^+p$  scattering lies far below the  $1/s^8$  fit to the lower energy ( $s \lesssim 10 \text{ GeV}^2$ ) data (Fig. 3.2).

#### D. CHANGE OF $n$ WITH ANGLE

The *second* objection to the scaling interpretation, (perhaps even more worthy of concern than the first), is the lack of factorization in the  $s$  and  $\theta$  dependence of the cross-section, manifested by *the change of  $n$  with angle*. This problem again has been noticed by several authors and it, too, was first brought to attention by the analysis of Barger *et al.* [11], who made a plot of  $n$  vs  $\theta_{c.m.}$  all the way from  $\theta_{c.m.}=0.6^\circ$  to  $\theta_{c.m.}=90^\circ$  ( $n$  is computed from fits with  $s \gtrsim 7 \text{ GeV}^2$ ) (see Figs. 3.15, 3.16). For our purposes, the plot is only relevant for  $\theta_{c.m.} \gtrsim 40^\circ$  ( $\cos\theta_{c.m.} \lesssim 0.75$ ) because the data for smaller angles is not well described by a power-law fit ( $|t|$  is too small for these angles). In the relevant region of the plot, the value of  $n$  rises monotonically from 6.8 to 9.3, and  $n$  can only be considered to be approximately constant for angles very close to  $90^\circ$ . To help remove any lingering doubts about the existence of a *real* problem, one can again look at the high statistics pp data of Jenkins *et al.* [8]. Their analysis gives  $n=9.21 \pm 0.13$  for  $\theta_{c.m.}=75^\circ$  compared to  $n=10.07 \pm 0.11$  for  $90^\circ$ . Similar analyses of available data on other elastic scattering reactions confirms this trend of a decrease in  $n$  for decreasing angle, even more convincingly. The following tables summarize the results of such analyses for three different reactions: The data for np elastic scattering is taken from Ref. [14].

$pp \rightarrow pp$  ,  $12 \leq s \leq 19 \text{ GeV}^2$

$\theta_{\text{c.m.}}$	$n$
90°	10.07±0.11
85°	10.05±0.11
80°	9.74±0.11
75°	9.21±0.13

$\pi^-p \rightarrow \pi^-p$  ,  $14 \leq s \leq 19 \text{ GeV}^2$

$\theta_{\text{c.m.}}$	$n$
105°	6.52±0.89
100°	6.79±0.49
95°	6.96±0.29
90°	8.32±0.33
85°	8.22±0.29
80°	7.34±0.29
75°	6.63±0.29

$np \rightarrow np$  ,  $10 \leq s \leq 24 \text{ GeV}^2$

$\theta_{c.m.}$	$n$
120°	$8.10 \pm 0.22$
90°	$10.40 \pm 0.34$
60°	$8.04 \pm 0.15$

The numbers shown in these tables point to a universal trend in high- $P_T$  elastic scattering; the cross-section falls with  $s$  most rapidly at 90° and the steepness decreases for angles both below and above this value. The results for  $\pi^+p$  scattering have large errors and are not listed above, but they too show a similar trend.

For the hard headed skeptics who may still harbor doubts in their minds about the failure of the factorization hypothesis we again refer to the recent  $\pi^-p$  measurements by Almas *et al.* [12] compute  $n$  for two angular ranges by combining their high energy data with the data of others at lower energies. For  $0 < \cos\theta_{c.m.} < 0.45$  they deduce  $n = 9.5 \pm 0.5$ , and for  $0.45 < \cos\theta_{c.m.} < 0.6$  the fitted value of  $n = 8.0 \pm 0.3$ . This is a very significant difference and that too in an energy range where we expect sub-asymptotic effects to have become negligible.

In conclusion then, our review of high- $P_T$  wide angle elastic data suggests that there is a significant geometrical (or non-constituent-model) component in the scattering amplitude at the measured energies, which produces fine structure in the data; but *even in the average sense the data are not well described by the power-law scaling hypothesis*, though their fall with energy at 90° and at intermediate energies is closely approximated by the hard-scattering prediction (assuming a very small  $\Lambda$ ). If the closeness of the measured value of  $n$  to its

scaling value is not a complete accident then the averaged out data could well be giving indications of constituent scattering but the amplitude involved may not be as simple as the one derived in the hard scattering model, and may involve the hadronic length scale in an important way.

### 3.2. HIGH ENERGY, SMALL ANGLE DATA

In the last few years, elastic scattering measurements for  $\pi^-p$  and  $pp$  have been carried out at Fermilab energies [15,16,17], and for  $pp$  also at ISR energies [18]. At these high energies ( $s \gtrsim 400 \text{ GeV}^2$ ), the elastic cross-section at wide angles is too small to be measurable and the data have to be restricted to small angles. However, fairly large values of  $|t|$  can still be achieved ( $|t| \lesssim 11 \text{ GeV}^2$  for  $\pi^-p$  and  $|t| \lesssim 15 \text{ GeV}^2$  for  $pp$ ), thus providing an opportunity to verify the predictions of constituent scattering models.

The high energy data have been measured at only a few chosen values of  $s$ . Since the angular range of these data is not compatible with the range of the intermediate energy data, the high energy data are not suitable for extending the fixed-angle energy-dependence analysis to check the validity of power-law scaling at these energies. However, the  $t$ -ranges of the two classes of data *are* compatible, and by combining the intermediate and high energy data we can study the *fixed- $t$*  energy-dependence of the elastic cross-section for a very large range of energies. As discussed in the last section of the theory review, this analysis should reveal the asymptotic form of the scattering amplitude in the limit  $t/s \rightarrow 0$ . The approach to this asymptotic form can provide important information on the relative contribution of quark-exchange and gluon-exchange scattering mechanisms.



### A. DATA FOR pp SCATTERING

Fig. 3.17 shows the variation of the pp elastic cross-section with  $s$  for several different values of  $t$ . The data points in this plot are taken from many different experiments and the curves are drawn to guide the eye. For smaller energies the fixed  $t$  cross-section falls quite rapidly but at the highest available energies it seem to be approaching an energy-independent value. Notice also, that for smaller values of  $|t|$  the cross-section levels off at the highest measured energies but for higher  $|t|$  it is still falling in that range. This strongly suggests that the approach to an asymptotic value is governed by the ratio  $t/s$ . This fact is consistent with scaling since the function  $f(\theta_{c.m.})$  in Eq. (3.1) can always be expanded in powers of  $t/s$ . Note however that for  $-t=3.6 \text{ GeV}^2$  the asymptotic region is not reached until  $s \sim 2000 \text{ GeV}^2$ . Thus, if we express the cross-section as a sum of a part that is independent of  $s$  and a part that has a factor of  $t/s$  in it, then the second part must have a coefficient much larger than the first. We can study this property of the data more carefully in the context of the hard scattering model.

Using the known asymptotic forms of amplitudes corresponding to quark-exchange and gluon-exchange diagrams, and assuming dimensional scaling we can express the pp elastic scattering cross-section as follows:

$$\frac{d\sigma}{dt}_{pp} \sim \frac{1}{s^2} \left[ c_g \frac{s}{t^5} + c_q \frac{1}{t^4} \right]^2 \quad (3.3)$$

We can now fit this expression to the small angle data and evaluate the constants  $c_g$  and  $c_q$ . This has been done in the analysis of Lepage and Brodsky [ ], who make a fit for the data at three energies ( $s \sim 400, 800, \text{ and } 3000 \text{ GeV}^2$ ) and for a large range in  $t$  ( $5 \text{ GeV}^2 \lesssim |t| \lesssim 15 \text{ GeV}^2$ ). The fits are shown in Fig. 3.18. A coupling constant factor with  $\Lambda=0.1 \text{ GeV}$  is included in the fits. The authors express

the two constants in dimensionless units by dividing each of them with  $t^4 G_M^2(t)$ , which is a constant in the large  $t$  limit ( $G_M(t)$  is the proton's magnetic form factor). They then find  $c_g \simeq 8$  and  $c_q \simeq 510$ , so that the ratio  $c_q/c_g \simeq 64$ . *This ratio is much greater than 1* and calls for some explanation if we are to retain our faith in the hard scattering model. Since the numbers of the two kinds of diagrams are comparable, this situation can only come about if the intrinsic normalization of quark-exchange diagrams is much larger than that of the gluon-exchange diagrams. This of course was the main assumption of the CIM model. As we shall see, our own calculations for  $\pi\pi$  scattering do not bear out this assumption, thus raising serious doubts about the credibility of the model that leads to Eq. (3.3).

If we look more carefully at the plots in Fig. 3.17 we see that in the intermediate energy range, where the  $c_q$ -component of the scattering amplitude is expected to dominate completely, the cross-section is falling much more rapidly than  $1/s^2$ . This is not surprising because the form in Eq. (3.3) only holds in the asymptotic region and presumably  $t/s$  is not small enough in the intermediate region. One way, in which to better appreciate this possibility is to take the phenomenological form for the wide-angle cross-section established by Landshoff and Polkinghorne (Eq. (3.2)) and expand it in powers of  $t/s$ . This exercise yields,

$$\frac{d\sigma}{dt_{pp}} \sim \frac{1}{s^{2.7}t^7} \left[ 1 + 7 \frac{|t|}{s} + 21 \frac{t^2}{s^2} + \dots \right] \quad (3.4)$$

It is quite clear from the above expression that the first term of the series is not a good parameterization of the cross-section unless  $t/s$  is quite small (at least less than 0.1). Despite this fact, Lepage and Brodsky (Ref. [ ]) use the form in Eq. (3.3) to compute  $c_q$  for some  $90^\circ$  data at intermediate energies. Not surprisingly, they find  $c_q \sim 5000$  in the same units as those used for the high energy fit

above. We feel that this result is not meaningful, and is not a direct measure of the number of hard scattering diagrams, that get summed to make up the elastic scattering amplitude, as is triumphantly claimed by these authors.

Lastly we mention that some authors [19] have suggested that high energy data, if plotted at fixed- $s$  as a function of  $t$ , seems to fit rather well the form  $1/t^8$  (scaling predicts  $1/t^{10}$  for an energy independent cross-section). This fit is shown in Fig. 3.19. They claim that this may be an indication of the dominance, at these energies, of the unsuppressed pinch contribution. We would like to point out that the good fit could easily be caused by the presence, in significant amount, of the  $c_q$ -component of the scattering amplitude (which falls as  $1/t^8$  for constant  $s$ ), since most of the data used are at higher values of  $|t|$  where the cross-section has not yet achieved energy-independence. The viability of this argument is well illustrated by the fits of Lepage and Brodsky (Fig. 3.18) which describe the data just as well as the  $1/t^8$  fit does. There is still the possibility that the energy independent part of the cross-section is due to the pinch diagrams rather than the hard scattering ones (both contributions are independent of  $s$  and only differ in the power of  $t$  involved). Without the availability of more accurate and higher energy data, this question cannot be settled experimentally.

## B. DATA FOR $\pi^-p$ SCATTERING

The high energy, large  $|t|$  data for  $\pi^-p$  elastic scattering are rather limited and do not permit very many firm conclusions. One of the problems with analyzing these data to look for hard scattering effects is the fact that diffraction structures in the data extend to higher values of  $|t|$  than they do in  $pp$  scattering. While the fixed- $s$  plot of high energy  $pp$  data [18] (Fig. 3.21) has a small dip at  $-t=1.4 \text{ GeV}^2$  and is very smooth after  $-t \sim 2 \text{ GeV}^2$ , the  $\pi^-p$  plot (Fig. 3.22), at an

$s$ -value of  $\sim 400 \text{ GeV}^2$  [15], has a large dip at  $-t=4 \text{ GeV}^2$  followed by a peak at  $-t \sim 5 \text{ GeV}^2$  and is expected to be smooth only after about  $6 \text{ GeV}^2$ . Thus there is only a small region of  $t$  where we can study the fixed- $t$  energy dependence to look for the relative size of different hard scattering contributions.

Fixed- $t$  plots of the  $\pi^-p$  cross-section, such as the one we just analyzed for  $pp$  data, have been made for  $s \lesssim 45 \text{ GeV}^2$  and  $t \lesssim 4.5 \text{ GeV}^2$  [20] (Fig. 3.20). The dip at  $-t=4$  does not exist at these energies and since  $t/s$  is fairly small, it may be reasonable to look for evidence for the small angle prediction for the  $\pi^-p$  cross-section, in these plots. The small angle prediction for meson-baryon scattering is given by,

$$\frac{d\sigma}{dt}_{\pi p} \sim \frac{1}{s^2} \left[ c_g \frac{s}{t^4} + c_q \frac{1}{t^3} \right]^2 \quad (3.5)$$

where the constants  $c_g$  and  $c_q$  now have different values. The plots in Fig. 3.20 have a character very similar to the ones for  $pp$  data. For small  $|t|$  the cross-section attains energy independence at the highest energies but the larger  $|t|$  data are still falling quite rapidly. If we decide to ignore data for  $|t| \lesssim 2.5$ , as was done for the  $pp$  case, then only two values of  $t$  ( $-t=3.5$ ,  $-t=4.5$ ) are left to consider. For both these values the cross-section is still falling faster than  $1/s^2$  at  $s \sim 45 \text{ GeV}^2$ , indicating that we are far away from the asymptotic region and the form in Eq. (3.5) is not yet applicable.

Fixed- $t$  plots for higher values of  $|t|$ , and up to higher energies, should provide a more meaningful comparison with hard scattering predictions. Even though data at high  $|t|$ 's are available over a large energy range, such plots do not exist in the published literature. We have therefore made our own plots for  $-t=8 \text{ GeV}^2$  and  $-t=10 \text{ GeV}^2$  (Fig. 3.23), which  $t$ -values are away from the dip region allowing us to use the highest energy data. The plots show that even at

the highest measured energy ( $s \sim 400 \text{ GeV}^2$ ), the cross-section is still falling, though the slope is rapidly decreasing and may finally go to zero. If Eq. (3.5) is fitted to the data we again expect to get a large value for  $c_q/c_g$ , though it may be somewhat smaller than the one obtained for pp scattering.

### 3.3. CONCLUDING REMARKS

Our review of both intermediate and high energy elastic scattering data suggests, that the belief that quark-exchange hard-scattering is the dominant mechanism in wide-angle scattering is *not* compatible with the behavior of the data, when examined over a large range of energies and angles. The data do have some characteristics of constituent scattering (approximate power-law fall-off), but they are not quite free of an intrinsic scale and *the scale breaking is more serious than a logarithmic modification*. On a concluding note we would like to add that the success claimed for reproducing the angular dependence of the cross-section by CIM calculations is far from impressive. The calculations include a lot of free parameters and cannot reproduce any of the detailed structure seen in  $\pi p$  and  $np$  scattering data. There is also no evidence for the presence of Landshoff's multiple scattering mechanism (without Sudakov effects) in the elastic data, which differs from hard scattering mostly because of a different prediction for  $n$  ( $n=8$  for baryon-baryon scattering and  $n=7$  for meson-baryon scattering).

Perhaps the data is indicating the presence of a completely different kind of mechanism, or perhaps a more careful treatment of the hard scattering model will produce the required deviations from the overly simple power-law scaling hypothesis. Whatever be this mechanism, both pp and  $\pi^-p$  elastic data suggest that the magnitude of its contribution at intermediate energies is much

greater than the magnitude of the energy independent contribution. A detailed calculation of the diagrams contributing to the hard scattering amplitude could be of enormous help in resolving some of these issues.

FIGURE CAPTIONS

- Fig. 3.1 Power-law fit for pp and np elastic scattering (figure taken from Ref. [14]).
- Fig. 3.2 Comparison of  $K^+p$  elastic data with the hard scattering prediction (figure from Ref. [1]).
- Fig. 3.3 Comparison of  $\pi^-p$  and  $\pi^+p$  data with the scaling prediction [8].
- Fig. 3.4 The angular dependence of  $s^{10}(d\sigma/dt)$  and  $d\sigma/dt$  for pp elastic scattering [1].
- Fig. 3.5 The angular dependence of  $s^8(d\sigma/dt)$  and  $d\sigma/dt$  for some meson-proton elastic reactions [1].
- Fig. 3.6 Power law fits to fixed angle pp scattering [7]. The straight lines are positioned by eye and the value of  $n$  is found to be  $9.7 \pm 0.5$ .
- Fig. 3.7 Angular dependence of the pp cross-section [7]. The straight line through the data corresponds to  $f(\theta) \sim (\sin\theta)^{-14}$ .
- Fig. 3.8 Power law fit to the high statistics pp data of Ref. [8].

- Fig. 3.9      Exponential fits to pp elastic scattering data [9].
- Fig. 3.10     A sinusoidal fit to the oscillations of pp data around the exponential fit [9].
- Fig. 3.11     A plot of  $s^B(d\sigma/dt)$  against  $s$  for  $\pi^-p$  scattering. The data may be giving some indication of oscillations [8].
- Fig. 3.12     Plots of fixed angle pp scattering showing dip structure [10].
- Fig. 3.13     Plots showing that the  $n=12$  fit is better than the  $n=10$  fit for highest energy pp data [9].
- Fig. 3.14     Another comparison of the two possible fits to pp data. This figure is from Ref. [6].
- Fig. 3.15     Power law fits to fixed angle pp elastic scattering data [11].
- Fig. 3.16     Plot of  $n$ , determined from the fits of Fig. 3.15, as a function of  $\cos(\theta_{c.m.})$ .
- Fig. 3.17     Fixed- $t$  plots of the pp elastic scattering cross-section as a function of energy.



Fig. 3.18 Fits of the high energy pp data to the form in Eq.(3.3).

Fig. 3.19 A fit of the high energy pp data to the prediction of the Landshoff mechanism.

Fig. 3.20 Fixed- $t$  plots of the  $\pi^-p$  data as a function of energy.

Fig. 3.21 The pp cross-section as a function of  $t$  at  $\sqrt{s}=53$  Gev.

Fig. 3.22 The  $\pi^-p$  cross-section as a function of  $t$  at  $s \simeq 400$  Gev<sup>2</sup>.

Fig. 3.23 Fixed- $t$  plots of  $\pi^-p$  data for  $t=8$  and  $t=10$  Gev<sup>2</sup>.

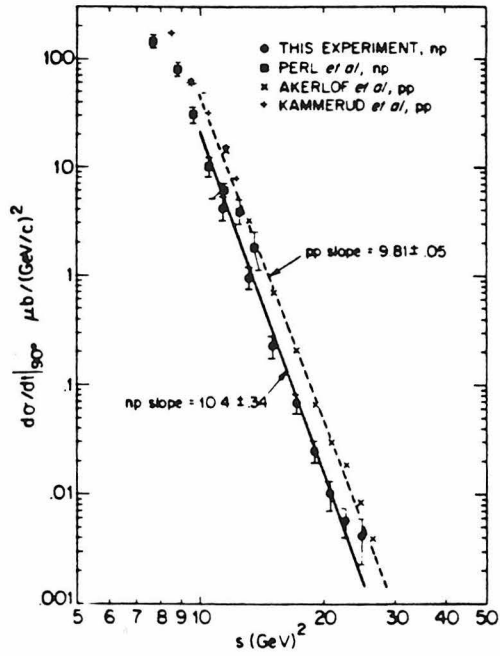


Fig. 3.1

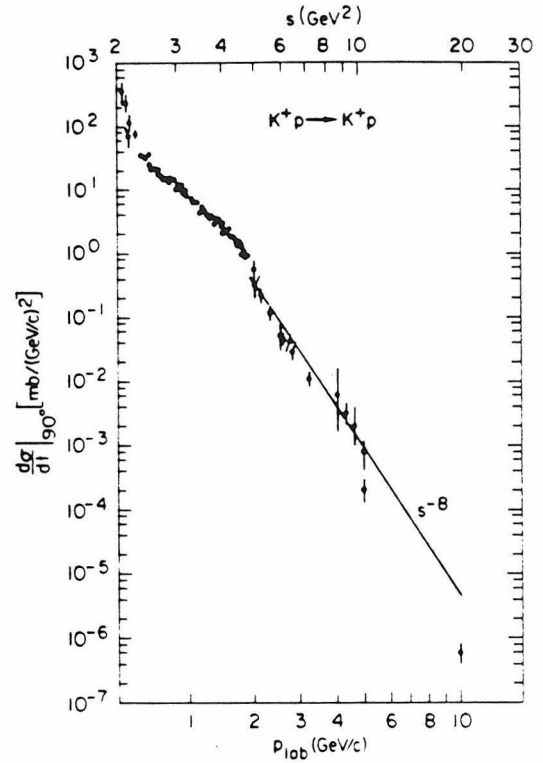


Fig. 3.2

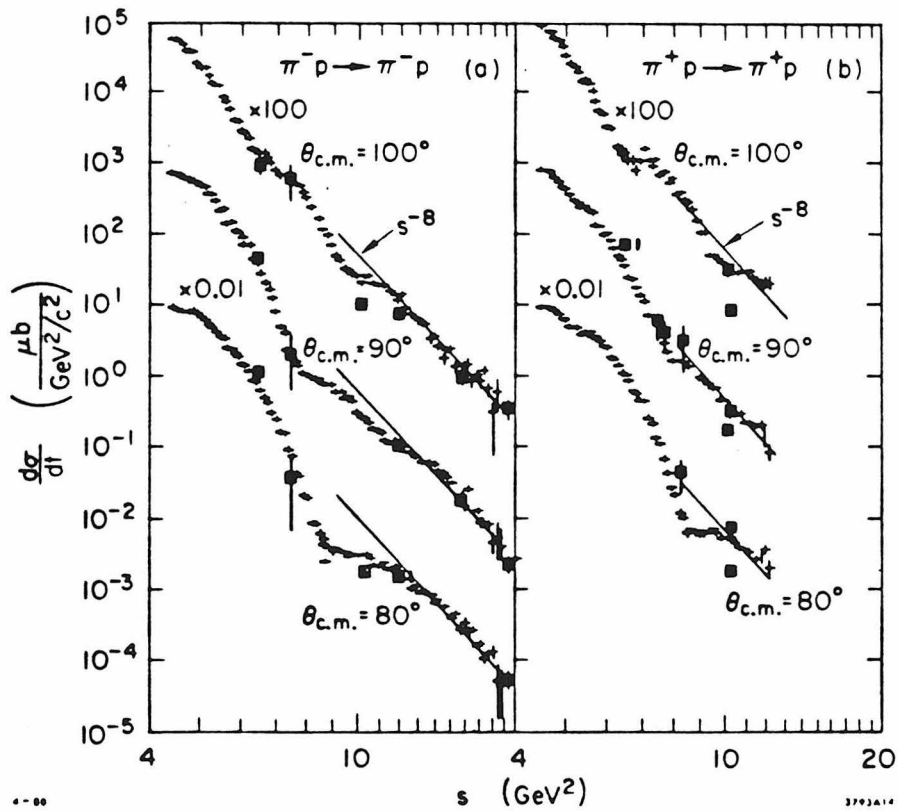


Fig. 3.3

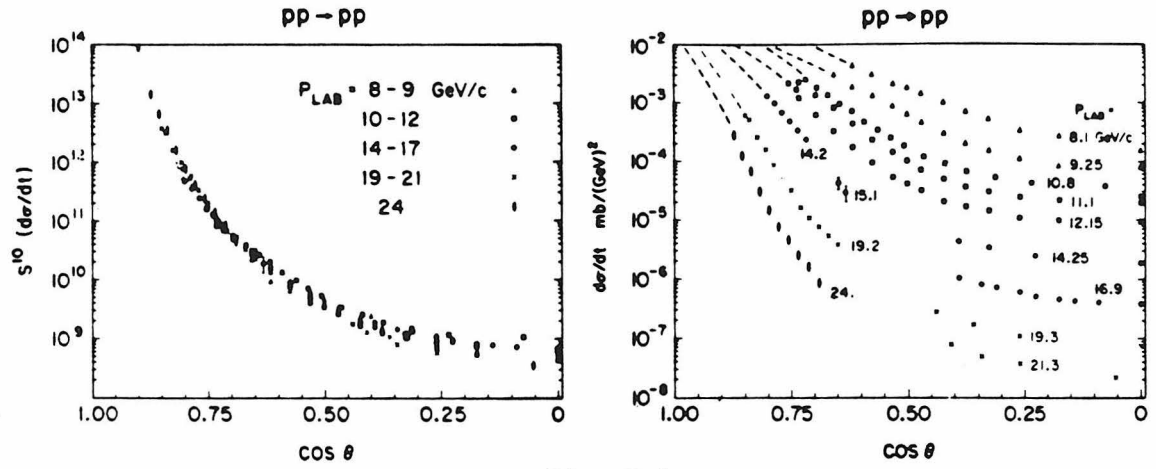


Fig. 3.4

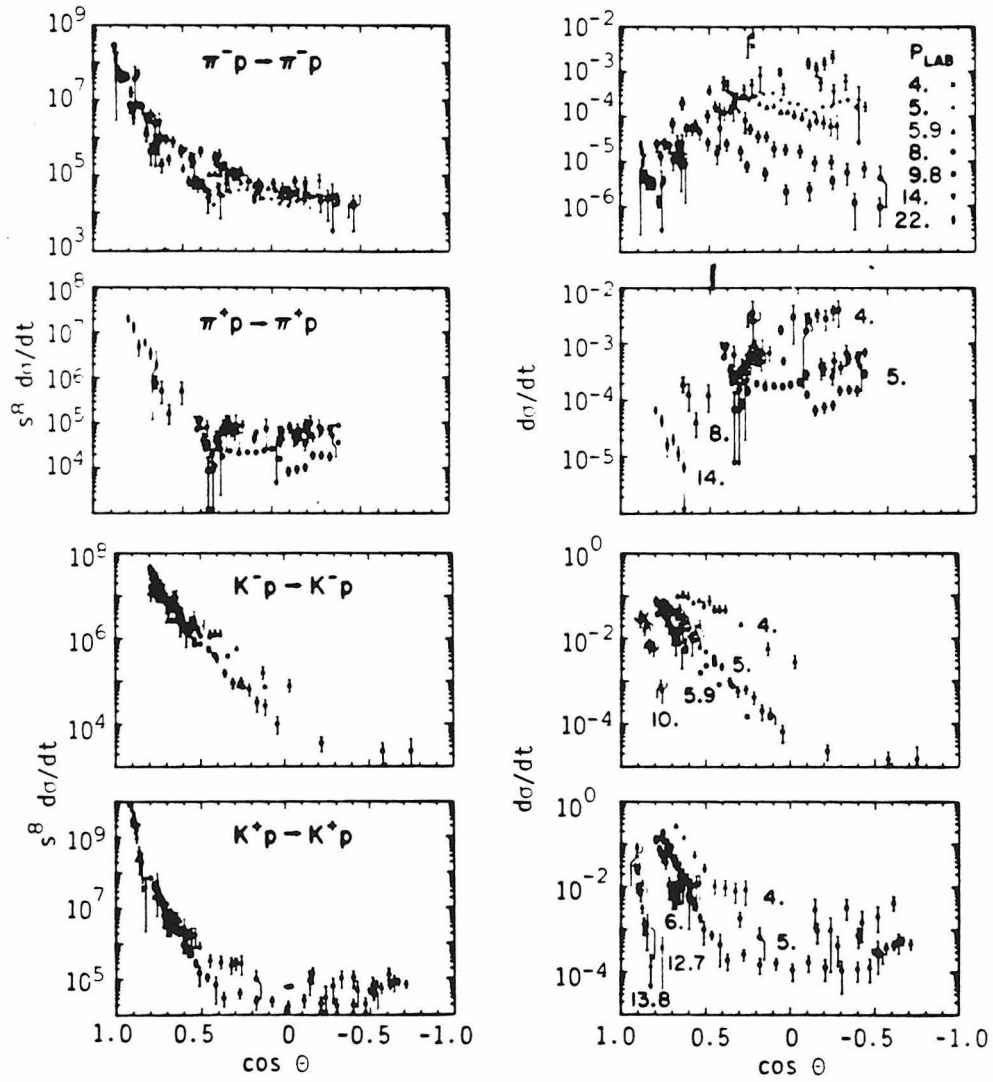


Fig. 3.5

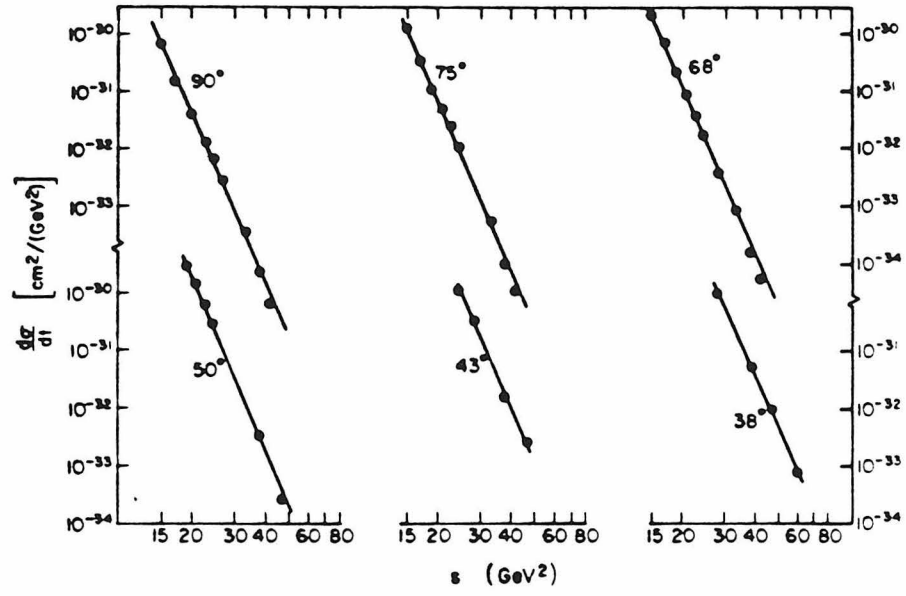


Fig. 3.6

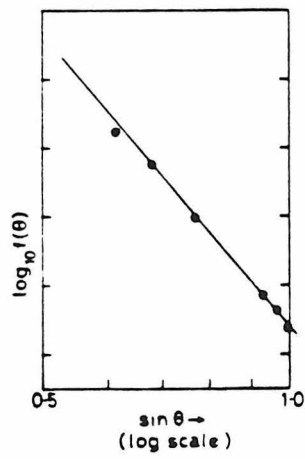


Fig. 3.7

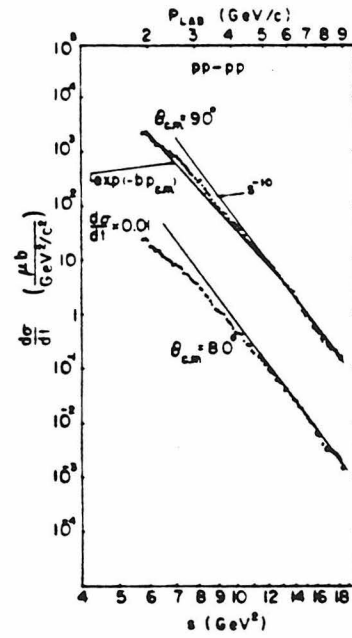


Fig. 3.8

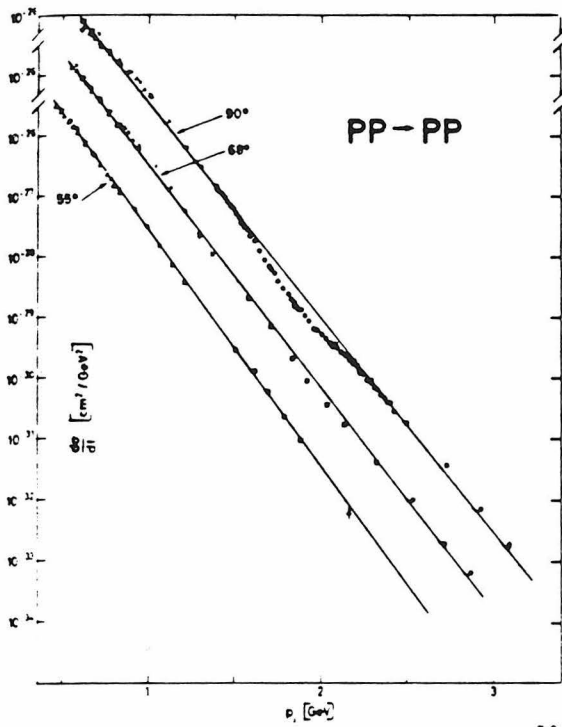


Fig. 3.9

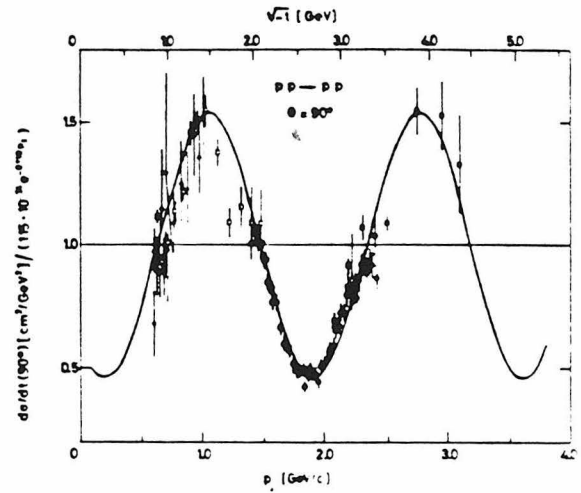


Fig. 3.10

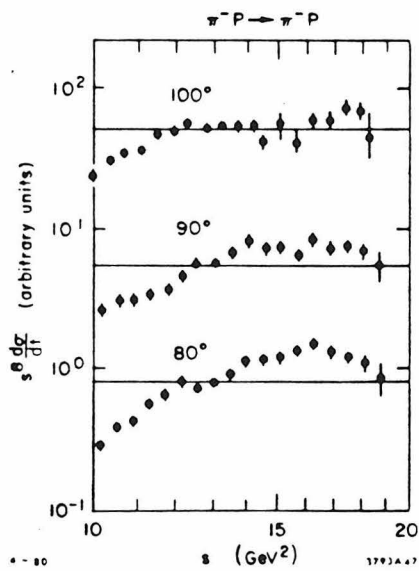


Fig. 3.11

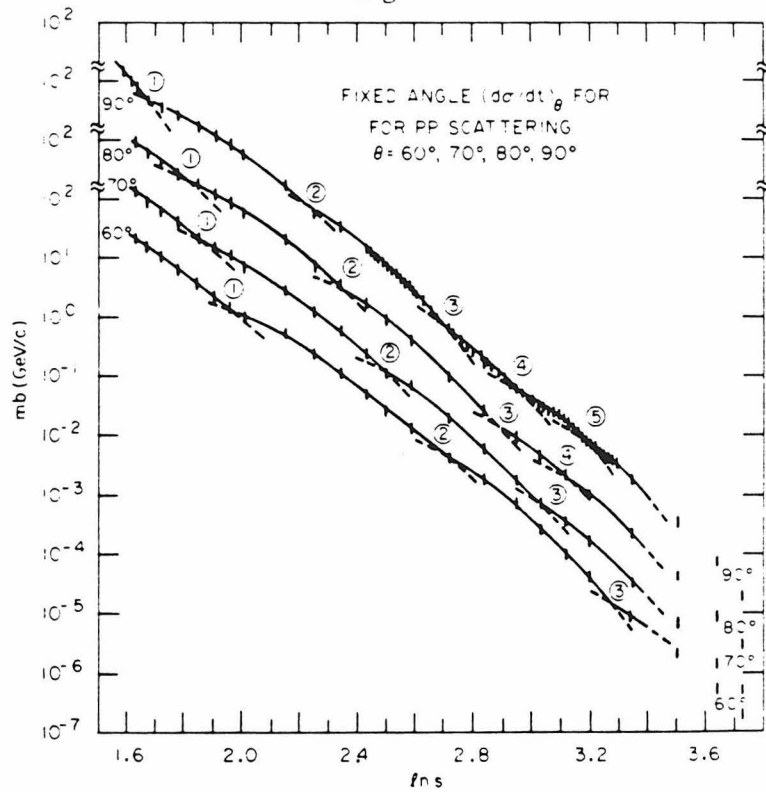


Fig. 3.12

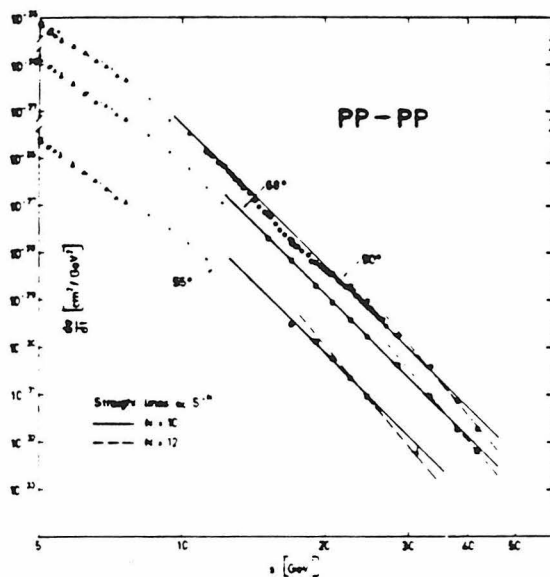


Fig. 3.13

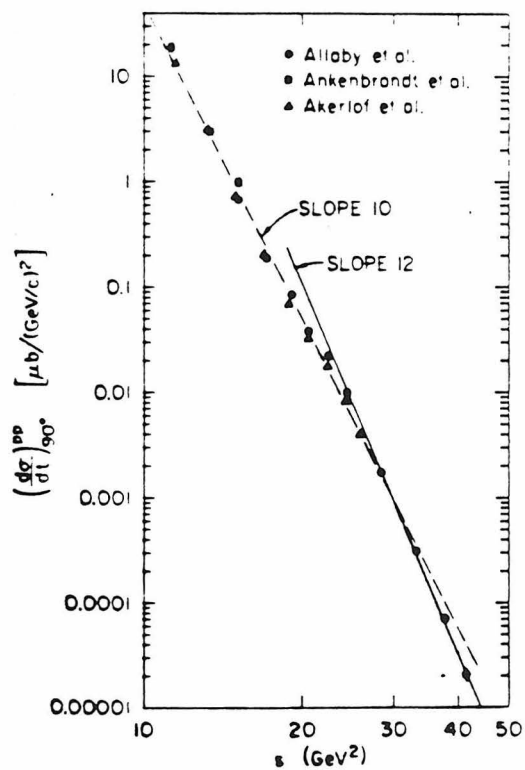


Fig. 3.14

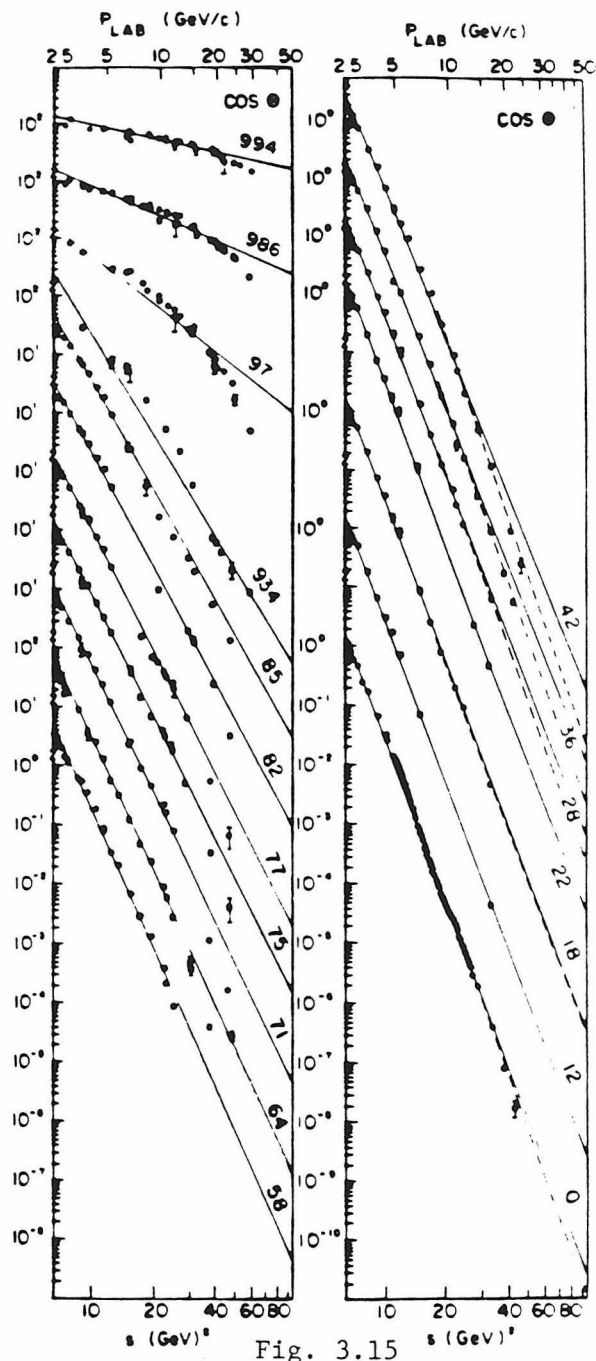


Fig. 3.15

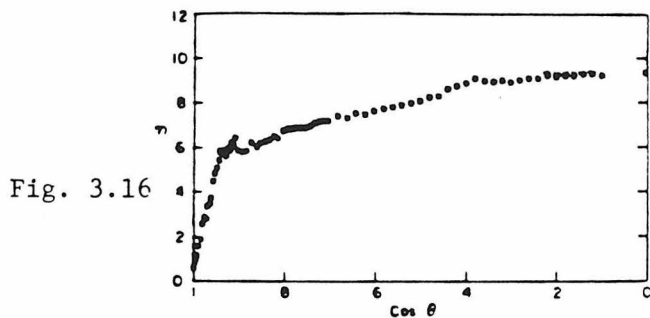


Fig. 3.16

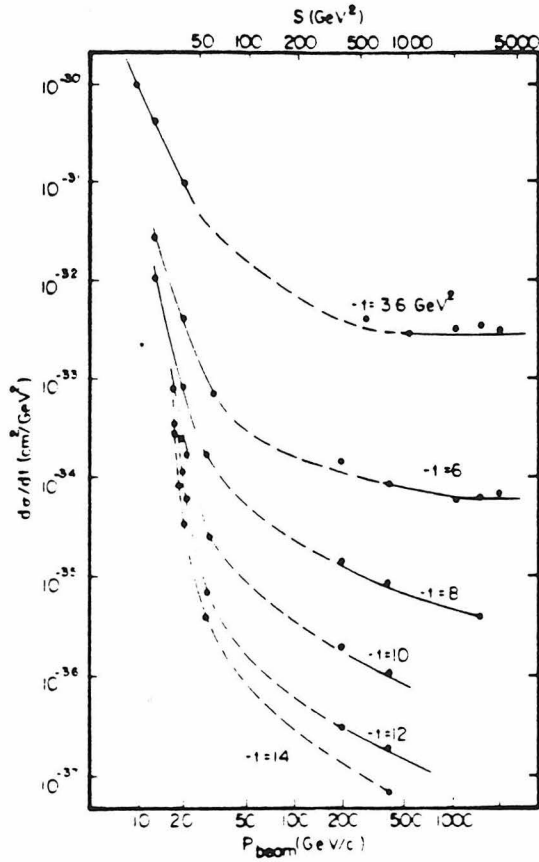


Fig. 3.17

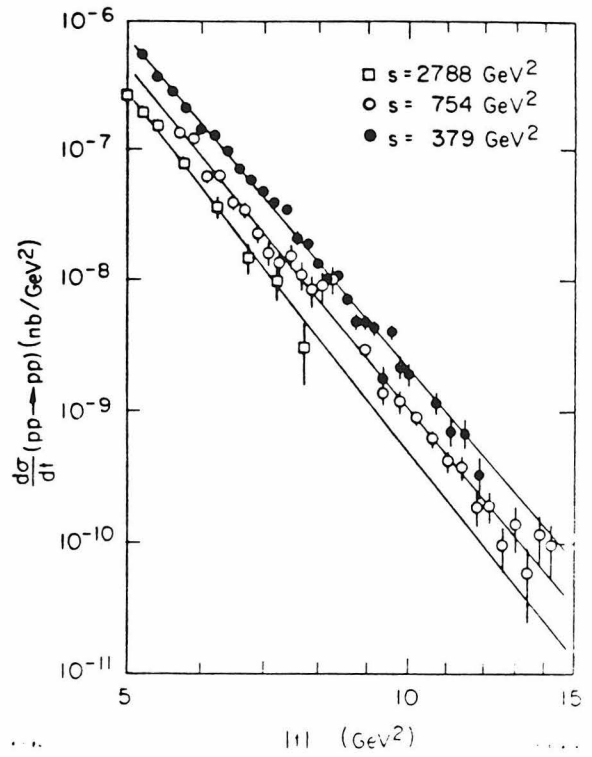


Fig. 3.18

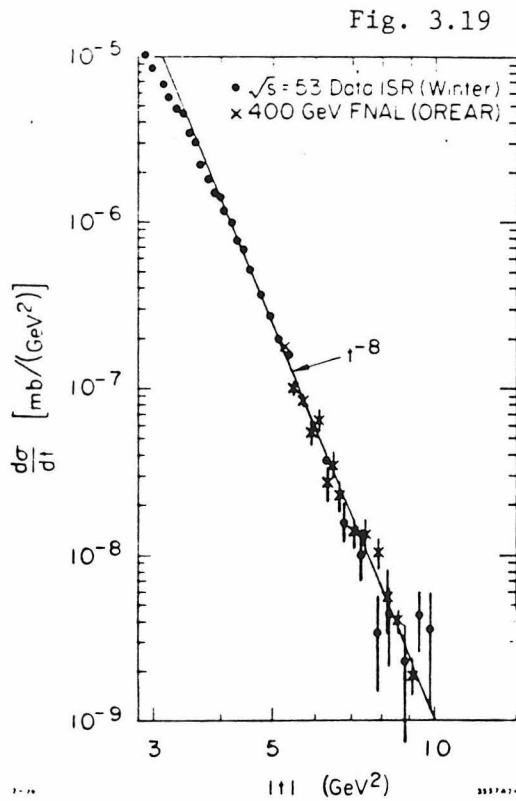


Fig. 3.19

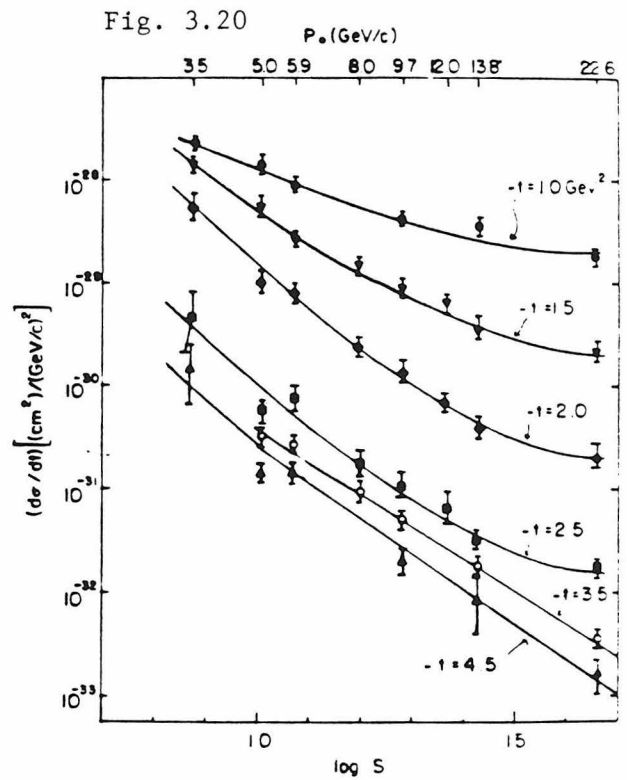


Fig. 3.20

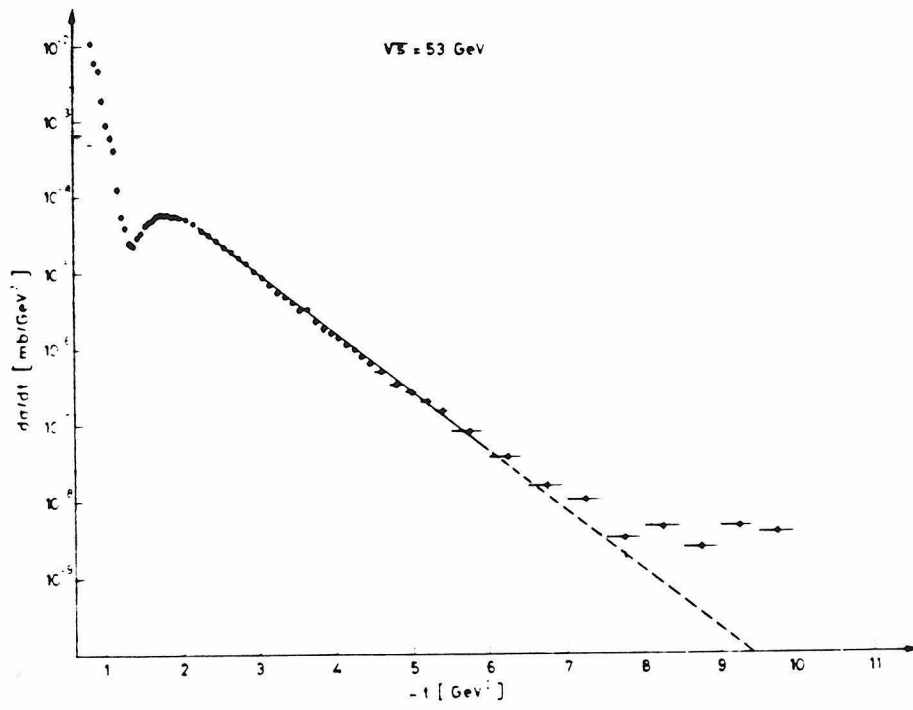


Fig. 3.21

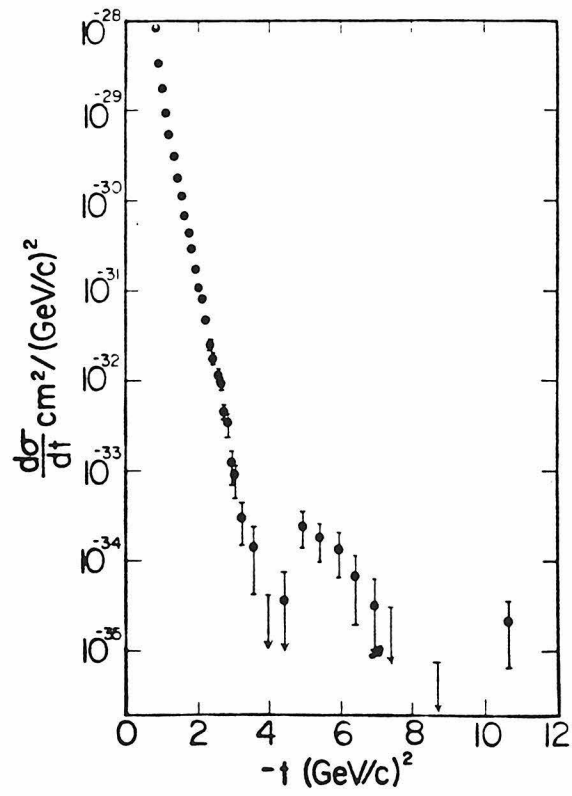


Fig. 3.22



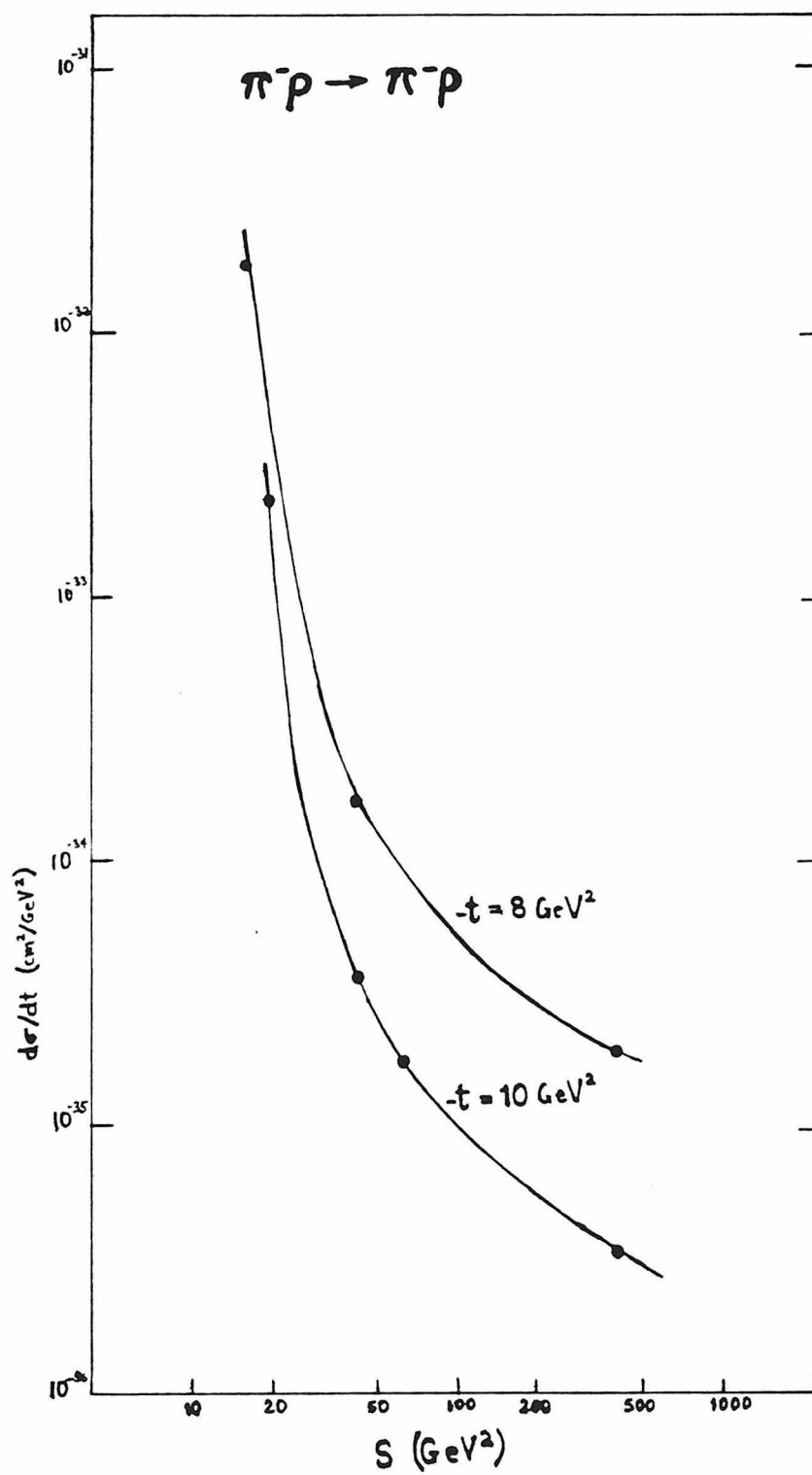


Fig. 3.23

## CHAPTER IV

### RESULTS OF THE $\pi\pi$ CALCULATION

We report in this chapter the results of a detailed QCD computation, to leading order in  $\alpha_s$ , of  $\pi\pi$  elastic scattering. An analytic approach to this problem is easily seen to be an extremely tedious and time consuming task, if not an impossible one. We have therefore developed, for this calculation, a numerical algorithm for computing tree diagrams in perturbative QCD. This algorithm was translated into a FORTRAN 77 program, and the computation was carried out on a VAX 11/780 computer. The details of the method of computation are presented in an appendix to the thesis, and in this chapter we shall concentrate on reporting and analyzing the results.

#### 4.1. SETTING THE STAGE

##### 4.1.1. MOTIVATION

Much as one would desire, the results of this calculation cannot be directly compared with experimental data, since data on high- $P_T$   $\pi\pi$  elastic scattering are non-existent (due to the obvious difficulty of making a pion target). The motivation for choosing to compute this process, instead of  $\pi p$  or  $pp$  scattering, stems from its relative simplicity. The elastic scattering of two mesons involves far fewer diagrams than meson-baryon or baryon-baryon scattering and each diagram itself is simpler with a fewer number of quarks and therefore fewer

degrees of freedom to integrate over. On the other hand, meson-meson scattering has all the essential theoretical complexity encountered in the modeling and computing of elastic hadron scattering involving baryons, and is therefore expected to exhibit all the important qualitative features that one might find in the more realistic processes. It is therefore of great theoretical as well as experimental interest to carry out a detailed QCD computation of the simplest hadron-hadron scattering process. Such a computation could prove to be a more detailed and quantitative test of the theory than the ones possible for inclusive processes, where quark fragmentation introduces many uncertainties in the calculation. Moreover, the method developed for this computation is completely general with respect to the number of quarks involved in the diagram, so that with the availability of more computer time and faster computers it should be easily possible to extend the calculation to the case of  $\pi p$  and  $pp$  in the future.

The results presented here are for the case of same charge  $\pi\pi$  scattering (i.e.  $\pi^+\pi^+$  or  $\pi^-\pi^-$ ). Other cases of  $\pi\pi$  scattering will involve more diagrams because of the possibility of quark annihilation, but the qualitative behavior for most purposes is expected to be the same. The restriction of same-charge also makes the process we calculate more akin to the case of  $pp$  scattering, which is the best measured elastic scattering reaction and therefore most suitable for comparison with theory.  $\pi^+\pi^+$  and  $\pi^-\pi^-$  scattering are expected to be identical to each other because of charge conjugation symmetry.

#### 4.1.2. THE $\pi\pi$ SCATTERING AMPLITUDE

Our calculation is based on the theoretical analysis of exclusive processes presented in detail in Chap. II. We rewrite here the expression for the elastic scattering amplitude derived in Chap. II (Eq. (2.22)), adopting the same conventions and notation that was used in that chapter,

$$\begin{aligned}
 M_{AB \rightarrow CD}(s, \theta_{\text{c.m.}}) = & \int_0^1 [dx_a][dx_b][dx_c][dx_d] \varphi_C^*(x_c, Q^2) \varphi_D^*(x_d, Q^2) \\
 & \times T_H(x_a, x_b, x_c, x_d, s, \theta_{\text{c.m.}}) \varphi_A(x_a, Q^2) \varphi_B(x_b, Q^2)
 \end{aligned} \tag{4.1}$$

where the scale  $Q^2$  is taken to be,

$$Q^2 = -t = \frac{s}{2}(1 - \cos \theta_{\text{c.m.}}).$$

For the case of  $\pi\pi$  scattering we need associate only one independent momentum fraction with each incoming or outgoing hadron. Thus, for example, we can let  $x_a$  be the momentum fraction of the quark in pion A, so that the momentum fraction of the anti-quark is given by  $(1-x_a)$ . Then the integral in Eq. (4.1) is a four dimensional integral and the region of integration is the four-dimensional unit cube. The hard scattering amplitude  $T_H$  can be expanded as a perturbation series in powers of  $\alpha_s(Q^2)$  and can thus be computed, to any given order, as a sum of Feynman diagrams. The distribution amplitudes satisfy well defined evolution equations which can be solved to determine  $\varphi(x, Q^2)$  in terms of a given initial condition  $\varphi(x, Q_0^2)$ . Let us examine these components of the amplitude in more detail in order to better appreciate the significance of the results of this calculation.

#### 4.1.3. THE PION DISTRIBUTION AMPLITUDE

The differential equation governing the  $Q^2$ -evolution of the pion distribution amplitude is derived in Sec. 2.2.4 and its solution is presented in Eqs. (2.12) and (2.13). Each experimental data point for an exclusive process represents the result of an integration over the momentum fractions associated with the

constituents of the reacting hadrons. The elastic scattering data at some fixed  $Q_0^2$  cannot therefore be used to determine the initial distribution amplitude  $\varphi(x, Q_0^2)$  and thus the amplitude,  $\varphi(x, Q^2)$ , for all higher  $Q^2$ . In fact we need data at a large (theoretically infinite) number of  $Q^2$ -values in order to determine the constants  $\varphi_n(Q_0^2)$  in Eq. (2.12) and thus the function  $\varphi(x, Q_0^2)$  using the expansion given in Eq. (2.10). It is then evident that in order to compute the elastic scattering cross-section *in an absolute sense*, so as to test our theoretical model, we must use the data for a different exclusive process but involving the same distribution amplitude, to determine the function  $\varphi(x, Q_0^2)$ . The elastic form factor of the hadron is a natural choice for such a process. Unfortunately, the data available for the pion form factor are very limited and have large errors. We therefore adopt a somewhat less ambitious strategy to solve the problem.

In the limit of very large  $Q^2$  the solution for  $\varphi(x, Q^2)$  has an asymptotic form which is completely determined (independent of the initial condition) up to a normalization constant (Eq. 2.14).

$$\varphi(x, Q^2) = c_\pi x(1-x) \quad (4.2)$$

Even though the  $Q^2$ -values of the available data on elastic scattering may not be large enough for this limit to be valid, the asymptotic form should serve as a very good approximation. The function  $x(1-x)$  vanishes at the end-points, is peaked at equal momenta of constituents and is smooth in between; which is what we expect of the distribution amplitude at any value of  $Q^2$ . The constant  $c_\pi$  could now be determined from the form factor data, but in fact a more accurate estimate is obtained by using the pion decay constant  $f_\pi$ . For the purposes of the current calculation, the distribution amplitude of Eq. (4.2) is certainly quite adequate, since we are interested in the qualitative features of the cross-section

and in obtaining reasonable estimates of the absolute normalization and angular dependence.

The full pion wave function involves color, flavor, spin and Dirac structure in addition to the space-time part discussed above. These parts of the wave function are well known and we express below the complete wave function for  $\pi^+$  in order to define the conventions adopted for the calculation.

$$\Psi(x, p_\pi) = c_\pi x(1-x) E_\pi \sum_{i=1}^3 [u_{\bar{i}} \bar{u}_i - u_i \bar{u}_{\bar{i}}] \quad (4.3)$$

where  $p_\pi$  is the four-momentum and  $E_\pi$  the energy of the pion. The sum is over the three color indices. The factor,  $\sqrt{x(1-x)}$ , coming from the normalization of the spinors, has been absorbed into the distribution amplitude. For the present calculation all quarks have been assumed massless, so that  $\bar{u}u = \bar{v}v = 0$  in our convention for spinors. With these assumptions the computation of  $c_\pi$  from the measured value of  $f_\pi$  yields the following result:

$$c_\pi = 0.065 \text{ Gev}$$

#### 4.1.4. THE HARD SUBPROCESS DIAGRAMS

As discussed in Chap. II, the leading order contribution to  $T_H$  consists of the sum of all connected tree diagrams where the scattering is assumed to take place between sets of collinear quarks representing each hadron. Even for the case of  $\pi\pi$  scattering, which involves four constituents, the quarks and anti-quarks can be connected to each other by gluon lines in a large number of ways, giving rise to a large set of tree diagrams. It is easy to see that an increase in the number of scattered constituents leads to very rapid increase in the number of diagrams. The diagrams for pp scattering have an estimated count of over a

million! Before launching on a diagram by diagram computation it is useful to organize these diagrams into specific classes. For same charge  $\pi\pi$  scattering the diagrams divide into two major classes: (a) - *diagrams which do not involve the interchange of any quark-constituents during the scattering process*, and (b) - *diagrams which do involve the interchange of the quarks or of the anti-quarks between the two interacting pions*. For the case of same charge scattering we do not have to worry about the possibility of quark anti-quark annihilation. We have already seen that these two classes of diagrams have a very different small angle behavior.

Each of the above classes can be further subdivided into two categories; diagrams which result in a pinch singularity in the integrated amplitude, and diagrams which do not. The *pinch diagrams* do not obey dimensional scaling because of the persistence of long distance effects and result in the so called multiple scattering mechanism. The *hard diagrams* are dominated by short distance interactions and are responsible for the hard scattering mechanism which we have seen leads to power-law scaling. The pinch diagrams can be visually separated from the hard ones because of their direct relationship with multiple scattering (Landshoff) diagrams. *If a  $\pi\pi$  connected diagram can be reduced to a multiple scattering diagram by the removal of a single gluon line, at least one of whose ends is connected to a quark line, then the diagram belongs to the pinch category.* Otherwise it is a hard diagram. As we have seen in Chap. II, a careful treatment of infra-red divergences in pinch diagrams forces us to include a Sudakov factor in the integrand, which then causes a partial suppression of the pinch region and, in addition, leads to the introduction of a length scale into the integrated amplitude. This length scale is essentially an infra-red cut-off corresponding to the hadronic radius ( $\sim 1/\Lambda$ ) beyond which the system is color neutral. The Sudakov factor is then a means by which some of the effects

of soft gluon interactions can be included in the scattering amplitude within the context of perturbation theory. The effect of these long range interactions on the behavior of the elastic cross-section is an important item to be investigated in the current calculation.

The task of computing the diagrams can be immensely shortened by making use of the symmetries that exist among various diagrams. For class-(a) diagrams (henceforth called *gluon exchange* diagrams) one can easily identify four symmetry transformations. These can be listed as: (1,2) the exchange of the quark with the anti-quark within either of the two pions, which can at most lead to a change in the sign of the diagram, (3) the exchange of the two pions with each other which is essentially a rotation of the diagram by  $180^\circ$  about a horizontal axis, (4) the exchange of the in-going pions with the out-going pions, which can be considered as a  $180^\circ$  rotation about a vertical axis or alternatively a time reversal transformation. These transformations should result in *sixteen* diagrams having the same magnitude for their amplitude. However, sometimes a symmetry transformation leads to the same diagram as before, so that sixteen only represents the maximum possible number in a symmetry group. For class-(b) diagrams (henceforth called *quark exchange* diagrams) the first two symmetries do not hold because the constituent which undergoes an interchange cannot be identified with any one pion. The rotations about the horizontal and vertical axis are still valid symmetries and can at most relate *four* different diagrams. Another useful fact to notice is that gluon exchange diagrams, which have a single gluon going across from one pion to another, have a vanishing color-factor, and need not be computed. This is not true for the quark exchange diagrams.

We are now in a position to catalog all the contributing diagrams and to label them with a numbering scheme for the sake of easy reference. Fig. 4.1



shows the three multiple scattering diagrams that are useful in separating the pinch diagrams from the hard ones. Every pinch diagram can be reduced to one of these three diagrams by removing one gluon line from it. It is the region where this extra gluon becomes soft or collinear that produces the pinch singularity in these diagrams. Fig. 4.2 presents the complete list of connected diagrams that contribute to same charge  $\pi\pi$  elastic scattering. The list is organized according to the classes that have been discussed above. We do not include diagrams that involve the interchange of the anti-quarks in the pions or those that involve the interchange of both constituents. The contribution of these diagrams is automatically taken into account when we symmetrize the elastic scattering amplitude with respect to the exchange of the two final state pions. For the sake of brevity, only one representative diagram is drawn for each symmetry group. The others can be obtained by carrying out the symmetry transformations on this one.

The labeling scheme for the diagrams is designed to help identify their class and sub-class. The first letter in the label is either  $G$ , for gluon exchange, or  $Q$  for quark exchange, while the second letter is either  $P$ , for pinch diagram, or  $H$  for hard diagram. The diagrams in each sub-class are numbered with two numbers such that all diagrams that differ only because of a different time-ordering of the gluon vertices have the same first number. A count of the diagrams reveals the following: there are 75 gluon exchange diagrams (48 pinch and 27 hard), and there are 100 quark exchange diagrams (24 pinch and 76 hard).

#### 4.1.5. SOME MORE REMARKS

A few more explanatory remarks are in order before we present the results of our calculation. The basic object of the present calculation is to compute the two functions  $f$  and  $g$  defined in Sec. 2.3.4. As expressed in Eq. (2.35), the amplitude for  $\pi\pi$  scattering, after integrating over all the momentum fractions, can be written as:

$$M_{\pi\pi}(s, \theta_{\text{c.m.}}) \sim \frac{c_\pi^4}{s^2} \left[ f(\theta_{\text{c.m.}}) + g(s/\Lambda^2, \theta_{\text{c.m.}}) \right] \quad (4.4)$$

We have extracted the four powers of  $c_\pi$  coming from the four distribution amplitudes in the matrix element, so that the functions inside the brackets are dimensionless.  $f$  contains the contribution of the hard diagrams and  $g$  the contribution of the pinch diagrams. To be exact,  $f$  too has some dependence on  $s$  because of the presence in it of the coupling constant,  $\alpha_s(Q^2)$ . However, this dependence is through a known logarithmic factor while the  $s$ -dependence in  $g$  can be more complex and serious. In the computation of each diagram, the momenta of the quarks are expressed in units of the center-of-mass energy. This implies that the result of a diagram computation is in fact proportional to  $s^2 \hat{M}_{\pi\pi}$ , where  $\hat{M}_{\pi\pi}$  is the matrix element corresponding to a single diagram. Thus summing this quantity for each class of diagrams will directly yield the desired functions.

Since some of the propagators, in both pinch as well as hard diagrams, can go on shell in the middle of the integration region, it is necessary to add a small imaginary part to these propagators ( $p^2 \rightarrow p^2 + i\Lambda^2$ ) in order to carry out the numerical integration. This displaces the pole from the real axis and makes the integrand finite in the whole region. In the case of pinch diagrams this modification of the propagator also serves to regulate the pinch singularity.

While the hard contribution is expected to become independent of  $\Lambda$ , as this mass scale is taken to zero, the unsuppressed pinch contribution depends on  $\Lambda$  in an important way.

We now have three mass scales involved in the diagram calculation, all of them of the order of the QCD scale,  $\Lambda$ . It is important to be able to tell them apart and we do so by appending a subscript to  $\Lambda$ , indicating which of the three scales it denotes.  $\Lambda_\alpha$  is the scale involved in the argument of the running coupling constant  $[\alpha_s(Q^2/\Lambda_\alpha^2)]$ . This is the scale that is often referred to as the QCD scale.  $\Lambda_p$  is the scale used in the regulation of the diagram propagators and, as was argued in Sec. 2.3.2., this too has a "natural" magnitude of the order of the QCD scale.  $\Lambda_s$  is the scale that appears in the QCD-improved Sudakov factor (Eq. (2.31)). The functions  $f$  and  $g$  can depend on these scales through the dimensionless ratios of these scales with the energy scale  $\sqrt{s}$ .

## 4.2. FIXED ANGLE ENERGY DEPENDENCE

In this section we investigate the fixed angle behavior of the quantity  $s^2 \hat{M}_{\pi\pi}$  for some typical diagrams. Let us refer to this function as  $h$ , so that there is an  $h$  associated with each diagram. To get the desired functions  $f$  and  $g$  we must sum  $h$  over a class of diagrams but, for the purposes of analyzing general behavior, it is far simpler to study this function for a representative diagram. As discussed above,  $h$  can, in general, depend on  $s/\Lambda_\alpha^2$ ,  $s/\Lambda_p^2$ ,  $s/\Lambda_s^2$  and of course  $\theta_{c.m.}$ . Since some of the diagram propagators have imaginary parts ( $i\Lambda_p^2$ ) in them,  $h$  is a complex function. We calculate both the real and imaginary parts of  $h$  and plot them as functions of different variables.

#### 4.2.1. THE HARD CONTRIBUTION

We first study the behavior of  $h$  for hard diagrams. We choose as our typical hard diagram, the one listed in the catalog as GH1.1. Let us look, first, at the behavior of  $h$  for the case where the coupling constant factor ( $\alpha_s^3$ ) has been excluded from the amplitude. In this case the fixed-angle  $h$  will depend only on  $s/\Lambda_p^2$ . As  $s/\Lambda_p^2$  increases  $h$  should attain a constant value. Fig. 4.3 shows the results for a  $90^\circ$  calculation of GH1.1 and the behavior of both the real and imaginary parts of  $h$  is exactly as expected. The plot of  $h$  against  $s/\Lambda_p^2$  can be viewed either as showing the dependence on  $s$  for a fixed  $\Lambda_p$ , or as depicting the dependence on  $\Lambda_p$  for a fixed  $s$ . If we assume that the addition of  $i\Lambda_p^2$  to the propagator represents a genuine modification of the amplitude (indicating the inability of on-shell colored quarks or gluons to travel long distances; i. e.  $1/\Lambda_p$  is a decay length) and if we further assume  $\Lambda_p$  to be fixed at 100 Mev then the energy independence of  $h$  is achieved around  $s \sim 5 \text{ Gev}^2$  ( $s/\Lambda_p^2 \sim 500$ ). Thus for large enough  $s$  we expect the cross-section corresponding to this diagram to obey power-law scaling with  $n=6$ .

The inclusion of the coupling constant factor ( $\alpha_s^3$ ) in the calculation causes a further dependence of  $h$  on  $s/\Lambda_\alpha^2$ . We can associate one coupling constant with each of the three gluons in the diagram. In the actual calculation, the argument of each coupling constant, at a given point in the integration space, is taken to be the off-shellness of its associated gluon at that integration point. This method should result in a more accurate treatment of coupling constant effects than that obtained by using the constant arguments,  $|t|$  or  $|t/4|$ .

The result of this calculation is plotted in Fig. 4.4. For simplicity we take  $\Lambda_p = \Lambda_\alpha$ , and we view the plot as a function of  $s$  for some fixed value of these mass scales. The effect of including the coupling constant factor is quite dramatic.

Both, real and imaginary parts now fall rapidly as a function of  $s/\Lambda_\alpha^2$ , though the slope is very gradually decreasing as expected. The imaginary part dominates the amplitude as it did for the previous calculation. The plot shows that even for  $s/\Lambda_\alpha^2 \sim 50,000$  the rate of fall is substantial. As we saw from our previous plot (Fig. 4.3), the effect of  $\Lambda_p$  lasts only up to  $s/\Lambda_p^2 \sim 500$ . Thus after this value for  $s/\Lambda_\alpha^2$  the behavior is completely controlled by the scale  $\Lambda_\alpha$ . In the region,  $1000 < s/\Lambda_\alpha^2 < 5000$ , the imaginary part of  $h$  can be very well described by a straight line with a slope of -0.71. If we take  $\Lambda_\alpha$  to be 100 Mev, then this range corresponds to  $10 < s < 50 \text{ Gev}^2$ , which is the entire range of presently existing wide-angle pp elastic data. This behavior of  $h$  leads to a large increase in the power of  $s$  that describes the fall-off, with energy, of the  $\pi\pi$  cross-section. In the above energy range the value of  $n$  resulting from the slope of the plotted line is 7.42 instead of the dimensional counting prediction of 6. In the case of pp elastic scattering, *the increase in  $n$  is expected to be even larger* because the cross-section has 10 powers of  $\alpha_s$  instead of 6. This is an important fact to be kept in mind while comparing elastic data with the predictions of the hard scattering model.

#### 4.2.2. THE PINCH CONTRIBUTION

Let us now look at the results of calculating  $h$  for a typical pinch diagram. Here we expect more interesting effects in the fixed angle behavior of  $h$ . We choose the diagram labeled GP1.1 and first present the results for the amplitude which contains neither a coupling constant factor nor a Sudakov factor. Then  $h$ , for fixed angle, is only a function of  $s/\Lambda_p^2$ . This function, for  $\theta_{c.m.} = 90^\circ$ , is plotted in Fig. 4.5, and we immediately see the effect of the pinch singularity in the consistently rising nature of both the real and imaginary parts of  $h$ . After a brief nonasymptotic region for small  $s$ , the curves attain a constant slope which can

be accurately calculated to be 0.5. Thus the function  $h$  is asymptotically proportional to  $\sqrt{s/\Lambda_p^2}$ . This is exactly the result obtained through analytical calculations of  $\pi\pi$  pinch diagrams, and causes the cross-section for such diagrams to fall like  $1/s^5$  instead of  $1/s^6$ . It is also interesting to note that the real and imaginary parts of  $h$  seem to become equal to each other asymptotically. This is not a significant result because the relative magnitude of the real and imaginary parts of  $h$ , depends completely on the relative magnitude of the real and imaginary parts of the constant added to the propagator for regulating the singularity. If this constant is real instead of imaginary, then, asymptotically, the pinch contribution comes out to be pure imaginary.

In our next calculation of the same diagram we include the Sudakov factor in the integrand, but still avoid the coupling constant factor in order to better see what the Sudakov modification does to the fixed angle behavior of the pinch diagram amplitude. The result for the  $90^\circ h$  is plotted in Fig. 4.6. as a function of  $s/\Lambda_s^2$ . The regulation of the propagators with the scale  $\Lambda_p$  is no longer necessary because the Sudakov factor automatically removes the singular regions of the integrand. In fact we have put  $\Lambda_p=0$  for the present calculation in order to see the uncontaminated effect of the Sudakov factor. Including  $\Lambda_p$  affects only the initial part of the curves. The plot shows that the imaginary part is falling rapidly and can be taken to be zero in the asymptotic region. The reason for this is that the imaginary contribution comes only from the pinch region of the integration space and this region is completely suppressed by the Sudakov factor. However, the real part, which gets its contribution from the whole of the integration space is only partially suppressed and, despite the Sudakov factor, it still shows up as a rising function of  $s/\Lambda_s^2$ . This function *does not* seem to attain any asymptotic slope even up to values of  $s/\Lambda_s^2$  as high as 500,000 (not shown on the plot of Fig. 4.6). The rate of change of the slope of the curve seems to be

decreasing with an increase of  $s/\Lambda_s^2$  and the curve is convex pointing upward. The function does not fit any simple analytical form, and it certainly does not agree with the approximate analytical calculation of Mueller. Even at the highest values of  $s/\Lambda_s^2$  in the plot, the slope has only achieved a value of 0.20, which is far from the asymptotic value of 0.08 predicted by Mueller (see Sec. 2.3.4). Our numerical calculation is certainly more accurate and trustworthy than the analytical one by Mueller and we strongly suspect the validity of his approximation method, for which he does not give any proof. This is then a completely new and very important result, obtained by a numerical integration, where analytical methods are too difficult. A good way to characterize the function plotted in Fig. 4.6 is to specify its slope at regular intervals. The results of this exercise are shown in the table below along with the value of  $n$  resulting from each slope.

$s/\Lambda_s^2$	slope	$n$
100	0.63	4.74
400	0.48	5.04
1600	0.35	5.30
6400	0.27	5.46
25600	0.20	5.60

We now add the coupling constant factor to the integrand and look at the final result of the QCD prediction for pinch diagrams. Fig. 4.7 shows the plot of the real part of  $h$  resulting from our calculation. The imaginary part has been left out since it remains insignificant compared to the real part and can be safely ignored. Again, as a simplest case, we have set  $\Lambda_p = \Lambda_\alpha = \Lambda_s$  and we view the plot as a function of  $s$  for some fixed value of these constants. The function  $h$

has a very interesting form. It begins to rise a little but soon the coupling constant effect overcomes the pinch effect resulting in a slowly falling function. This results in a low, broad hump and a remarkably flat function over a wide range of  $s/\Lambda_\alpha^2$ . The shape of this curve is controlled by the interplay between the Sudakov modified pinch effect and the coupling constant effect. Changing  $\Lambda_p$  only slightly shifts the location of the peak of the hump but otherwise the shape of the curve remains the same. The opposing scale breaking effects of the pinch singularity and the running coupling constant seem to nullify each other and the resulting amplitude closely approximates the dimensional scaling behavior. For a better comparison with elastic scattering data we shall again characterize this curve by specifying the slope at regular intervals of  $\ln(s/\Lambda_\alpha^2)$ . This is displayed in the table below and we again show the value of  $n$  resulting from the slope. Note that dimensional scaling predicts  $n=6$ .

$s/\Lambda_\alpha^2$	slope	$n$
100	0.21	5.58
200	0.04	5.92
400	-0.16	6.32
800	-0.23	6.46
1600	-0.25	6.50
3200	-0.22	6.44
6400	-0.20	6.40

What is interesting to notice from the above table is that the value of  $n$  is never far removed from the scaling prediction. In fact, if we take  $\pm 0.5$  as a grace margin around the scaling value of  $n$  (this is often the experimental accuracy



within which  $n$  can be determined from data), then the calculated amplitude is consistent with  $n=6$  in the whole of the range for which it has been plotted. The slope of the curve is exactly zero (corresponding to  $n=6$ ) at about  $s/\Lambda_\alpha^2 \sim 250$ . If we assume that all the mass scales have the value 100 Mev then this position corresponds to  $2.5 \text{ Gev}^2$ , and if we use the value 200 Mev then this privileged point is at  $10 \text{ Gev}^2$ . Changing the relative magnitude of the scales also results in a shift of the peak, but it is important to emphasize that the general character of the function is fairly insensitive to the relative magnitude of the mass scales, as long as they are reasonably close to each other. The dependence of the function  $h$  on the center-of-mass angle will be discussed later, but choosing another wide angle instead of  $90^\circ$  would have led us to the same conclusions about energy dependence.

It is important, also, to establish that the behavior of  $h$  discussed for the above two diagrams is not peculiar to those diagrams. We have made similar calculations for several other diagrams in each class and the results lend strong support to the claim of generality for the behavior observed in the two selected diagrams. The details do differ slightly from diagram to diagram, e.g. the energy at which a hard diagram becomes independent of  $\Lambda_p$  can vary a little, and for the pinch diagrams the slope of the Sudakov modified  $h$ -function at a given value of  $s/\Lambda_s^2$  can change by as much as 0.05 (slope for diagram GP2.1 at  $s/\Lambda_s^2=25600$  is 0.25); but our general conclusions about the energy dependence at wide angles remain unchanged. Our calculations also show that *the fixed angle behavior of  $h$  is independent of whether the diagram involves gluon exchange or quark exchange*. Thus, one need pay heed to only the pinch/hard distinction while analyzing the fixed angle energy dependence of the elastic cross-section.

### 4.3. THE NORMALIZATION FOR 90° SCATTERING

#### 4.3.1. RELATIVE NORMALIZATION

Before we leave this topic it is of great interest to compare the relative normalization of the two contributions whose behavior we have analyzed. Whichever contribution dominates the total amplitude will be the one that determines the actual behavior of the elastic cross-section for  $\pi\pi$  scattering. From our analysis of fixed angle energy dependence it is clear that for large enough  $s$  the pinch contribution will dominate the cross-section since the hard contribution is falling much more rapidly with  $s$  than is the pinch contribution (compare Figs. 4.4 and 4.7). However, we would like to investigate the relative magnitude of the two contributions at energies where most of the wide angle elastic data have been collected. There is an inherent uncertainty that must be faced in this attempt because our calculation provides the amplitude as a function of  $s/\Lambda^2$ , and the exact value of the various hadronic mass scales is not known. Even so, we can derive significant conclusions from such an analysis, and if the same calculations as above are done for a measured elastic process then the results can be used to make an estimate of the magnitude of  $\Lambda$ . In the following analysis we assume all the mass scales to be equal in magnitude and we denote them by  $\Lambda$ .

To simplify our analysis, let us choose a single value of  $s/\Lambda^2$  at which to make comparisons of the calculated amplitudes. We choose this to be given by  $s/\Lambda^2=2000$ . If  $\Lambda=100$  Mev then this point corresponds to  $s = 20 \text{ Gev}^2$  which is close to where most of the wide angle data exist. For  $\Lambda=200$  Mev the same point corresponds to  $s = 80 \text{ Gev}^2$ , and so on. Let us first consider the effects of the coupling constant factor and the Sudakov factor on the normalization at this point. In the case of the hard diagram we only have the coupling constant to

worry about. Adding the coupling constant to the calculation reduces the imaginary part of the amplitude by a factor of about 25. The real part is not known with enough accuracy at this energy, but it is sub-dominant anyway. In the case of pinch diagrams, both the Sudakov factor and the coupling constant factor affect the normalization obtained from the "bare" diagram calculation. At the value of  $s/\Lambda^2$  being considered, the Sudakov factor reduces the amplitude by a factor of about 30 and the coupling constant does the same by another factor of 30.

Let us now compare the normalization of the pinch and hard diagrams with each other. In the units that we use to express the function  $h$  obtained from our calculation, the magnitude of the hard diagram at  $s/\Lambda^2=2000$  is 0.065, and the magnitude of the pinch diagram with all factors included is 0.012. These two numbers are quite comparable and urge us to go further and do a more complete calculation of the full hard amplitude and the full pinch amplitude. It turns out that the magnitude of  $h$  changes by up to an order of magnitude from one diagram to another in the same class. It is therefore not very useful to calculate one diagram and to multiply its contribution by the number in that class. One must do a detailed calculation of all the contributing diagrams. This way we can also obtain the QCD prediction for the absolute normalization of the  $90^\circ \pi\pi$  elastic cross-section, which was one of the aims with which we set out on this project. Even though the  $\pi\pi$  cross-section at large  $P_T$  has not been measured, one can still hope to do some phenomenology by using the data for  $\pi p$  and  $pp$  cross-sections. This detailed calculation will also allow us to compare the magnitude of the gluon exchange and quark exchange contributions, which is very relevant to the analysis of small angle behavior.

The results for the  $90^\circ$  calculation of  $h$  at  $s/\Lambda^2=2000$  are presented in the following tables. We calculate each representative diagram of a symmetry group

(listed in Fig. 4.2) and then multiply the result by the number in that group to get the answer, which goes as an entry in our table against the identification label of that symmetry group. The number of diagrams ( $N_{sym}$ ), in the symmetry group is also listed in the tables. The contribution from each of the four classes into which the diagrams have been divided is summed separately.

#### A. GLUON EXCHANGE PINCH DIAGRAMS

DIAGRAM	$N_{sym}$	$h(s/\Lambda^2=2000)$	
		REAL	IMAGINARY
GP1.1	8	0.10	0.0
GP1.2	8	0.08	0.0
GP2.1	8	-0.93	0.0
GP2.2	8	-0.81	0.0
GP3.1	16	0.05	0.0
TOTAL	48	-1.51	0.0

B. GLUON EXCHANGE HARD DIAGRAMS

DIAGRAM	$N_{sym}$	$h(s/\Lambda^2=2000)$	
		REAL	IMAGINARY
GH1.1	16	0.05	1.04
GH1.2	8	0.0	-0.01
GH2.1	2	-0.51	0.72
GH3.1	1	0.11	0.0
TOTAL	27	-0.35	1.73

C. QUARK EXCHANGE PINCH DIAGRAMS

DIAGRAM	$N_{sym}$	$h(s/\Lambda^2=2000)$	
		REAL	IMAGINARY
QP1.1	4	0.022	0.0
QP1.2	4	0.019	0.0
QP1.3	4	0.017	0.0
QP1.4	4	-0.238	0.0
QP2.1	2	-0.004	0.0
QP2.2	2	-0.003	0.0
QP3.1	2	-0.004	0.0
QP3.2	2	-0.003	0.0
TOTAL	24	-0.194	0.0

D. QUARK EXCHANGE HARD DIAGRAMS

DIAGRAM	$N_{sym}$	$h(s/\Lambda^2=2000)$	
		REAL	IMAGINARY
QH1.1	2	0.030	0.0
QH1.2	4	0.007	0.014
QH1.3	2	-0.003	0.002
QH2.1	2	0.030	0.0
QH2.2	4	0.007	0.014
QH2.3	2	-0.003	0.002
QH3.1	4	-0.042	0.0
QH3.2	4	0.033	-0.004
QH3.3	4	0.040	0.0
QH3.4	4	0.001	-0.002
QH4.1	2	0.030	0.0
QH4.2	2	0.0	0.023
QH4.3	2	0.0	0.023
QH4.4	2	-0.001	-0.002
QH4.5	2	-0.001	-0.002
QH4.6	2	-0.026	0.042

... cont.

DIAGRAM	$N_{sym}$	$h(s/\Lambda^2=2000)$	
		REAL	IMAGINARY
QH5.1	2	0.030	0.0
QH5.2	4	0.0	0.046
QH5.3	4	-0.002	-0.004
QH5.4	2	-0.026	0.042
QH6.1	4	0.034	0.0
QH6.2	4	0.004	0.053
QH7.1	4	0.034	0.0
QH7.2	4	0.004	0.053
QH8.1	1	-0.003	-0.006
QH9.1	2	-0.019	-0.002
QH10.1	1	0.007	0.0
TOTAL	76	0.127	0.155

The numbers listed in these tables are calculated to within an accuracy of 10%. The accuracy can be increased indefinitely by using more points in the numerical integration, which in turn requires more computer time. However, for our purposes this accuracy is quite sufficient. Notice that many quark exchange diagrams have identical answers even though they are in different symmetry groups. This fact can be shown to be a consequence of an accidental symmetry



which is present for  $\theta_{c.m.}=90^\circ$ , but which does not hold at other angles.

Let us first compare the relative normalizations of the four different contributions. The CIM model, which for a long time has been used as a framework in which to view the detailed behavior of elastic scattering, is built on the shaky assumption that diagrams which involve the exchange of gluons between different hadrons are suppressed with respect to the ones which involve the exchange of quarks. Our calculation strongly questions the validity of this unproved assumption. Adding the pinch and hard contributions, the absolute magnitude of the gluon exchange amplitude comes out to be 2.54 while that of the quark exchange contribution works out to be 0.17. Thus, if anything, it is the gluon exchange mechanism that dominates the elastic cross-section for  $\pi\pi$  scattering. In fact, only one symmetry group (QH3.1), consisting of four diagrams out of a total of a hundred quark exchange diagrams, contributes to the CIM mechanism and, as can be seen, *there is nothing special about the value of this contribution*. On the average, the intrinsic normalization of a quark exchange diagram is of the same order of magnitude as that of a gluon exchange diagram, and since the energy behavior does not depend on the exchange-type of the diagram, this relationship is independent of  $s$ . Moreover, there is no reason to expect a very different conclusion for the results of a  $\pi p$  or  $pp$  calculation. In fact it seems that the relatively lower level of symmetry in the quark exchange diagrams may cause them to suffer more cancellation amongst each other, and thereby result in a smaller total magnitude than the one for the gluon exchange diagrams. Thus, inasmuch as our calculation is based on a fairly rigorous treatment of perturbative QCD, *this theory does not provide any evidence for the CIM model assumptions*, and if one is to continue working in the QCD framework, other explanations must be found for the successes of the CIM. Some recent QCD calculations [21] for inclusive processes have also shown a

lack of support for the CIM.

The other long held belief brought to a severe question by our calculation is the suppression of the multiple scattering mechanism with respect to the hard scattering one. The fact that the experimental rate of fall of the elastic cross-sections, with energy, is very close to the dimensional counting prediction has led many people to conclude that hard scattering is the dominating mechanism for elastic processes at large  $P_T$ . The Sudakov factor that builds up in the amplitude for the scattering of nearly on shell quarks is the most frequently quoted justification for the suppression of the pinch diagrams. Our calculation shows that, with a more careful treatment of Sudakov effects, the suppression is only partial and the magnitude of the pinch contribution at the energy of existing elastic data is of the same order of magnitude as the hard contribution. For both the gluon exchange and the quark exchange diagrams, the pinch and hard contributions at  $s/\Lambda^2=2000$  and  $\theta_{c.m.}=90^\circ$  work out to be almost equal. This means that for a somewhat higher value of  $s/\Lambda^2$ , say 10,000, the pinch contribution clearly dominates over the hard one. *It thus seems that a detailed analysis of elastic scattering in QCD does not provide any justification for ignoring the multiple scattering mechanism in the analysis of elastic data.*

It would be extremely interesting to compare the two contributions for  $\pi\pi$  and  $pp$  scattering. In the absence of such a calculation we can only make a few comments. First, contrary to a statement by Brodsky and Lepage, rough estimation shows the number of pinch and hard diagrams to be comparable for all elastic scattering processes. (The table at the end of this section presents a summary of the number of diagrams in each of the four classes for the three processes:  $\pi\pi$ ,  $\pi p$  and  $pp$ . The numbers for  $\pi p$  and  $pp$  are only rough estimates.) Secondly, since the general form of the Sudakov factor is the same for all such processes, there is no reason to expect a qualitatively different behavior of the

Sudakov modified pinch contribution for processes with more quarks. Furthermore, the pinch singularity in  $pp$  scattering is even more severe than that in the case of  $\pi\pi$  scattering. In some of the  $pp$  pinch diagrams, *two* gluons can become soft or collinear in the middle of the integration region at the same time. The  $h$ -function for such diagrams can be shown to be asymptotically proportional to  $s/\Lambda^2$  instead of  $\sqrt{s}/\Lambda^2$ , as was the case with  $\pi\pi$ . The Sudakov modified  $h$ -function corresponding to these diagrams can then be expected to rise with  $s$  even faster than was the case with  $\pi\pi$ , and therefore the energy at which the pinch contribution begins to dominate over the hard one will be even smaller. Thus, it is not at all unreasonable to conclude from our calculations that  *$pp$  elastic scattering at intermediate energies may be completely dominated by pinch effects rather than short distance ones.*

PROCESS	$N_{GP}$	$N_{GH}$	$N_{QP}$	$N_{QH}$
$\pi\pi$	48	27	24	76
$\pi p$	$\sim 1000$	$\sim 1500$	$\sim 1500$	$\sim 7500$
$pp$	$\sim 30,000$	$\sim 40,000$	$\sim 50,000$	$\sim 350,000$

#### 4.3.2. ABSOLUTE NORMALIZATION

From the results presented in the tables we can also work out the absolute normalization of the  $90^\circ$   $\pi\pi$  cross-section. Adding all the four contributions, the value of  $h$  at  $s/\Lambda^2=2000$  comes out to be  $-1.79+i1.89$ . After multiplying  $|h|^2$  by appropriate factors, including the four powers of  $c_\pi$  whose value was determined from the pion decay constant, the  $90^\circ$  result for the  $\pi\pi$  cross-section at  $s=20 \text{ GeV}^2$  and  $s/\Lambda^2=2000$  works out to be  $6.75 \times 10^{-35} \text{ cm}^2/\text{GeV}^2$ . For the sake of

a rough comparison, we quote here the experimental value of the  $\pi p$  and  $pp$   $90^\circ$  cross-sections at the same energy ( $s=20 \text{ Gev}^2$ ). The value for  $\pi p$  is  $2.6 \times 10^{-33} \text{ cm}^2/\text{Gev}^2$  and that for  $pp$  is  $7.2 \times 10^{-32} \text{ cm}^2/\text{Gev}^2$ . However, the comparison of these numbers is not very meaningful because the different cross-sections fall with energy at quite different rates, and their ratios will change with a change in the energy at which they are computed or measured. It may therefore be more sensible to compare the results for  $s^n(d\sigma/dt)$  where  $n$  is the power describing the fall-off of the relevant cross-section. These numbers are independent of energy but they all have different dimensions since the value of  $n$  is different for each cross-section, and therefore the comparison will now depend on the units of energy being used. If we further divide these numbers by the dimensional normalization constants of the distribution amplitudes present in the QCD expressions for the corresponding cross-sections, then we will have a dimensionless number for each of the cross-sections, enabling a more meaningful comparison.

Another small improvement is made if, instead of the normalization constants  $c_\pi$  and  $c_p$ , we use the value of  $tF_\pi(t)$  and  $t^2G_M(t)$  to divide the cross-sections. By this means some of the uninteresting constants present in the cross-sections will also be divided out, giving more relevant numbers for our comparison. As was discussed in the theoretical review, the expressions  $tF_\pi(t)$  and  $t^2G_M(t)$  are asymptotically independent of  $t$ , and are proportional to the square of the normalization constant of the distribution amplitude involved. Let us denote these constants by  $C_\pi$  and  $C_p$  for pion and proton respectively. Then the value of  $C_\pi$ , determined from the theoretical expression for  $F_\pi$ , involving the pion decay constant, is about  $0.10 \text{ Gev}^2$  and the value of  $C_p$  determined from the experimental data on the proton magnetic form factor works out to be about  $0.35 \text{ Gev}^4$ . Underneath we present the results of this analysis for the three

cross-sections, using the theoretically calculated value for  $\pi\pi$  and the experimentally determined ones for  $\pi p$  and  $pp$ .

$$\frac{s^6}{C_\pi^4} \frac{d\sigma}{dt}_{\pi\pi} = 1.11 \times 10^5 \simeq [3.33 \times 10^2]^2$$

$$\frac{s^8}{C_\pi^2 C_p^2} \frac{d\sigma}{dt}_{\pi p} = 1.40 \times 10^8 \simeq [1.18 \times 10^4]^2$$

$$\frac{s^{10}}{C_p^4} \frac{d\sigma}{dt}_{pp} = 1.26 \times 10^{11} \simeq [3.55 \times 10^5]^2$$

The values in the square brackets are the square roots of the numbers obtained for each cross-section. These square root values reflect the magnitude of the scattering amplitude instead of the cross-section, and are easier to interpret.

The next obvious question is that what significance, if any, can we associate with the magnitude of these dimensionless numbers? These numbers are proportional to the sum over all diagrams of the multi-dimensional integral, over quark momentum fractions, associated with each diagram (with the appropriate powers of  $s$  and of  $c_\pi$  and  $c_p$  extracted out of the integral). The magnitude of this number for a given scattering reaction therefore depends on two parameters, the average value of this integral for that scattering process and the number of diagrams that contribute to that process. Brodsky and Lepage in their review claim that using the square of the form factor as a divisor gets rid of the dependence on the intrinsic normalization of the diagrams, so that these numbers directly reflect the diagram count for each process. The soundness of this claim is very questionable and a careful analysis calls for a more prudent attitude. Firstly, the form factor only involves hard diagrams and does not have any equivalence of the pinch singularity. Secondly, the diagram obtained from squaring a form factor diagram (and replacing the photon by a gluon) has only

one gluon going across between the two diagrams and this diagram is already known to have a vanishing contribution. Our calculation has shown that even within the same class the contribution of two diagrams can differ by an order of magnitude. Thus it is hardly reasonable to treat the form factor as providing the typical magnitude of an elastic scattering diagram.

Another source of uncertainty in estimating the numbers of diagrams by such methods comes from the wide variation in the phase of the amplitude corresponding to a diagram. If we assume complete randomness in the phase then the above numbers are proportional to  $\sqrt{N}$  instead of  $N$ , where  $N$  represents the number of diagram and we assume their contributions to be roughly equal in magnitude. The number in a single class of  $\pi\pi$  diagrams is too small to ascertain if the cancellation is close to what we expect from a random distribution. However, a check with the contributions of the 16 or so unequal symmetry groups of quark exchange hard diagrams shows that the result is close to what is expected from a random distribution. Even if we accept this as generally true, the fact that there are always some diagrams constrained to be equal because of symmetry requirements, will make the total contribution proportional to something in between  $N$  and  $\sqrt{N}$ .

Despite all these uncertainties we give below a comparison of the dimensionless numbers calculated above, with an estimate of the  $N$  and  $\sqrt{N}$  of the gluon exchange hard diagrams that contribute to each process. The numbers in other diagram-classes can also be used, but we choose this class because if the form factor provides an estimate of any diagram contribution at all it has to be the gluon exchange hard diagram contribution.

ELASTIC REACTION	DIMENSIONLESS NUMBER	$N_{GH}$	$\sqrt{N_{GH}}$
$\pi\pi$	$\sim 330$	27	$\sim 5$
$\pi p$	$\sim 1200$	$\sim 1500$	$\sim 40$
$pp$	$\sim 350,000$	$\sim 40,000$	$\sim 200$

It should be kept in mind that the absolute value of our characteristic numbers is not very meaningful and we are only interested in the ratios. The table shows that these numbers are very close to being proportional to  $N_{GH}$ . Given the various uncertainties involved in this analysis we do not attempt to draw any conclusions from this result. If, as we have shown possible, the  $90^\circ$  cross-section is dominated by the pinch contribution then the ratios of these dimensionless numbers will depend very much on the Sudakov modified  $h$ -function that results from the integral in each of the three processes, in addition to the number of pinch diagrams involved in that process. For the moment, we conclude this analysis with the statement that there is nothing horribly inconsistent about the absolute normalization of our calculation when it is compared to the experimental measurements of  $\pi p$  and  $pp$  scattering. Later we will compare this analysis to a similar one for the small angle normalization of the  $\pi\pi$  cross-section.

#### 4.4. ANGULAR DEPENDENCE AT WIDE ANGLES

Having studied the fixed angle energy dependence and the  $90^\circ$  normalization of the  $\pi\pi$  cross-section, we now turn to its angular dependence. We will first look at the angular dependence in the wide angle regime and then study the small angle behavior to look for the fixed- $t$   $s$  dependence of the different contributions. It is again interesting to separately consider the contributions from pinch and hard diagrams and to compare them. For experimental data we must still look to  $\pi p$  and  $pp$  and see if we can make some general comparisons. As before, we begin by analyzing the results from a single representative diagram in each class, and we choose the same two diagrams that were studied in the previous section. All the mass scales are again taken to be equal to each other.

The results for the diagram GP1.1 are shown in Fig. 4.8. We plot the square of the magnitude of  $h$  as a function of  $\cos(\theta_{c.m.})$ , for the fixed energy corresponding to  $s/\Lambda^2=2000$ . The square of  $h$  is used so as to look at the angular dependence of the cross-section, which is a more relevant quantity, experimentally. Only the region  $\theta_{c.m.} \leq 90^\circ$  is shown in the plot since the function is symmetric around the  $90^\circ$  angle. A similar plot is shown for diagram GH1.1 in Fig. 4.9. It is very clear that the angular function for the pinch diagram rises more slowly with decreasing angle than the one for the hard diagram. This means that since the magnitude of the two contributions at  $90^\circ$  and at the chosen energy was comparable, at smaller angles the hard contribution will somewhat dominate the pinch one. But this domination can again be inverted by going to somewhat higher energies and if for  $\pi p$  and  $pp$  the domination of the pinch is much stronger, then the change in angle will not effect the situation very much. It is also interesting to note that the measured angular dependence of  $\pi p$  and  $pp$  scattering looks much more like the pinch diagram result rather than the hard



result. This is perhaps another piece of evidence that suggests the dominance of the pinch contribution at wide angles. A calculation of the complete angular dependence for the  $\pi p$  and  $pp$  cross-sections would be very useful in settling this issue. None of the previous calculations of these angular functions, in simplified models like the CIM, give very satisfactory fits to the data, despite the fact that they often have several adjustable parameters.

The next interesting aspect to look at is to see if the angular dependence changes with a change in the center-of-mass energy. The energy independence of the angular dependence is a hallmark of power-law scaling and we have already seen in Chap. III that there is strong evidence that experimental data on elastic scattering *does not* satisfy this requirement. The hard diagram contribution (as measured by the function  $h$ ), without considering coupling constant effects, acquires a constant value independent of energy *at all angles*. This fact immediately implies energy independence for the angular dependence of the hard contribution, as had been predicted by the QCD analysis of the hard scattering mechanism. Including the coupling constant factor in the calculation, does not significantly affect this conclusion since the magnitude of this additional factor, at a given energy, changes very little with angle (specially so in the wide angle regime).

The function  $h$  for the pinch contribution, however, involves a dependence on  $s/\Lambda^2$  even without considering the coupling constant factor. There is therefore no reason to expect the pinch contribution to have an energy independent angular dependence, unless the  $\theta_{c.m.}$  and  $s/\Lambda^2$  dependences of the function factorize. Instead of plotting the angular dependence of  $h$  at various energies we study this problem here by looking at the energy plots of  $h$  for various angles. This method is closer to the analysis of experimental data on elastic scattering, discussed in Chap. III. We leave out the coupling constant factor so as to

concentrate on the behavior of the Sudakov modified pinch amplitude, and because we have already seen that the effect of the coupling constant on factorization is unnoticeable. We have plotted the function  $h$  against  $s/\Lambda^2$  for several different wide angles in Fig. 4.10. The diagram being used is again GP1.1. Even to the eye it is fairly clear that the lines for different angles are not quite parallel to each other, so that the factorization of the angular and energy dependences *does not* hold. To quantify the deviation from factorization we compare the slopes of the curves at three different energies and present the results of this exercise in the following table.

$\theta_{\text{c.m.}}$	slope of $h$		
	$s/\Lambda^2=100$	$s/\Lambda^2=500$	$s/\Lambda^2=2000$
60°	0.77	0.45	0.40
70°	0.73	0.42	0.36
80°	0.70	0.40	0.34
90°	0.65	0.38	0.30

Even though these slopes have been calculated by using hand drawn tangents, and lack great accuracy, the numbers in the table exhibit a very clear pattern. The slope is the smallest for the 90° curve for all three energies and it tends to increase consistently with a decrease in the scattering angle. Because of the symmetry around 90°, we expect this pattern to be reflected identically for angles greater than 90°. These changes in slope will eventually lead to a dependence of  $n$  on angle for the pinch contribution to the elastic  $\pi\pi$  cross-section. For the energy range being considered, the change in  $n$  in going from

$90^\circ$  to  $60^\circ$  is about 0.2. This change is somewhat smaller than the kind of effects that have been seen in  $\pi p$ ,  $pp$  and  $np$  elastic data (Sec. 3.1-D). However the pattern of change is exactly of the kind that has been observed in these data and it is certainly possible that a similar calculation carried out for  $\pi p$  or  $pp$  would yield a larger change in  $n$  with angle. In any case this result of ours is again rather suggestive of the possibility that *some of the features of wide angle elastic data are better explained by assuming the dominance of pinch diagrams rather than the dominance of the hard ones.*

#### 4.5. SMALL ANGLE BEHAVIOR

It is of great interest to see if the small angle behavior of the various contributions to the  $\pi\pi$  cross-section can throw any light on the rather unexpected small angle behavior of  $\pi p$  and  $pp$  cross-sections discussed in the previous chapter. It was observed there, that one had to go to extremely high energies before the elastic cross-section data at moderate values of  $t$  began to show energy independent behavior. Since we already know from studying the Regge limit of scattering amplitudes in perturbation theory that diagrams involving the exchange of fermions lead to an asymptotically falling cross-section (going as  $1/s^2$ ), and those involving the exchange of vector bosons lead to an asymptotically energy independent cross-section, then the natural explanation of this phenomenon is to assume that quark-exchange diagrams *strongly* dominate over the gluon-exchange ones at wide angles (where  $s \approx t$ ). It has been claimed that this experimental observation provides a further reason for believing in the CIM picture of hadronic scattering. However, the results of our  $\pi\pi$  calculation at  $90^\circ$  make it highly unlikely that quark-exchange will be a strongly dominating mechanism in any elastic scattering reaction. If, therefore, we are to continue

to maintain our faith in the QCD analysis of exclusive processes, it behooves us to look for an alternative explanation of this phenomenon.

We analyze the small angle behavior of the four classes of diagrams by working out the  $s$ -dependence of the function  $h$  at fixed  $t$ , and as  $s \rightarrow \infty$ . Since we already know the energy dependence of  $h$  at fixed angles (i. e. fixed  $t/s$ ), this analysis enables us to deduce the asymptotic form of the amplitude in terms of powers of  $s$  and  $t$ . Having determined the functional forms of the different contributions to the scattering amplitude, we can use our calculation to deduce the relatively as well as absolutely normalized coefficients that multiply these forms. These coefficients are the best suited numbers for making rough comparisons with the small angle data on  $\pi p$  and  $pp$  scattering, and for speculating on the various possibilities for how these results can be extrapolated to other elastic reactions.

The method we use to carry out this analysis is to plot the expression  $(t/s)^n h$  as a function of  $s/\Lambda^2$  for a fixed value of  $-t/\Lambda^2$ , where  $n$  can be any integer. For each diagram we try out various values of  $n$  until we find one that makes the expression  $(t/s)^n h$  approach a constant value as  $s/\Lambda^2$  is being increased. This value of  $n$  then determines the asymptotic  $s$  dependence of the function  $h$ , and thereby of the amplitude  $\hat{M}_{\pi\pi}$ , corresponding to a particular diagram; and the constant value attained is the coefficient that multiplies the form that has thus been ascertained. Adding these coefficients for all diagrams possessing the same asymptotic form will then give us the desired coefficient for the contribution to the scattering amplitude corresponding to this class of diagrams. In an attempt to stay close to the energy regime of the existing elastic scattering data, as was the aim in our previous analyses, we choose  $-t/\Lambda^2 = 1000$  as the fixed value at which to carry out this analysis. For  $\Lambda = 100$  Mev this corresponds to a  $t$ -value of  $10 \text{ Gev}^2$ , which is in the midst of the region where

small angle data has been examined for evidence of hard scattering effects. Since the argument of the running coupling constant is essentially proportional to  $t$ , its presence in the amplitude does not significantly effect our analysis of the fixed- $t$   $s$ -dependence of  $h$ . The coupling constant factor, however, does introduce a  $t$ -dependence into the coefficients obtained from the analysis.

Figures 4.11 through 4.14 show some examples from the diagram by diagram determination of the functional forms and of the coefficients that go with them. We have chosen a representative diagram from each class. For the gluon exchange diagrams we again choose GH1.1 and GP1.1, which by now should be quite familiar to the reader. In Fig. 4.11 we plot the results for the real and imaginary parts of GH1.1. We see that the plot of  $(t/s)^3 h$  against  $s/\Lambda^2$  gives an asymptotically constant result. This implies that  $h$  goes as  $s^3$  and therefore  $\hat{M}_{\pi\pi}$  for this diagram goes as  $s$ , which in turn leads to an energy independent cross-section. This result is exactly what we were led to expect from our theoretical analysis in Sec. 2.3.5. The asymptotic amplitude for this diagram can now be written as a coefficient times the form  $s/t^3$ . Since the hard diagrams obey dimensional scaling, we expect this coefficient to be independent of the actual value of  $t$  used for carrying out the analysis. In actual fact, the coefficient drops with  $t$  fairly rapidly, because of the coupling constant factor. This can be seen clearly from the plot in Fig. 4.4 discussed in Sec 4.3.2.

In Fig. 4.12 the results for the diagram GP1.1 are plotted. *Here, we are in for a surprise.* Because of the presence of the Sudakov factor in the integrand, the analysis of Feynman diagrams in the Regge limit does not apply for the Sudakov modified pinch contribution. It turns out that, for this diagram, one has to plot the expression  $(t/s)^2 h$  in order to get something that approaches a constant value with increasing  $s$ . Thus, even though this is a gluon exchange diagram, its contribution does not yield an energy independent cross-section in

the asymptotic limit. The amplitude  $\hat{M}_{\pi\pi}$  becomes constant with  $s$  and the cross-section falls like  $1/s^2$ . Fig. 4.12 only shows the real part of the amplitude as the imaginary part is negligible. The second set of points in the figure represents the result of the unmodified pinch contribution corresponding to the same diagram; which we have included for the sake of making a comparison. The line drawn through these points has slope +1, so that the corresponding amplitude rises as  $s$  and again leads to an energy independent cross-section. Thus, both the hard as well as the pinch gluon-exchange diagrams yield cross-sections that are asymptotically independent of energy, but adding a Sudakov factor to the pinch diagram changes the  $s$ -dependence of its contribution in an important way. The coefficient obtained for the Sudakov modified pinch contribution must now multiply the form  $1/t^2$ . Without the presence of the coupling constant factor, this coefficient will rise slowly with an increase in the  $-t/\Lambda^2$  used for its determination. However, as we saw in Sec 4.3.2 while analyzing the fixed angle energy dependence of  $h$ , the falling effect of the coupling constant factor just about cancels the rising effect of the pinch singularity, which implies that the coefficient obtained is very close to being independent of  $t$ .

Figs. 4.13 and 4.14 show the resulting plots for the representative diagrams QH1.1 and QP1.1, respectively. Again the results of the hard diagram (QH1.1) are exactly as expected from a diagram involving the exchange of two spin- $1/2$  particles. We need to plot  $(t/s)^2 h$  in order to attain constancy with energy, which means that the amplitude  $\hat{M}_{\pi\pi}$  is asymptotically independent of  $s$  and the corresponding cross-section falls like  $1/s^2$ . The Sudakov modified pinch diagram again behaves differently (Fig. 4.14) and again falls faster than the hard diagram by a power of  $s$ . The asymptotic cross-section corresponding to this diagram will then fall like  $1/s^4$  since the asymptotic form of the amplitude is  $1/st$ .

The most interesting outcome of this analysis is that the gluon exchange pinch contribution falls with  $s$ , for small  $t/s$ , almost exactly like the contribution from the quark exchange hard diagrams. Thus, even if the quark exchange contribution is never dominant in elastic scattering processes, a dominance of the pinch contribution could just as well delay the onset of energy independent behavior of elastic cross-sections and thereby provide an alternative explanation for the observed behavior of small angle elastic data. To investigate this possibility a little further and to make rough comparisons of our calculation with  $\pi\pi$  and  $pp$  data, we now present the results of a full fledged calculation of the coefficients for all the diagrams that contribute to  $\pi\pi$  scattering. We tabulate the results using the same format that was used for the  $90^\circ$  normalization results, and we separately add the coefficients for each group of diagrams having the same asymptotic form and belonging to the same diagram-class.

Some comments regarding the detailed results presented below would be appropriate at this juncture. The four diagrams that we analyzed above *are* representative of the classes they belong to, but every diagram in a class does not always conform to this representative behavior. There are no exceptions for the pinch diagrams, of both the gluon and quark exchange types, but the two classes of hard diagrams show more variety amongst their members. First, the real part of diagrams involving triple or quadruple gluon vertices in both gluon and quark exchange hard diagrams, have an extra factor of  $s/t$  in their asymptotic form as compared to the representative diagram in that class. This would be worrisome except that the coefficients of these real parts always cancel out and do not give any net contribution. This fact is undoubtedly a manifestation of the gauge invariance of the final result. (It should be kept in mind that the coefficients for these real parts entered in the tables actually multiply a different functional form than is indicated at the head of the table.) Second, the

quark exchange hard diagrams divide into *three* groups, each one with a different asymptotic form. The group that agrees with the expectations of our general theoretical analysis of diagrams in the Regge limit is the one that consists of diagrams that include a gluon line connecting the two exchanged quarks. The other two groups fall faster with energy in the asymptotic region. The second group, which has an extra factor of  $t/s$  in its asymptotic form, consists of diagrams where neither the two exchanged quarks nor the two spectator quarks are connected with a single gluon line. The third and final group has two factors of  $t/s$  in it compared to the representative diagram and it consists of diagrams which involve a gluon line connecting the two spectator quarks. Diagrams with gluon lines between exchange as well spectator quarks of course belong to the pinch category. For the purposes of analyzing the small angle behavior of the different classes of diagrams the contributions of the last two groups can be neglected since, for small  $t/s$ , they are much smaller than the contribution of the first group.



A. GLUON EXCHANGE PINCH DIAGRAMS

$$\hat{M}_{\pi\pi} = c \frac{1}{t^2} [1 + O(t/s)]$$

DIAGRAM	$N_{sym}$	$c (-t/\Lambda^2=1000)$	
		REAL	IMAGINARY
GP1.1	8	0.05	0.0
GP1.2	8	0.02	0.0
GP2.1	8	-0.85	0.0
GP2.2	8	-0.53	0.0
GP3.1	16	0.03	0.0
TOTAL	48	-1.28	0.0

B. GLUON EXCHANGE HARD DIAGRAMS

$$\hat{M}_{\pi\pi} = c \frac{s}{t^3} [1 + O(t/s)]$$

DIAGRAM	$N_{sym}$	$c(-t/\Lambda^2=1000)$	
		REAL	IMAGINARY
GH1.1	16	0.008	0.156
GH1.2	8	0.0	-0.003
GH2.1	2	-0.045	0.135
GH3.1	1	0.045	0.0
TOTAL	27	0.008	0.288

C. QUARK EXCHANGE PINCH DIAGRAMS

$$\hat{M}_{\pi\pi} = c \frac{1}{st} [1 + O(t/s)]$$

DIAGRAM	$N_{sym}$	$c (-t/\Lambda^2=1000)$	
		REAL	IMAGINARY
QP1.1	4	0.024	0.0
QP1.2	4	0.013	0.0
QP1.3	4	0.010	0.0
QP1.4	4	-0.156	0.0
QP2.1	2	-0.006	0.0
QP2.2	2	-0.004	0.0
QP3.1	2	-0.003	0.0
QP3.2	2	-0.002	0.0
TOTAL	24	-0.125	0.0

D. QUARK EXCHANGE HARD DIAGRAMS

$$\hat{M}_{\pi\pi} = c \frac{1}{t^2} [1 + O(t/s)] \quad (I)$$

DIAGRAM	$N_{sym}$	$c(-t/\Lambda^2=1000)$	
		REAL	IMAGINARY
QH1.1	2	0.013	0.0
QH1.2	4	0.002	0.009
QH1.3	2	-0.001	0.001
QH4.1	2	0.007	0.0
QH4.2	2	0.0	0.011
QH4.3	2	0.0	0.011
QH4.4	2	-0.000	-0.001
QH4.5	2	-0.000	-0.001
QH4.6	2	-0.005	0.013
QH6.1	4	0.015	0.0
QH6.2	4	0.002	0.021
QH8.1	1	-0.002	-0.004
QH9.1	2	-0.008	-0.001
QH10.1	1	0.010	0.0
TOTAL	32	0.033	0.059

$$\hat{M}_{\pi\pi} = c \frac{1}{st} [1 + O(t/s)] \quad (\text{II})$$

DIAGRAM	$N_{sym}$	$c (-t/\Lambda^2=1000)$	
		REAL	IMAGINARY
QH3.1	4	-0.012	0.0
QH3.2	4	0.008	-0.001
QH3.3	4	0.021	0.0
QH3.4	4	0.000	-0.001
TOTAL	16	0.017	-0.002

$$\hat{M}_{\pi\pi} = c \frac{1}{s^2} [1 + O(t/s)] \quad (\text{III})$$

DIAGRAM	$N_{sym}$	$c(-t/\Lambda^2=1000)$	
		REAL	IMAGINARY
QH2.1	2	0.021	0.0
QH2.2	4	0.004	0.011
QH2.3	2	-0.004	0.003
QH5.1	2	0.019	0.0
QH5.2	4	0.0	0.017
QH5.3	4	-0.003	-0.005
QH5.4	2	-0.015	0.018
QH7.1	4	0.023	0.0
QH7.2	4	0.001	0.029
TOTAL	28	0.046	0.073

The first thing to notice from our results is that the coefficients for quark exchange contributions are again somewhat smaller than those for the gluon exchange contributions. The ratio  $c_q/c_g$ , defined in Chap. III, works out to be about 0.23 for the results of our  $\pi\pi$  calculation. This ratio is not sensitive to the value of  $-t/\Lambda^2$  at which it is evaluated and there is no reason to expect the situation to be vastly different for  $\pi p$  and  $pp$  scattering, even though the ratio of quark to gluon exchange diagrams is somewhat higher for these elastic

reactions. Let us therefore concentrate on the gluon exchange diagrams. The coefficient for the pinch diagrams is -1.28 and that for the hard diagrams is  $0.008+i0.228$ . Thus the coefficient for the pinch contribution is already somewhat bigger and if we go to higher values of  $t$  it will remain approximately constant while the coefficient for the hard contribution will fall because of the coupling constant factor, leading to a stronger and stronger domination. Because of the double-pinch effect in pp scattering, there is again reason to expect that for the pp case the pinch contribution may already be strongly dominant at  $-t/\Lambda^2=1000$ . This could then provide the explanation for the large value for the ratio  $c_q/c_g$  observed in experiment. We write below the expression for the  $\pi\pi$  cross-section coming from just the gluon exchange diagrams. The real part of the hard contribution is being ignored because it is very small.

$$\frac{d\sigma}{dt}_{\pi\pi} \sim \frac{1}{s^2} \left| i0.29 \frac{s}{t^3} - 1.28 \frac{1}{t^2} \right|^2 \quad (4.5)$$

As  $s$  is increased for a fixed value of  $t$ , the pinch contribution will soon fall away and the cross-section will be dominated by the energy independent hard contribution. Thus by looking at the region where the cross-section has achieved energy independence we automatically isolate the contribution of the hard gluon exchange diagrams. We already know from experiment that this region exists for  $\pi p$  and  $pp$  scattering, though at very high energies. From the measured cross-section in this region and from the known dependence on  $t$  from dimensional scaling we can work out the coefficient of the gluon-exchange hard contribution of  $\pi p$  and  $pp$  scattering and compare the results with the calculated coefficient for  $\pi\pi$ .

Let us first quote the numerical values of the three cross-sections at  $t=10\text{Gev}^2$  in the energy independent region. The calculated value for  $\pi\pi$ ,

assuming  $\Lambda=100$  Mev, is  $5.1 \times 10^{-35} \text{cm}^2/\text{Gev}^2$ . The measured value for  $\pi\pi$  and  $pp$  (some extrapolation is necessary for the  $\pi\pi$  case) are given by  $1.7 \times 10^{-36} \text{cm}^2/\text{Gev}^2$  and  $3.7 \times 10^{-37} \text{cm}^2/\text{Gev}^2$  respectively. These numbers of course depend strongly on  $t$  and we would therefore like to compare the expressions  $t^n(d\sigma/dt)$  which are essentially the squares of the above mentioned coefficients. However, the  $n$  is different for the three cases and therefore we must again divide by the appropriate powers of the normalization constants to get dimensionless numbers. The situation is identical to the analysis of the  $90^\circ$  results, and we basically repeat the steps of our previous analysis.

$$\frac{t^6}{C_\pi^4} \frac{d\sigma}{dt}_{\pi\pi} = 1.31 \times 10^3 \simeq [3.62 \times 10]^2$$

$$\frac{t^8}{C_\pi^2 C_p^2} \frac{d\sigma}{dt}_{\pi p} = 3.6 \times 10^3 \simeq [6.0 \times 10]^2$$

$$\frac{t^{10}}{C_p^4} \frac{d\sigma}{dt}_{pp} = 6.4 \times 10^2 \simeq [2.5 \times 10]^2$$

It now makes more sense to compare these numbers with the number of gluon exchange hard diagrams, though the uncertainties are still all there and we cannot afford to take the comparison very seriously. The following table shows this comparison:



ELASTIC REACTION	DIMENSIONLESS NUMBER	$N_{GH}$	$\sqrt{N_{GH}}$
$\pi\pi$	$\sim 36$	27	$\sim 5$
$\pi p$	$\sim 60$	$\sim 1500$	$\sim 40$
$pp$	$\sim 25$	$\sim 40,000$	$\sim 200$

The dimensionless numbers are now more or less equal to each other and show no significant dependence on  $N_{GH}$ . This is very different from the result for the  $90^\circ$  normalization. If the numbers obtained above are a better indication of the dependence of the "reduced" cross-section on the numbers of diagrams that contribute to it, then the characteristic numbers obtained for the  $90^\circ$  case are indicating the presence of a completely different effect. Unlike the situation for hard diagrams, in the case of pinch diagrams the normalization also strongly depends on the amount of enhancement coming from the pinch singularity. This enhancement can be quite different for different processes and could serve as a possible explanation for the large difference in the process dependence of wide angle and small angle normalizations. Our comparison of absolute normalizations, then, not only indicates that the magnitude of the elastic cross-section predicted by QCD is not off the mark by orders of magnitude, but it also suggests that the wide angle cross-section for  $\pi p$  and  $pp$  scattering may be dominated by the contribution of pinch diagrams even after a Sudakov factor is included in their calculation.

**FIGURE CAPTIONS**

- Fig. 4.1      The multiple scattering diagrams for  $\pi\pi$  scattering.
- Fig. 4.2      Catalog of all connected diagrams for  $\pi\pi$  scattering.
- Fig. 4.3      Plot of  $h_{90^\circ}$  against  $s/\Lambda_p^2$  for GH1.1 without the coupling constant factor.
- Fig. 4.4      Plot of  $h_{90^\circ}$  against  $s/\Lambda_\alpha^2$  for GH1.1 with coupling constant factor.
- Fig. 4.5      Plot of  $h_{90^\circ}$  against  $s/\Lambda_p^2$  for GP1.1 with no factors.
- Fig. 4.6      Plot of  $h_{90^\circ}$  against  $s/\Lambda_s^2$  for GP1.1 with only the Sudakov factor.
- Fig. 4.7      Plot of  $h_{90^\circ}$  against  $s/\Lambda_\alpha^2$  for GP1.1 with both, the Sudakov factor and the coupling constant factor.
- Fig. 4.8      Angular dependence of GP1.1 at wide angles.
- Fig. 4.9      Angular dependence of GH1.1 at wide angles.

Fig. 4.10     Plots of the function  $h_{\theta_{c.m.}}$  for several different scattering angles.  
The curves are not parallel to each other, thus proving the lack of factorization of the energy and angular dependence of the pinch contribution to  $\pi\pi$  scattering.

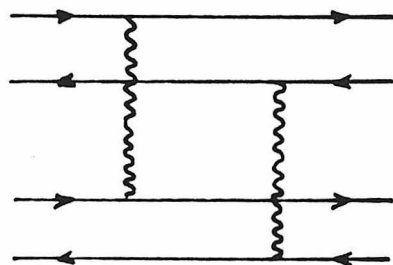
Fig. 4.11     Plot of  $(t/s)^3 h$  against  $s/\Lambda^2$  for GH1.1.

Fig. 4.12     Plot of  $(t/s)^2 h$  against  $s/\Lambda^2$  for GP1.1.

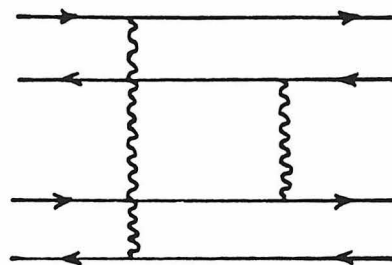
Fig. 4.13     Plot of  $(t/s)^2 h$  against  $s/\Lambda^2$  for QH1.1.

Fig. 4.14     Plot of  $(t/s) h$  against  $s/\Lambda^2$  for QP1.1.

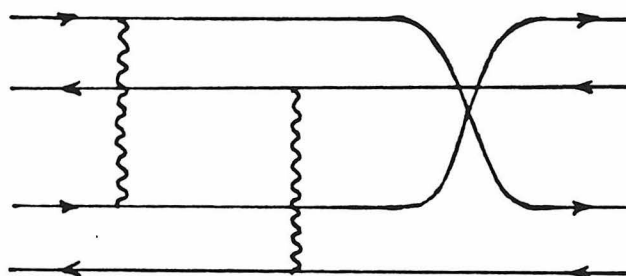
MULTIPLE SCATTERING DIAGRAMS



(a)



(b)



(c)

Fig. 4.1

# GLUON EXCHANGE PINCH DIAGRAMS

Representative Diagram	Label	No. in Symmetry Group
	GP 1.1	8
	GP 1.2	8
	GP 2.1	8
	GP 2.2	8
	GP 3.1	16

# GLUON EXCHANGE HARD DIAGRAMS

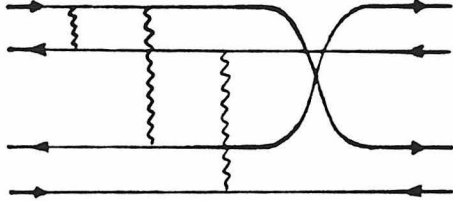
Representative Diagram	Label	No. in Symmetry Group
	GH 1.1	16
	GH 1.2	8
	GH 2.1	2
	GH 3.1	1

# QUARK EXCHANGE PINCH DIAGRAMS

Representative Diagram

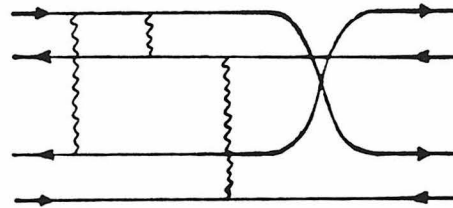
Label

No. in Symmetry Group



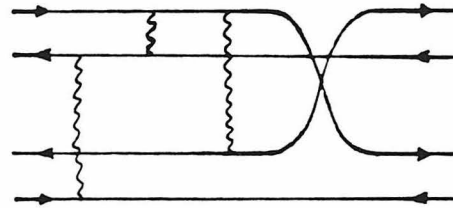
QP 1.1

4



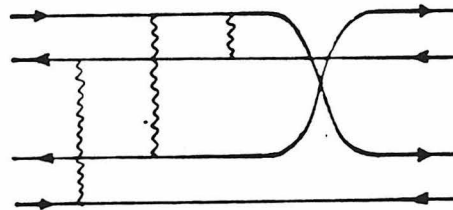
QP 1.2

4



QP 1.3

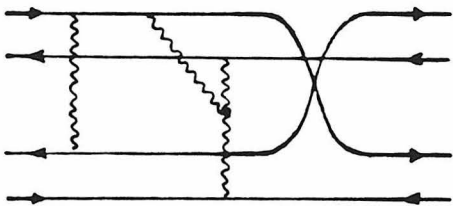
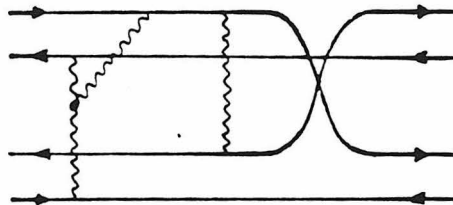
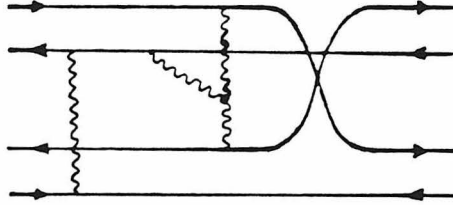
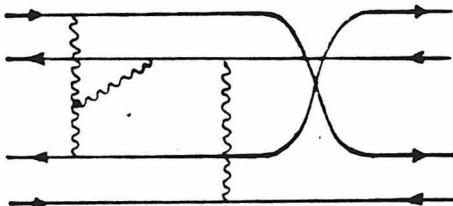
4



QP 1.4

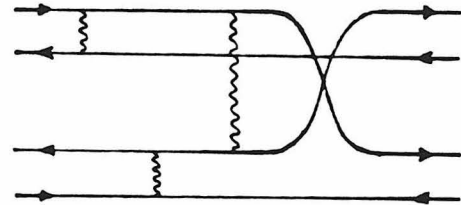
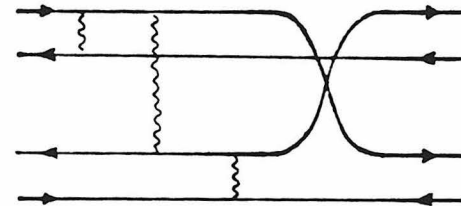
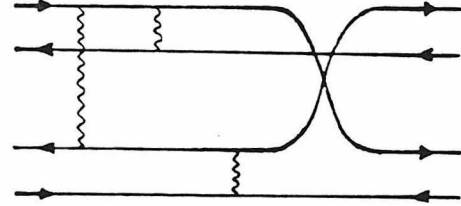
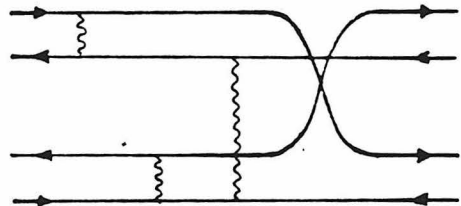
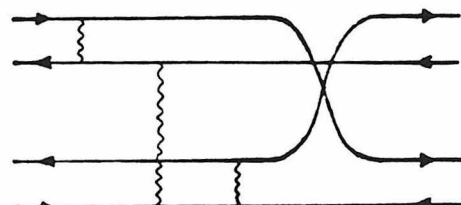
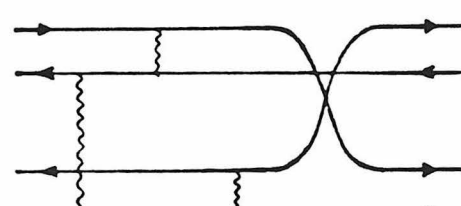
4

QUARK EXCHANGE PINCH DIAGRAMS (continued)

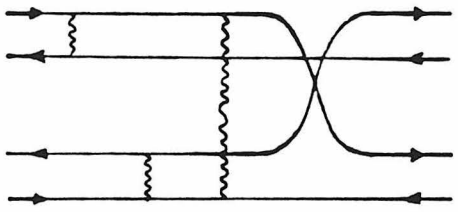
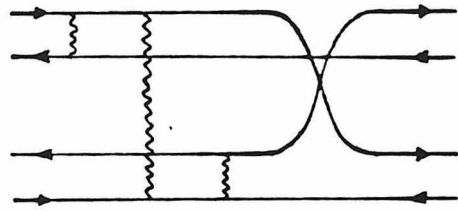
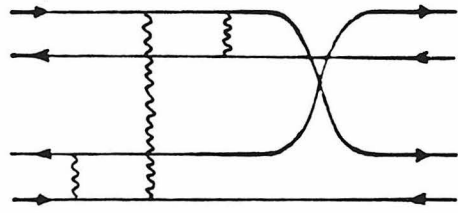
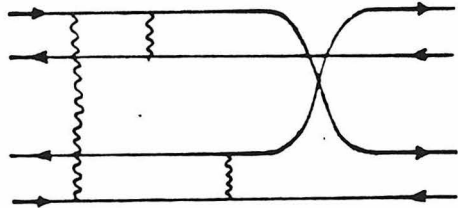
Representative Diagram	Label	No. in Symmetry Group
	QP 2.1	2
	QP 2.2	2
	QP 3.1	2
	QP 3.2	2



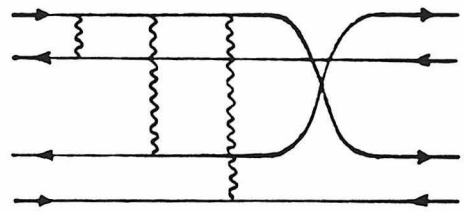
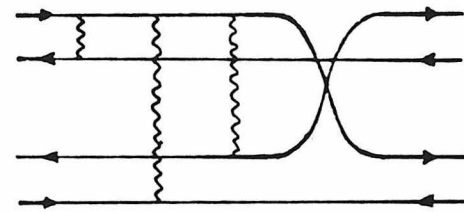
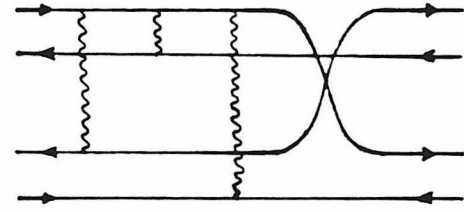
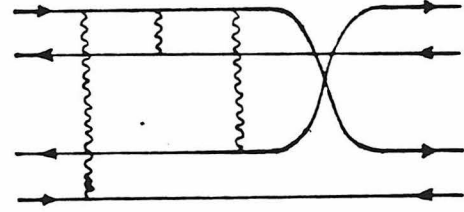
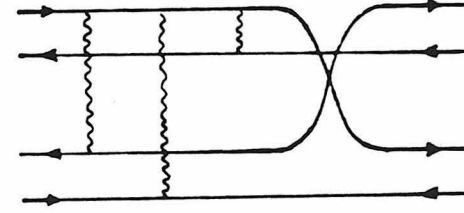
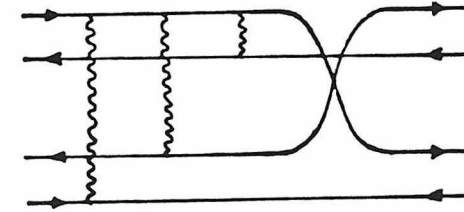
# QUARK EXCHANGE HARD DIAGRAMS

Representative Diagram	Label	No. in Symmetry Group
	QH 1.1	2
	QH 1.2	4
	QH 1.3	2
	QH 2.1	2
	QH 2.2	4
	QH 2.3	2

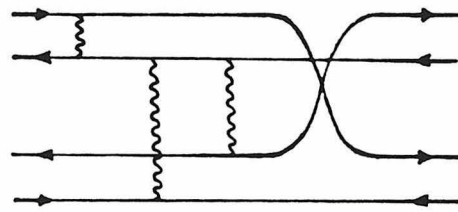
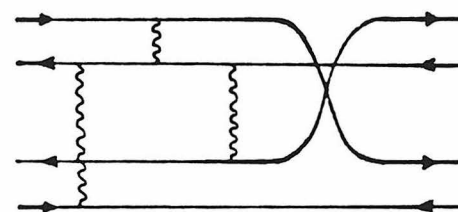
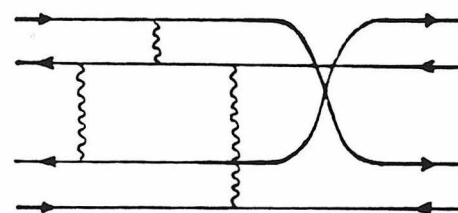
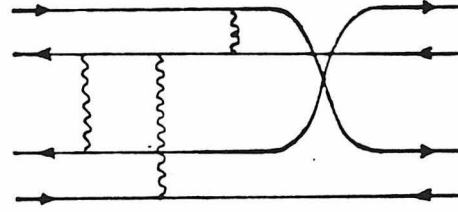
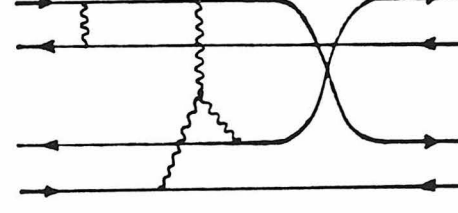
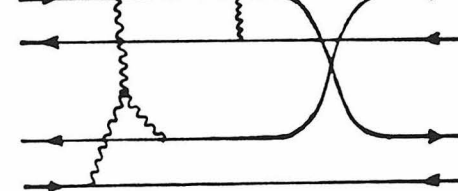
QUARK EXCHANGE HARD DIAGRAMS (continued)

Representative Diagram	Label	No. in Symmetry Group
	QH 3.1	4
	QH 3.2	4
	QH 3.3	4
	QH 3.4	4

QUARK EXCHANGE HARD DIAGRAMS (continued)

Representative Diagram	Label	No. in Symmetry Group
	QH 4.1	2
	QH 4.2	2
	QH 4.3	2
	QH 4.4	2
	QH 4.5	2
	QH 4.6	2

QUARK EXCHANGE HARD DIAGRAMS (continued)

Representative Diagram	Label	No. in Symmetry Group
	QH 5.1	2
	QH 5.2	4
	QH 5.3	4
	QH 5.4	2
	QH 6.1	4
	QH 6.2	4

QUARK EXCHANGE HARD DIAGRAMS (continued)

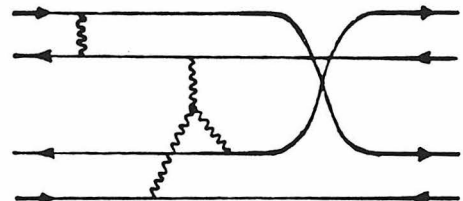
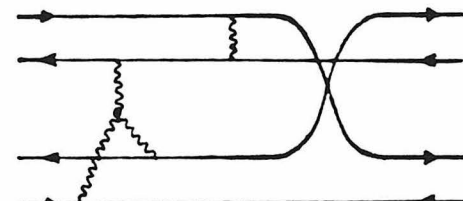
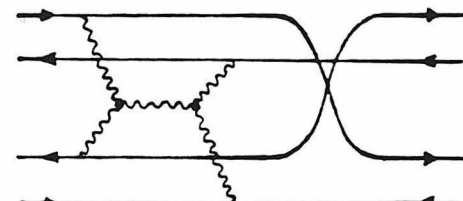
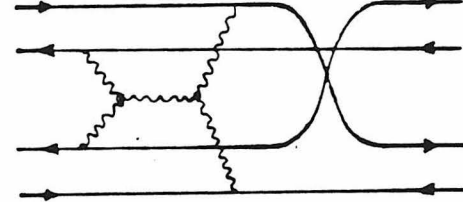
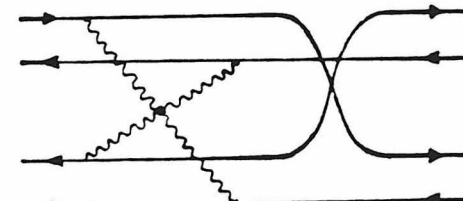
Representative Diagram	Label	No. in Symmetry Group
	QH 7.1	4
	QH 7.2	4
	QH 8.1	1
	QH 9.1	2
	QH 10.1	1

Fig. 4.2

# GH1.1 WITHOUT COUPLING CONSTANT FACTOR

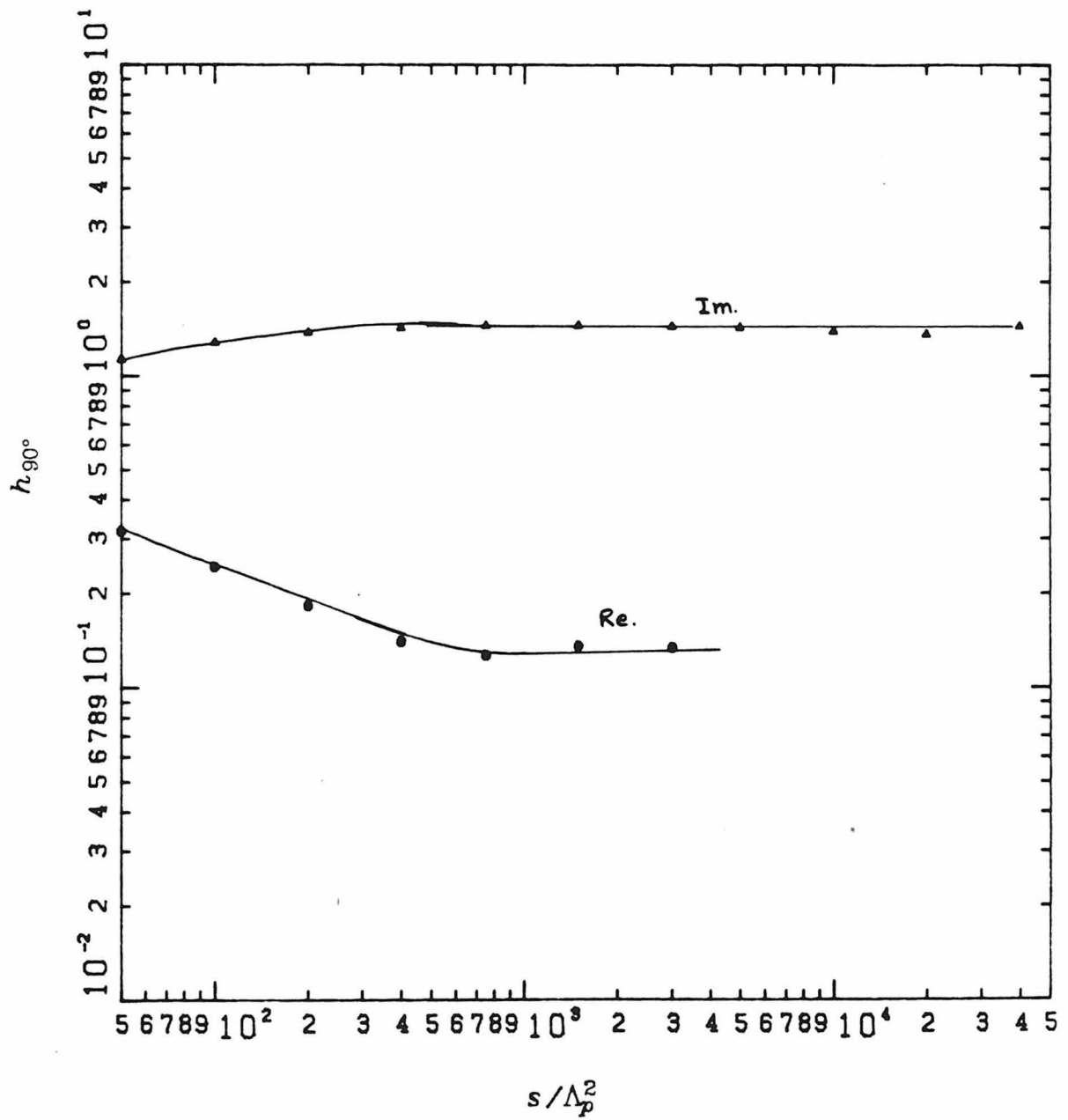


Fig. 4.3

# GH1.1 WITH COUPLING CONSTANT FACTOR

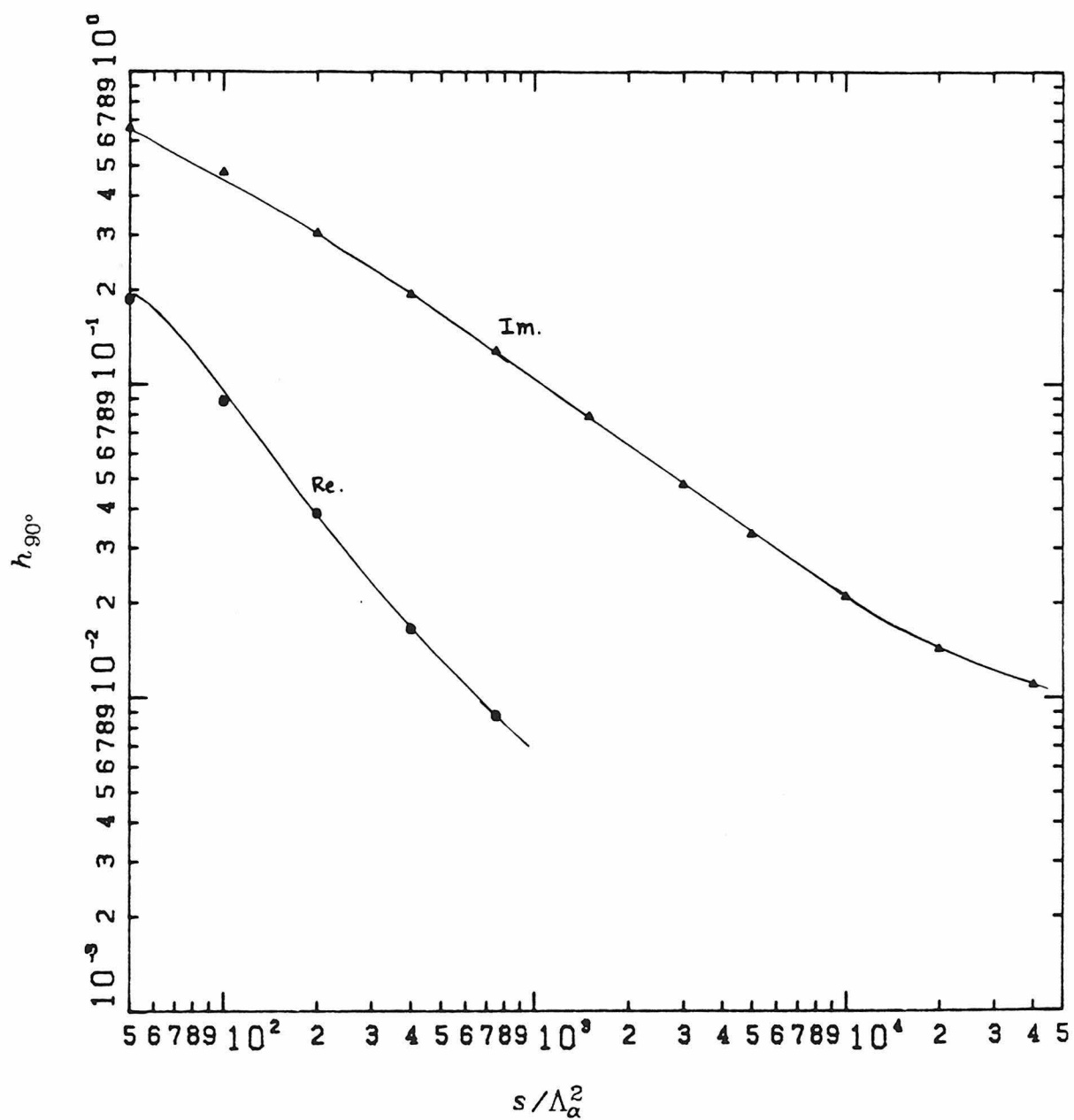


Fig. 4.4

GP1.1 WITH NO FACTORS

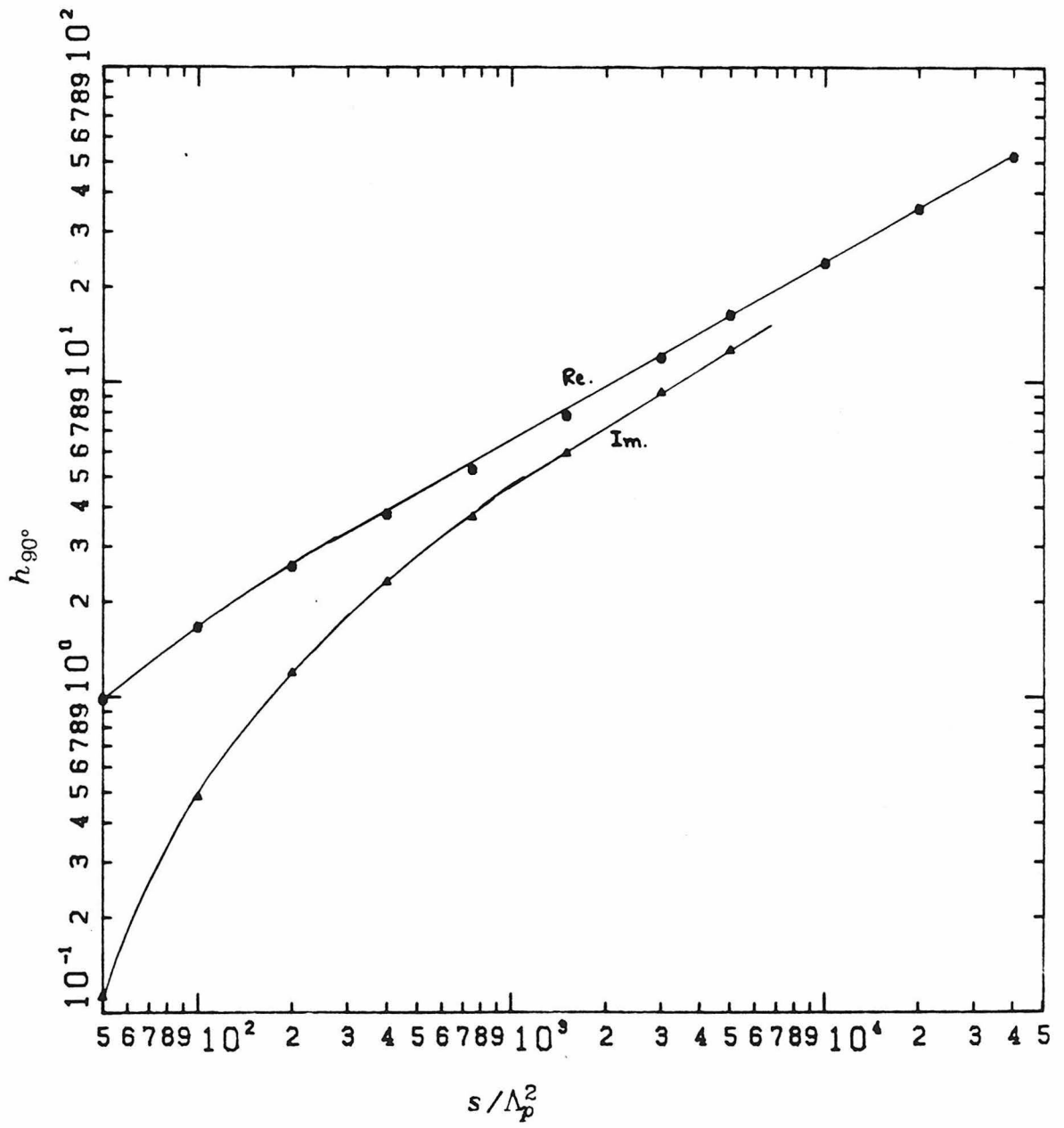


Fig. 4.5



GP1.1 WITH ONLY SUDAKOV FACTOR

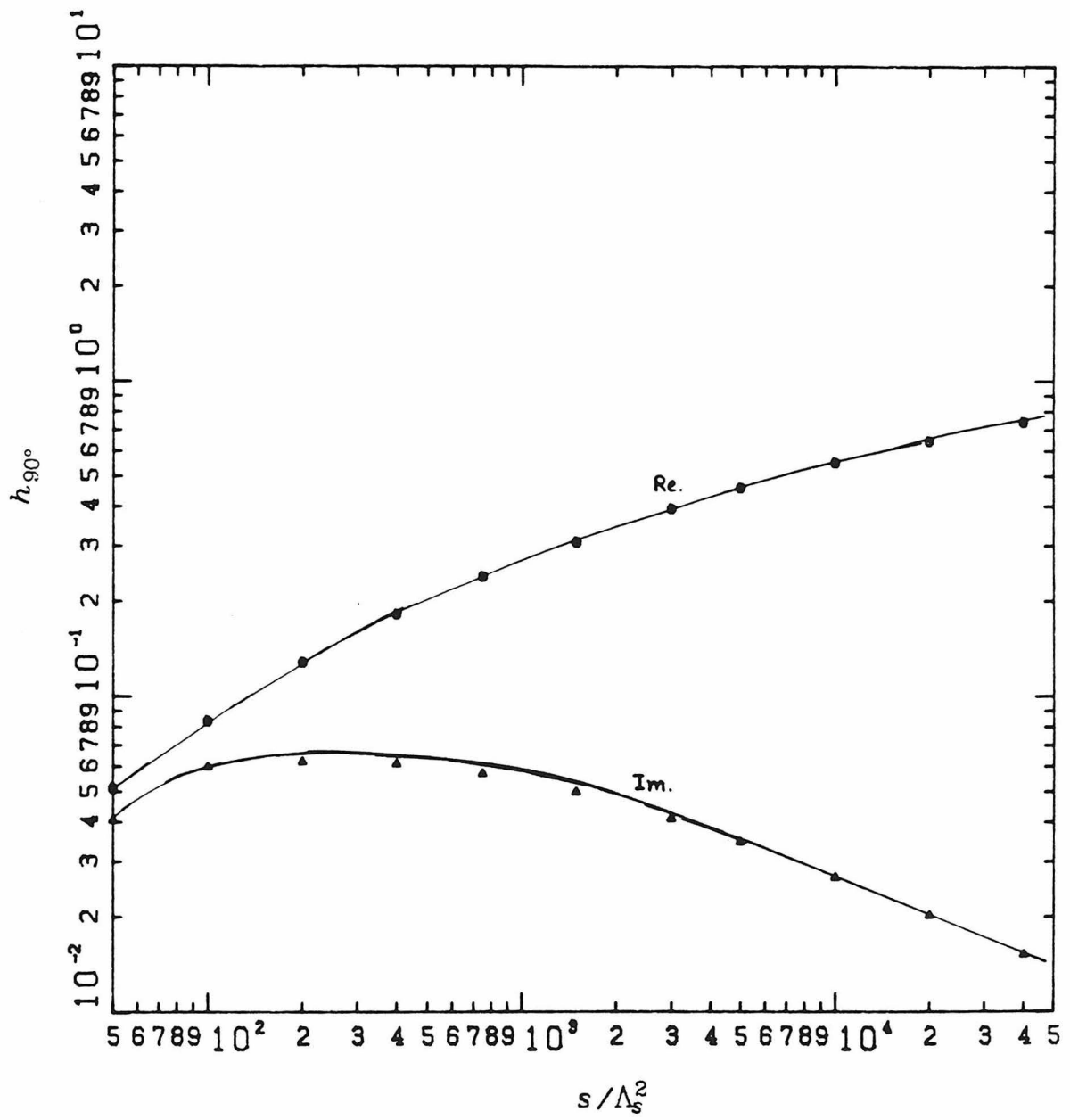


Fig. 4.6

# GP1.1 WITH SUDAKOV AND COUPLING CONSTANT FACTOR

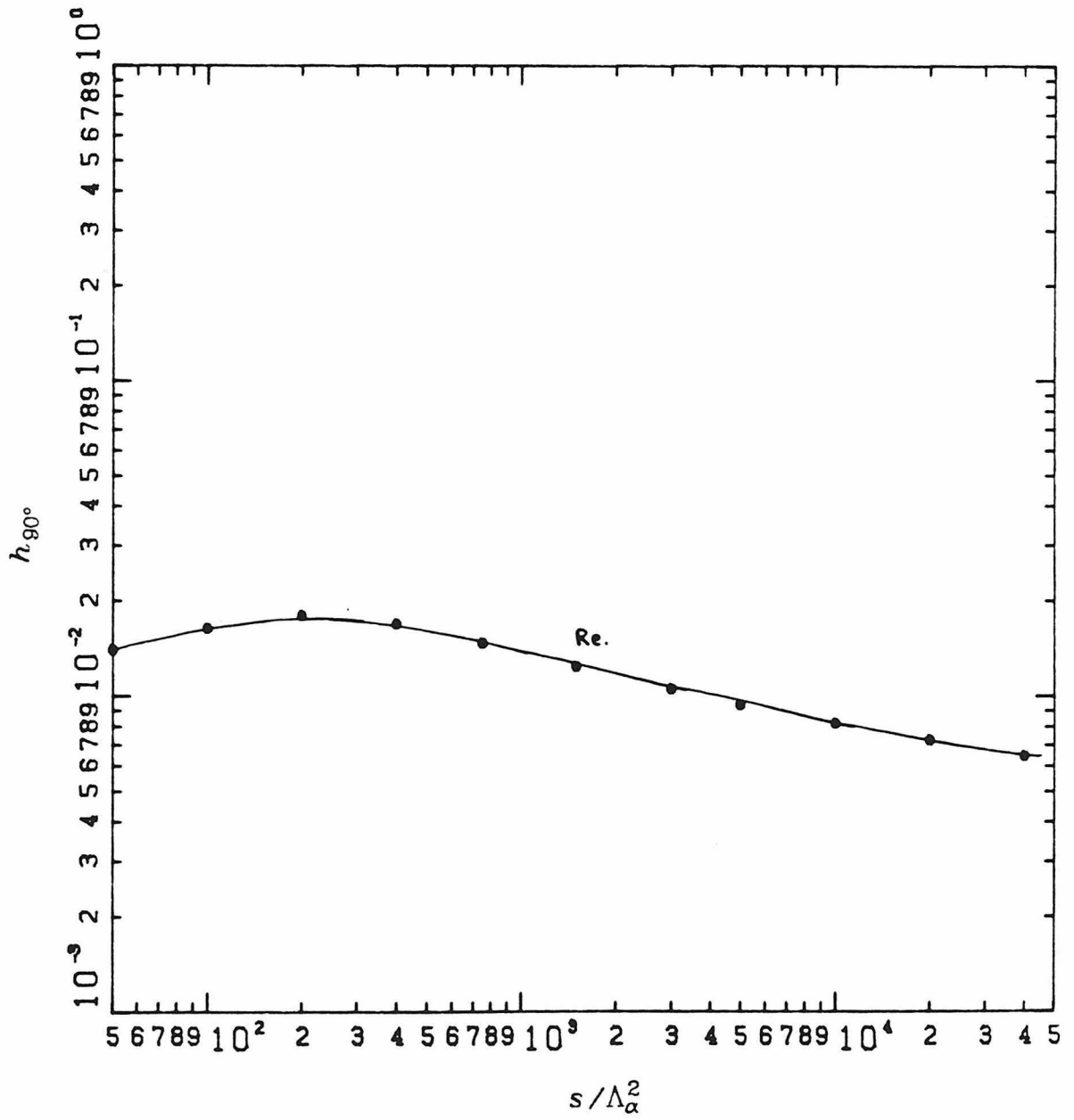


Fig. 4.7

# ANGULAR DEPENDENCE OF GP1.1

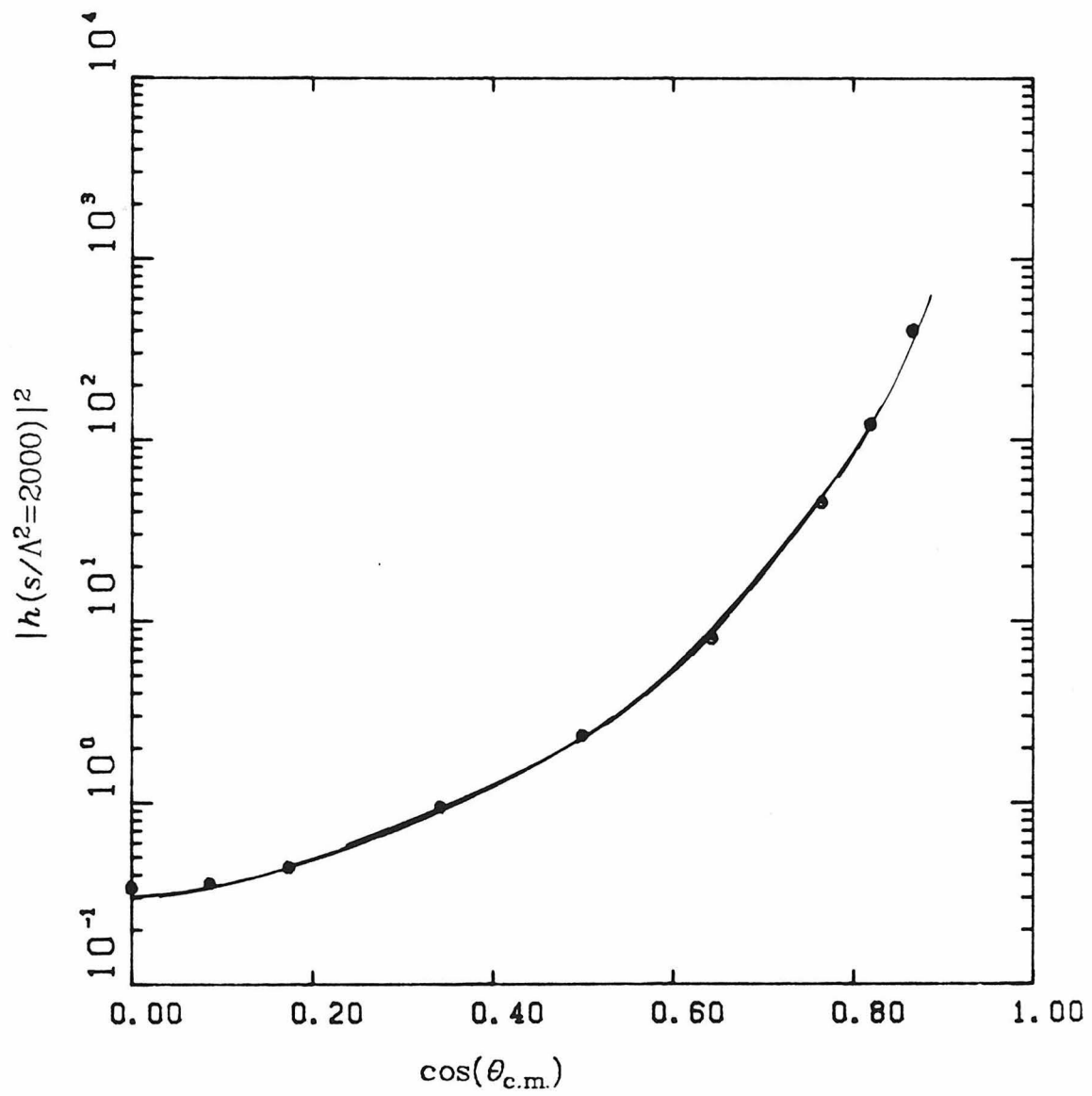


Fig. 4.8

# ANGULAR DEPENDENCE OF GH1.1

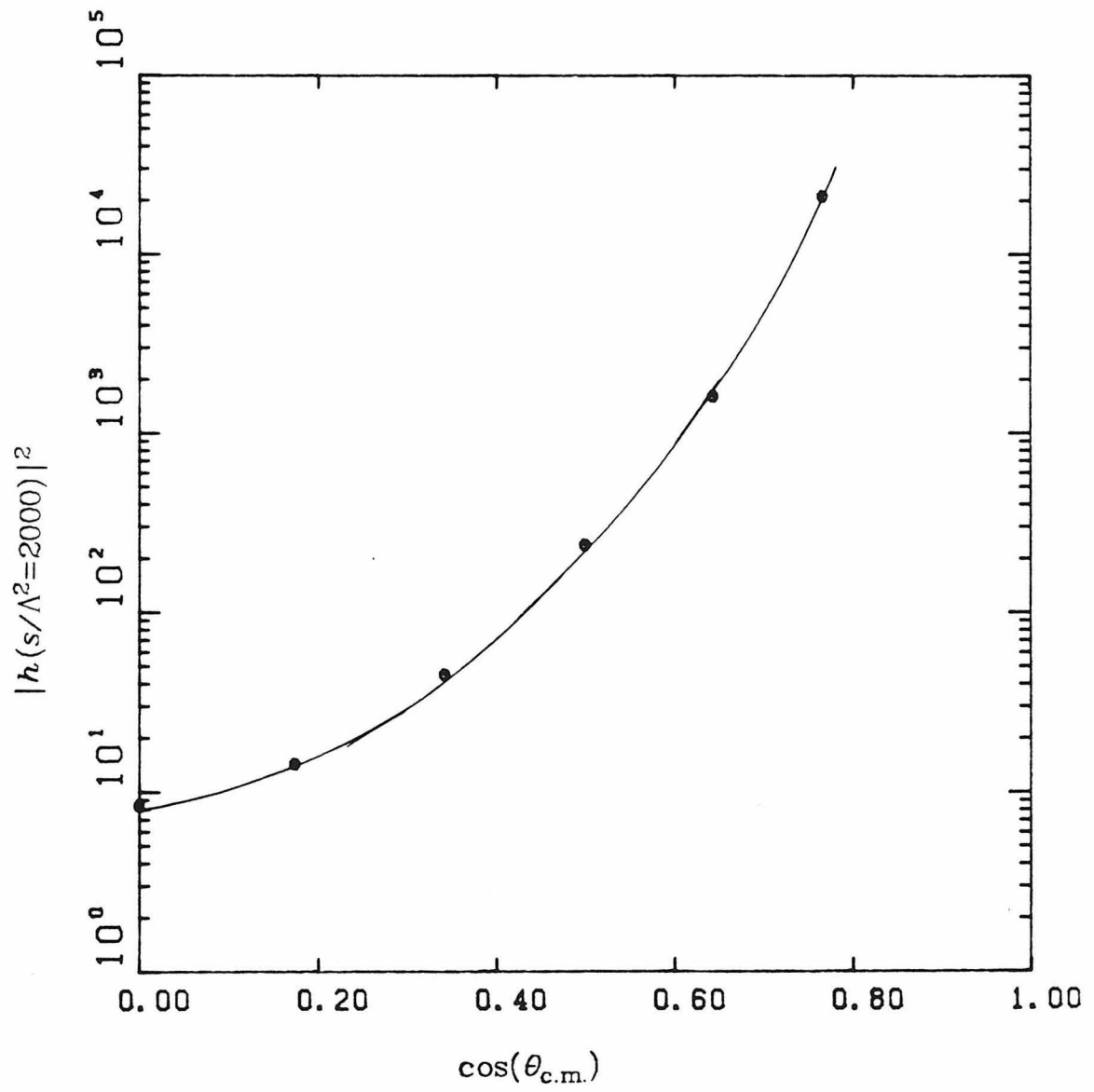


Fig. 4.9

# ANGULAR DEPENDENCE OF $h$ -FUNCTION

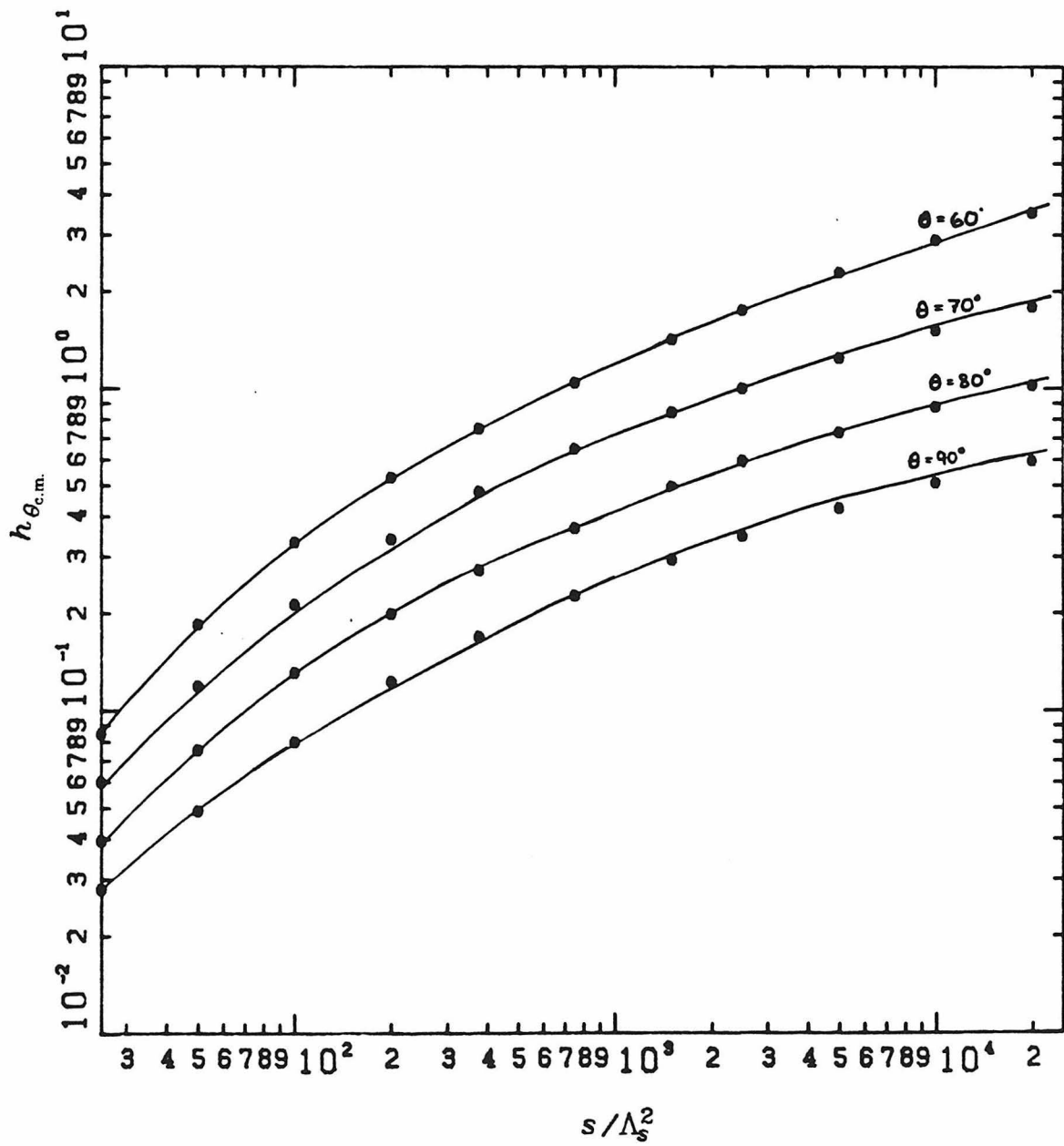


Fig. 4.10

# FIXED- $t$ PLOT FOR GH1.1

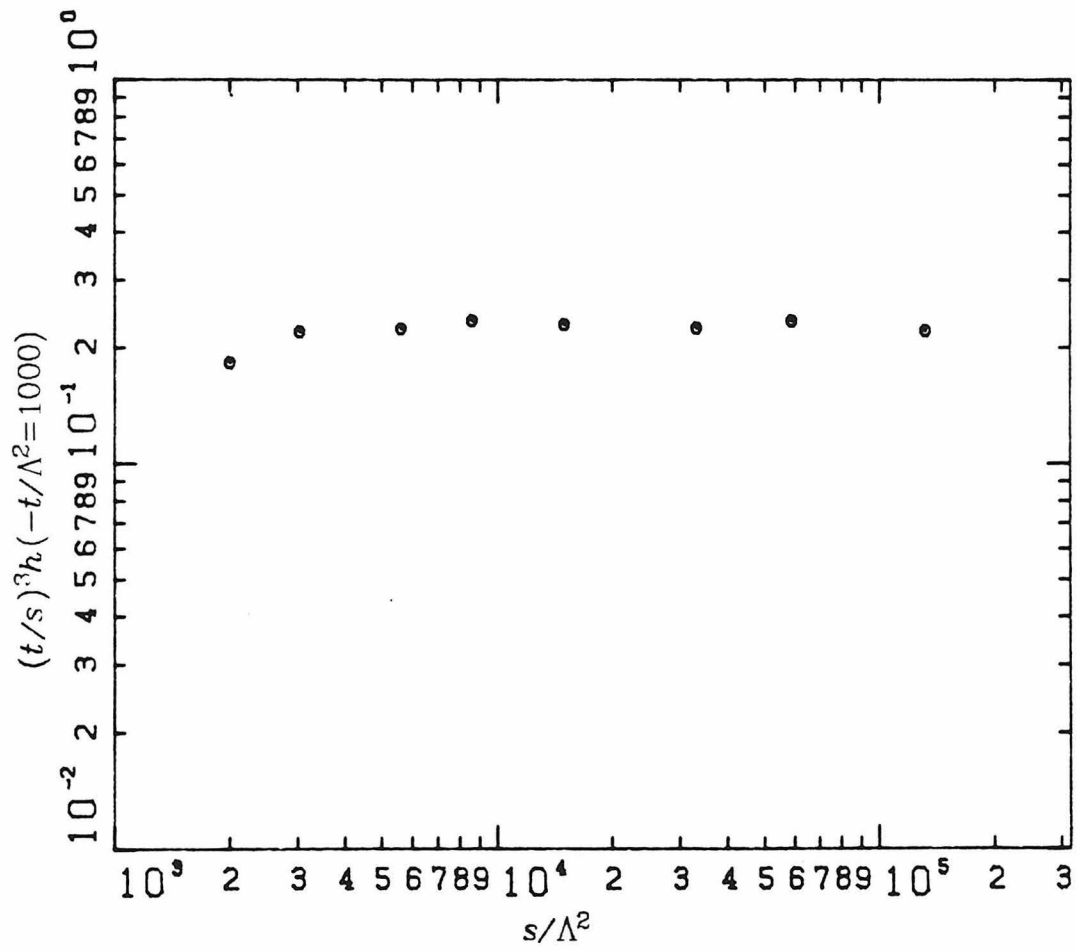


Fig. 4.11

# FIXED- $t$ PLOT FOR GP1.1

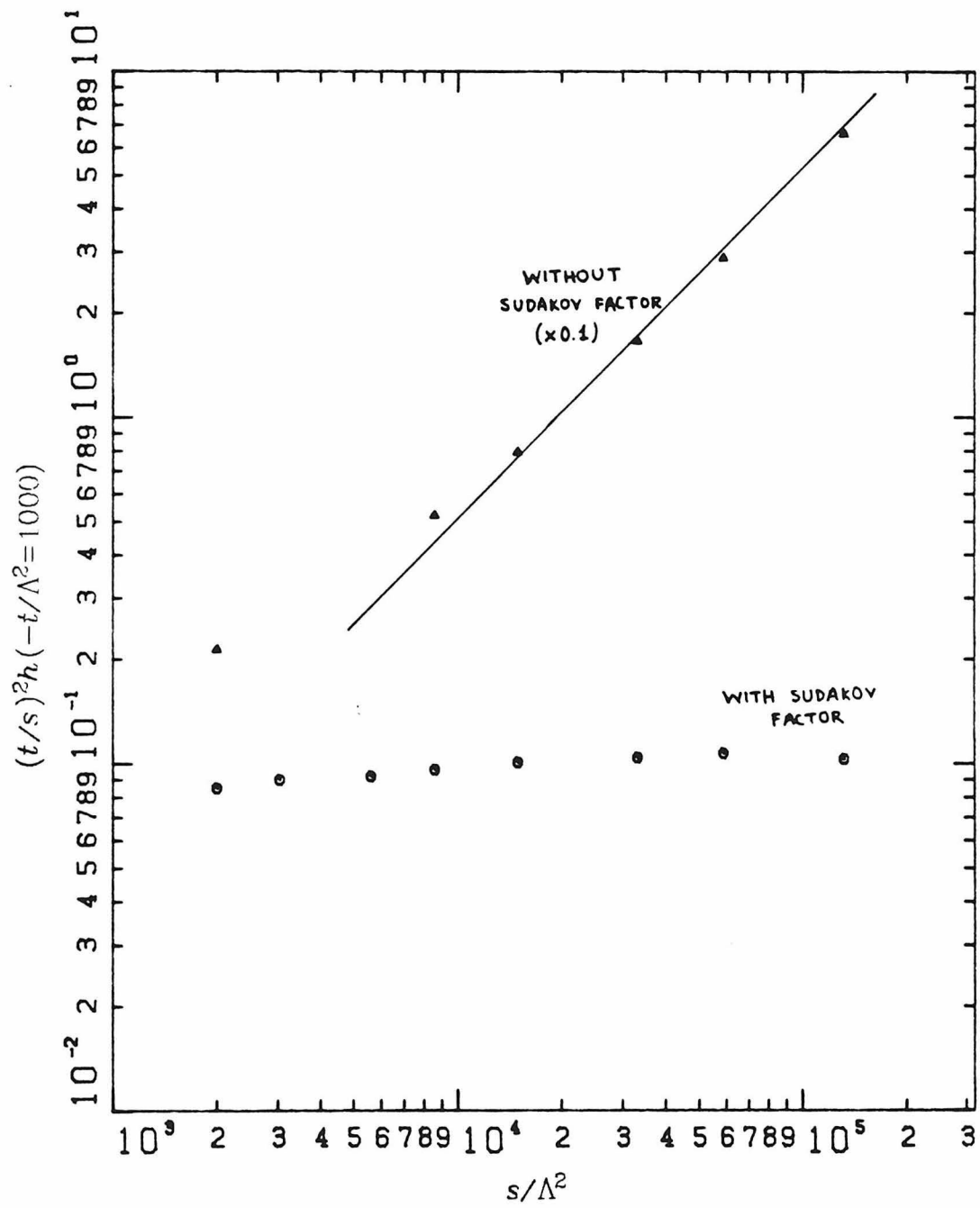


Fig. 4.12

FIXED- $t$  PLOT FOR QH1.1

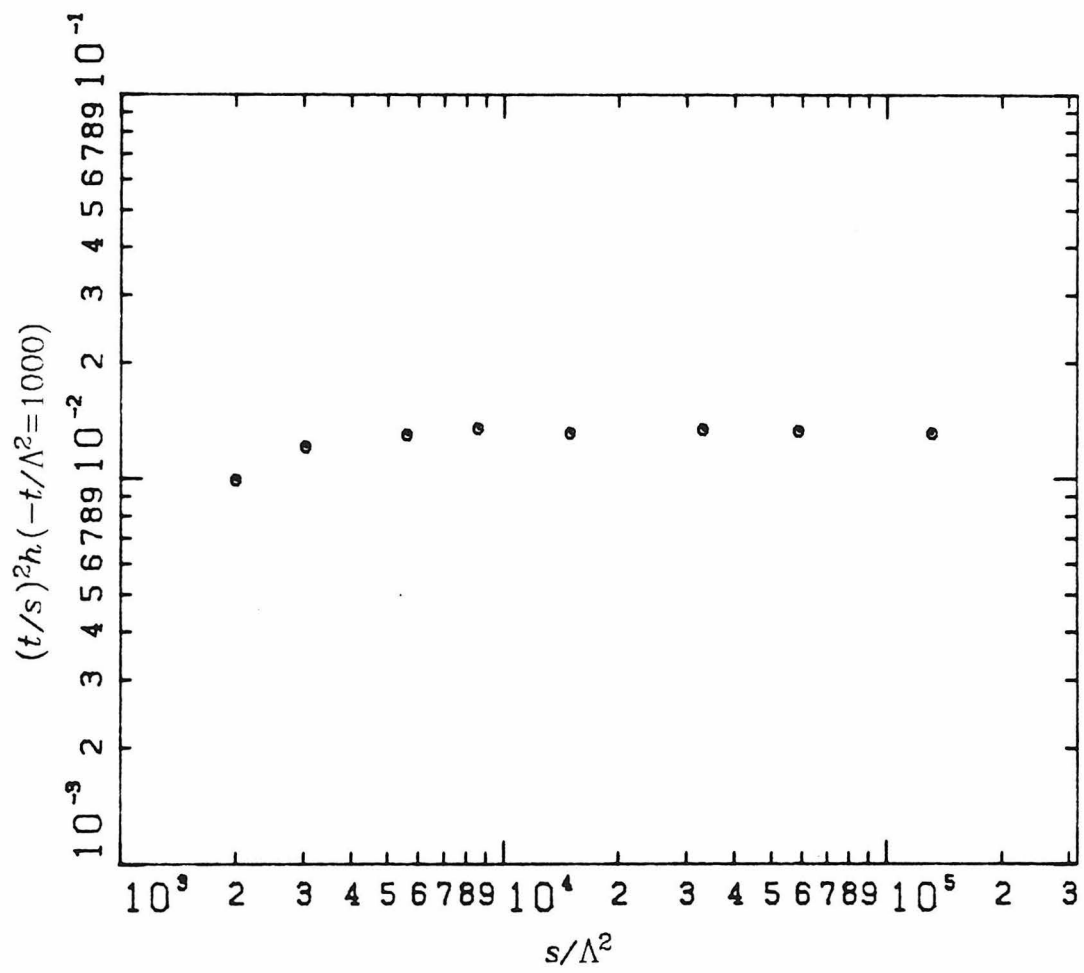


Fig. 4.13



# FIXED- $t$ PLOT FOR QP1.1

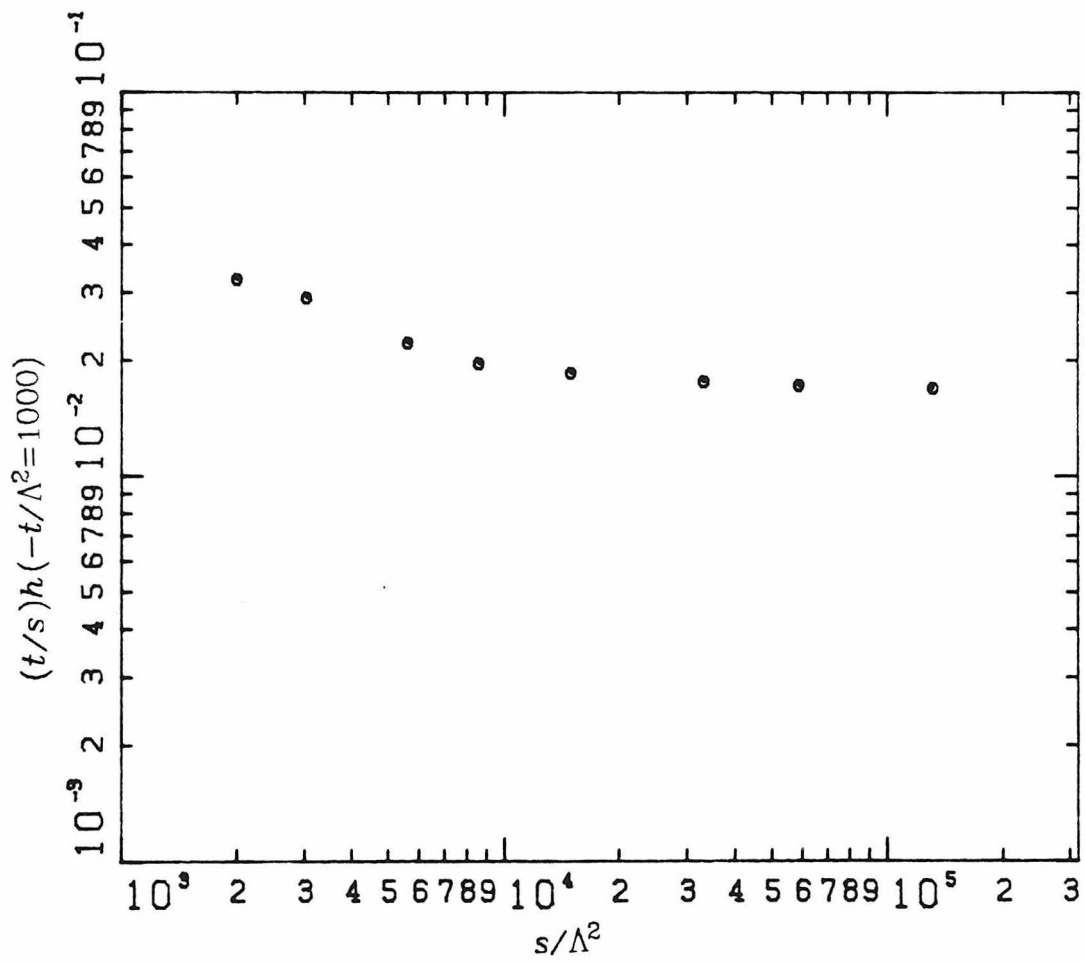


Fig. 4.14

## CHAPTER V

### SUMMARY AND CONCLUSIONS

In this thesis we have used the state of the art understanding of perturbative QCD to carry out a detailed computation of same-charge  $\pi\pi$  elastic scattering. Our calculation shows many interesting features which when generalized to  $\pi p$  and  $pp$  scattering provide us with an entirely new perspective on the interpretation of the wide angle and small angle behavior of high- $P_T$  elastic data.

Because of the good agreement with dimensional counting rules, of the energy dependence of wide angle data from many different exclusive reactions, it has come to be taken for granted that the scattering mechanism at these momentum transfers is dominated by the short distance interaction of the valence quarks in each hadron. For the case of hadron-hadron elastic scattering there exists an alternative scattering mechanism, the multiple scattering mechanism, which is not short-distance dominated and therefore poses a threat to the above interpretation. The adherents of the hard scattering interpretation usually appeal to the presence of a Sudakov factor in the amplitude for the scattering of nearly on-shell quarks, in order to show the relative insignificance of this contribution. In our theoretical review we have shown that a careful treatment, of the double-logs in the higher order corrections to multiple scattering diagrams, leads to the following conclusion: the region of momentum-fraction integration where the quarks being scattered are off-shell by an amount much greater than  $\Lambda^2$  but much less than  $s$  or  $|t|$  is not suppressed, and in fact gives rise to a non-scaling contribution because of the

presence in it of an infra-red length scale. We also show that the correct way to compute this contribution to the total scattering amplitude is to calculate and sum the amplitudes corresponding to all the so called pinch diagrams that form part of the full set of connected diagrams contributing to the hard subprocess. A Sudakov factor is of course included in the integral corresponding to these diagrams. The pinch diagrams are comparable in number to the hard ones and since their contribution falls slower with energy than the scaling contribution, there is a distinct possibility that it could be dominating the elastic cross-section at experimental energies.

Even though the experimental data seems to agree quite well with the hard scattering prediction of power-law scaling, a closer look reveals the presence of systematic deviations from this prediction. This point is well demonstrated in our experimental review, where we make use of some very recent high statistics data on  $\pi p$  and  $pp$  elastic scattering. One of the most serious problems with a hard scattering interpretation of the data is the absence of the scale-breaking effect expected from the many powers of the coupling constant present in the cross-section. Other deviations from scaling include the presence of fine structure over and above a power-law behavior, an increase in the power,  $n$ , with increasing energy and a definite dependence of  $n$  on the scattering angle. The delay in the achievement of energy independence of the fixed- $t$  cross-section with increasing  $s$  is also worrisome since the contribution of gluon exchange diagrams in QCD should be comparable to other contributions involving the interchange or annihilation of quarks. These observations taken together suggest that QCD hard scattering in its simplest form cannot account for all the features of the data at the energies involved, and either we are seeing some of the sub-asymptotic diffraction type effects which will go away at higher energies or the deviations are being caused by a different type of constituent scattering

mechanism that is sensitive to the hadronic length scale in a manner different from the usual dependence that comes from the running of the coupling constant.

The results of our detailed QCD calculation, limited though they are to  $\pi\pi$  scattering, suggest a possible explanation for the features observed in high- $P_T$  elastic data. Using the new understanding of Sudakov effects we have calculated and analyzed the pinch contribution to  $\pi\pi$  scattering and we see that its behavior is reminiscent of the behavior of elastic data in more ways than one. Whether or not this contribution dominates in  $\pi\pi$  scattering depends very much on the magnitude of the infra-red scale  $\Lambda$  used in the Sudakov factor. The exact value of this scale cannot be determined perturbatively but we do expect that it should be of the same order of magnitude as the QCD scale in the coupling constant. Our calculation certainly demonstrates the *possibility* that  $\pi p$  and  $pp$  elastic scattering may be dominated by pinch effects at experimental energies rather than hard scattering effects. If this is so then the lack of scale breaking observed in the data could be caused by a delicate balance between the opposing effects of the coupling constant factor and the partially suppressed pinch singularity. The dependence of  $n$  on energy and scattering angle is also consistent with the behavior of the  $\pi\pi$  pinch contribution. The oscillating fine structure in the data is not so easily explained, but that could well be a lingering geometrical effect not related to constituent scattering. The delay in the achievement of energy independence of the fixed- $t$  cross-section at high energies can again be explained in the context of a strong pinch dominance, because unlike the gluon exchange hard contribution the pinch contribution keeps falling with energy.

Our calculation shows no support for the constituent interchange model (CIM). The diagrams that contribute to the CIM are a small fraction of the total

number of diagrams and the contributions of these diagrams have nothing special about them. In fact despite the somewhat larger number of quark exchange diagrams, the contribution of the gluon exchange diagrams works out to be larger by an order of magnitude.

The results of this thesis provide a strong motivation to carry out a similar calculation for  $\pi p$  and  $pp$  elastic scattering, and to see if the pinch contribution does or does not dominate these cross-sections. It would also be interesting to see if the behavior of the pinch contribution can reproduce the angular dependence observed in experiment for these reactions and if it has some of the other interesting features noticed in our  $\pi\pi$  calculation. The method developed for our  $\pi\pi$  computation is completely general and can be extended to the case of  $\pi p$  or  $pp$  by merely changing a few numbers used as input into our computer program. It is estimated that each diagram for  $\pi p$  scattering will take about ten times the CPU time for a  $\pi\pi$  diagram and since there are about a hundred times more diagrams for  $\pi p$  the total time is multiplied by a factor of about a thousand. Considering that each diagram for  $\pi\pi$  scattering takes, on an average, two hours of CPU time to get 10% accuracy, this is a very large amount of time on a busy Department computer. However with faster and more efficient computers this should be possible to tackle. For the  $pp$  calculation the time will get multiplied by yet another similar factor. An interesting possibility that should be considered seriously is to use a Monte Carlo method to compute the sum of all diagram amplitudes by calculating a random set of diagrams. By using well known methods of importance sampling this could prove to be a reliable and fast method of estimating the absolute normalization of the cross-section and could enable us to test the applicability of perturbative QCD to exclusive processes.

If, as seems to be the case, the renormalization group approach is valid for calculating the measured cross-sections at the available energies, then we can

actually use the variety of data available for elastic scattering reactions to experimentally determine the magnitude of the QCD scale  $\Lambda$ , and even more interestingly, to explore the functional form of the hadron wave function that is involved in high- $P_T$  exclusive scattering. Such an investigation could provide a unifying link between the perturbative and non-perturbative domains of the theory and could help to increase our understanding of the bound state problem in QCD.

## APPENDIX

### DETAILS OF METHOD

In this appendix we present some of the details of the method used to carry out a numerical computation of the large number of Feynman diagrams encountered in the leading order calculation of  $\pi\pi$  elastic scattering. The usual method of squaring the diagram amplitude and using the casimir trick to get a trace in the numerator is not very useful because of the large number of interference terms that would be produced in this process. We would like to calculate all the amplitudes first, add them up and then square the result to get the cross-section. Thus we need a method of calculation that uses the helicity spinors of the quarks involved and carries out the detailed matrix multiplication of these spinors with the gamma matrices coming from quark-gluon vertices. This matrix multiplication leads to the determination of tensors, one for each quark line, with indices given by the Lorentz indices of the gluon polarization tensor. These indices must be contracted with each other to give the numerator of the matrix element.

The denominator is much easier to calculate. The momenta of the internal propagators can be determined by solving a set of linear equations. These momenta are then squared and multiplied to provide the denominator. The color factor for each diagram is calculated separately and then plugged into the final result of the amplitude. The actual implementation of these procedures can be understood by studying the computer program (written in FORTRAN 77) which we list below.

```
program pipi

real pie
integer tpn,grn,dgn,tmn
integer seed,sx,nx,mx,ax,bx,cx,ix
integer ns
real lz,lrz,lsz,tz(20),sz(20),lrsq(20)

real gee(4,4),eps(4,4,4,4)
real tdeg,trad
real az(-1:1,-1:1,4)
real pli(4),plf(4),p2i(4),p2f(4)
integer fm(4),dr(4)

integer q,tq,tqx,g,tg,tp,nqp
integer tv(6),ng(6,4),sg(6,4),nq(5,-1:1),nv(5,-1:1)
integer v,vi(6),vf(6,4)

real x1i,x1f,x2i,x2f,xfac
real pi(4,4),pf(4,4)
real pa(5,5),pb(5,4)
integer er
real wa(5)
real psq(5),rgp(5,20),rep(5,20),imp(5,20)
real dc,rc,red(20,4),imd(20,4)
real arg,alf(3),ca,afac(20)
real xq,sq,lx,ls,lxs,sfac(20)
```



```
real num,fun(20),rem(20,4),imm(20,4),trem(20,4),timm(20,4)
real frem(20),fimm(20)
real tfrem(20),tfimm(20),sfrem(20),sfimm(20)
real cfac,rmx,rei(20,4),imi(20,4),frei(20),fimi(20)
real fres(20),free(20),fims(20),fime(20)
```

```
common/setup/ pa,pb,pi,pf,tp
common/compt/ gee,eps,fm,dr,az
common/ngsg/ ng,sg
common/nqnv/ nq,nv,tv,tq,tqx
```

```
pie=3.1415926536
ca=(12.*pie)/25.
```

```
read(5,*) tpn,grn,dgn,tmn
read(5,*) seed,nx,bx
read(5,*) tdeg
    trad=(tdeg*pie)/180.
read(5,*) ns
read(5,*) (sz(j),j=1,ns)
do 95 j=1,ns
    tz(j)=(sz(j)*(1.-cos(trad)))/2.
```

```
95  continue
```

```
read(5,*) lz,lrz,lsz
```

```
call metric(gee)
call levciv(eps)
```

```
call vecamp(trad,az)
call hadmom(trad,p1i,p1f,p2i,p2f)
call fmdr(fm,dr)

c      * setting up the diagram functions *

read(5,*) tq,tqx,tg,tp
read(5,*) (nq(g,+1),nq(g,-1),g=1,tg)

do 215 q=1,tqx
    tv(q)=0
215 continue
do 220 g=1,tg
    q=nq(g,+1)
    tv(q)=tv(q)+1
    q=nq(g,-1)
    tv(q)=tv(q)+1
220 continue

do 230 q=1,tq
    if (tv(q).eq.1) vf(q,1)=1
    if (tv(q).eq.2) read(5,*) vf(q,1),vf(q,2)
    if (tv(q).eq.3) read(5,*) vf(q,1),vf(q,2),vf(q,3)
230 continue
do 231 q=(tq+1),tqx
    if (tv(q).eq.3) then
        vf(q,1)=1
```

```
      vf(q,2)=2
      vf(q,3)=3
    end if
    if (tv(q).eq.4) then
      vf(q,1)=1
      vf(q,2)=2
      vf(q,3)=3
      vf(q,4)=4
    end if
231  continue

      do 235 q=1,tqx
        vi(q)=0
235  continue

      do 240 g=1,tg
      do 240 ig=-1,1,2
        q=nq(g,ig)
        vi(q)=vi(q)+1
        v=vf(q,vi(q))
        nv(g,ig)=v
        ng(q,v)=g
        sg(q,v)=ig
240  continue

c      **** integrating the mtrx. elem. over ****
c      **** quark to hadron mom. fractions ****
```

```
read(5,*) ax
do 250 k=1,4
  read(5,*) (trem(j,k),j=1,ns)
  read(5,*) (timm(j,k),j=1,ns)
250 continue
read(5,*) (tfrem(j),j=1,ns)
read(5,*) (sfrem(j),j=1,ns)
read(5,*) (tfimm(j),j=1,ns)
read(5,*) (sfimm(j),j=1,ns)

cx=0
sx=seed
mx=ax

do 390 ix=(ax+1),nx

x1i=ran(sx)
x1f=ran(sx)
x2i=ran(sx)
x2f=ran(sx)

xfac=x1i*(1.-x1i)*x1f*(1.-x1f)*x2i*(1.-x2i)*x2f*(1.-x2f)

c      * initial and final values of quark mom. *

do 330 k=1,4
  pi(1,k)=  x1i*p1i(k)
```

```
pi(2,k)=(1.-x1i)*p1i(k)
pi(3,k)=  x2i*p2i(k)
pi(4,k)=(1.-x2i)*p2i(k)

pf(1,k)=  x1f*p1f(k)
pf(2,k)=(1.-x1f)*p1f(k)
pf(3,k)=  x2f*p2f(k)
pf(4,k)=(1.-x2f)*p2f(k)
330  continue

c      * setting up the matrix equations for *
c      * mom. conservation at diagram vertices *

i=1
nqp=tg+1
do 180 q=1,tq
  if (tv(q).eq.1) call setupx(i,q)
  if (tv(q).eq.2) then
    call setupl(i,nqp,q,1)
    call setupr(i,nqp,q,2)
  end if
  if (tv(q).eq.3) then
    call setupl(i,nqp,q,1)
    call setupm(i,nqp,q,2)
    call setupr(i,nqp,q,3)
  end if
180  continue
```

```
do 181 q=(tq+1),tqx
  if (tv(q).eq.3) call setp3g(i,q)
  if (tv(q).eq.4) call setp4g(i,q)
181 continue

c      * solving the matrix equations for mom. of int. lines *

call leqt1f(pa,4,tp,5,pb,0,wa,er)

c      * calculating the denominator of the matrix element *

do 170 i=1,tp
  psq(i)= pb(i,1)*pb(i,1)-pb(i,2)*pb(i,2)
1    -pb(i,3)*pb(i,3)-pb(i,4)*pb(i,4)
  do 165 j=1,ns
    lrsq(j)=(4.*lrz*lrz)/sz(j)
    rgp(i,j)=psq(i)*psq(i)+lrsq(j)*lrsq(j)
    rep(i,j)=psq(i)/rgp(i,j)
    imp(i,j)=lrsq(j)/rgp(i,j)
165  continue
170  continue

dc=psq(2)*psq(3)
if (dc.eq.0.) go to 390
rc=1./dc

mx=mx+1
```

```
do 190 j=1,ns
  red(j,1)=rc*rep(1,j)*rep(4,j)*rep(5,j)
  red(j,2)=rc*rep(1,j)*imp(4,j)*imp(5,j)
  red(j,3)=rc*imp(1,j)*rep(4,j)*imp(5,j)
  red(j,4)=rc*imp(1,j)*imp(4,j)*rep(5,j)
  imd(j,1)=rc*rep(1,j)*rep(4,j)*imp(5,j)
  imd(j,2)=rc*rep(1,j)*imp(4,j)*rep(5,j)
  imd(j,3)=rc*imp(1,j)*rep(4,j)*rep(5,j)
  imd(j,4)=rc*imp(1,j)*imp(4,j)*imp(5,j)
190  continue

c      * calculating the coupling const. factor *

do 195 j=1,ns
  afac(j)=1.
  do 185 i=1,tg
    arg=(abs(psq(i))*sz(j))/(4.*lz*lz)
    if (arg.le.1.0) then
      alf(i)=1.0
      go to 184
    end if
    alf(i)=ca/log(arg)
    if (alf(i).gt.1.0) alf(i)=1.0
184    afac(j)=afac(j)*alf(i)
185    continue
195  continue
```

c        \* calculating the suppression factor \*

```
do 200 j=1,ns
  xq=min(abs(psq(1)),abs(psq(4)),abs(psq(5)))
  sq=sz(j)/(4.*lsz*lsz)
  lx=log(xq)
  ls=log(sq)
  lxs=lx+ls
  if (lxs.le.0.0) then
    sfac(j)=0.0
  else
    sfac(j)=exp(-1.28*(ls*(log(ls)-log(lxs))+lx))
  end if
200 continue
```

c        \* evaluation of quark-line tensor amplitudes \*

```
nqp=tg+1
do 510 q=1,tq
  if (tv(q).eq.1) call compt1(q)
  if (tv(q).eq.2) call compt2(q,nqp,pb)
  if (tv(q).eq.3) call compt3(q,nqp,pb)
510 continue
do 511 q=(tq+1),tqx
  if (tv(q).eq.3) call cmpt3g(q,pb)
  if (tv(q).eq.4) call cmpt4g(q)
511 continue
```



c        \* contraction of quark-line tensor-amplitudes \*

if (tg.eq.3) call cont3(gee,num)

if (tg.eq.4) call cont4(gee,num)

if (tg.eq.5) call cont5(gee,num)

c        \* calculating and accumulating the mtrx. elem. \*

do 380 j=1,ns

  fun(j)=num\*xfac\*sfac(j)

  do 385 k=1,4

    rem(j,k)=fun(j)\*red(j,k)

    trem(j,k)=trem(j,k)+rem(j,k)

    imm(j,k)=fun(j)\*imd(j,k)

    timm(j,k)=timm(j,k)+imm(j,k)

385    continue

  frem(j)=rem(j,1)-rem(j,2)-rem(j,3)-rem(j,4)

  tfrem(j)=tfrem(j)+frem(j)

  sfrem(j)=sfrem(j)+frem(j)\*frem(j)

  fimm(j)=imm(j,1)+imm(j,2)+imm(j,3)-imm(j,4)

  tfimm(j)=tfimm(j)+fimm(j)

  sfimm(j)=sfimm(j)+fimm(j)\*fimm(j)

380    continue

cx=cx+1

if (cx.eq.bx) then

  print \*,ix

```
do 340 k=1,4
  print *,(trem(j,k),j=1,ns)
  print *,(timm(j,k),j=1,ns)
340  continue
  print *,(tfrem(j),j=1,ns)
  print *,(sfrem(j),j=1,ns)
  print *,(tfimm(j),j=1,ns)
  print *,(sfimm(j),j=1,ns)
  cx=0
end if

390  continue

  print 400,tpn,grn,dgn,tmn
400  format (1x,4i5)

  print 395,seed,mx,lz,lrz,lsz,tdeg
395  format (/(4x,i10,5x,i8,5x,f4.1,2x,f4.1,2x,f4.1,5x,f5.1))

c      * the integrated answer and its formal error *

  read(5,*) cfac
  rmx=real(mx)

  print 405,'REAL'
405  format (1x,a4)
```

```
do 430 j=1,ns
  do 410 k=1,4
    rei(j,k)=(trem(j,k)*cfac)/rmx
410  continue
    frei(j)=(tfrem(j)*cfac)/rmx
    fres(j)=(sfrem(j)*cfac*cfac)/rmx
    free(j)=sqrt((fres(j)-(frei(j)*frei(j)))/rmx)
    print 420,sz(j),(rei(j,k),k=1,4),frei(j),free(j)
420  format (1x,f8.1,5x,4e12.3,5x,e10.3,5x,e10.3)
430  continue

    print 435,'IMAGINARY'
435  format (1x,a9)

do 460 j=1,ns
  do 440 k=1,4
    imi(j,k)=(timm(j,k)*cfac)/rmx
440  continue
    fimi(j)=(tfimm(j)*cfac)/rmx
    fims(j)=(sfimm(j)*cfac*cfac)/rmx
    fime(j)=sqrt((fims(j)-(fimi(j)*fimi(j)))/rmx)
    print 450,sz(j),(imi(j,k),k=1,4),fimi(j),fime(j)
450  format (1x,f8.1,5x,4e12.3,5x,e10.3,5x,e10.3)
460  continue

stop
end
```

```
      subroutine compt1(q)
c      * components of t1 *

      integer q
      real gee(4,4),eps(4,4,4,4)
      integer fm(4),dr(4)
      real az(-1:1,-1:1,4)
      real t1(4,-1:1,4),t2(4,-1:1,4,4),t3(4,-1:1,4,4,4)
      real t3g(6,4,4,4),t4g(6,4,4,4,4)
      common/compt/ gee,eps,fm,dr,az
      common/tensor/ t1,t2,t3,t3g,t4g

      do 415 ih=-1,1,2
      do 410 i=1,4
         t1(q,ih,i)=az(dr(q),ih,i)*real(fm(q))
410  continue
415  continue

      return
      end
```

```
      subroutine compt2(q,nqp,pb)
c      * components of t2 *

      integer q,nqp
      real pb(5,4)
```

```
real a(4),b(4),p(4)
real c1,c2(4,4)
real gee(4,4),eps(4,4,4,4)
integer fm(4),dr(4)
real az(-1:1,-1:1,4)
real t1(4,-1:1,4),t2(4,-1:1,4,4),t3(4,-1:1,4,4,4)
real t3g(6,4,4,4),t4g(6,4,4,4,4)
common/compt/ gee,eps,fm,dr,az
common/tensor/ t1,t2,t3,t3g,t4g

do 460 ih=-1,1,2

do 420 i=1,4
  a(i)=az(dr(q),ih,i)
  b(i)=az(dr(q),ih,i)*real(ih)
  p(i)=pb(nqp,i)
420 continue

c1=0.

do 430 i=1,4
  c1=c1+gee(i,i)*p(i)*a(i)
430 continue

do 450 i=1,4
do 450 j=1,4
  c2(i,j)=0.
do 440 k=1,4
```

```
do 440 l=1,4
    c2(i,j)=c2(i,j)+gee(k,k)*gee(l,l)*eps(i,k,j,l)*p(k)*b(l)
440  continue
    t2(q,ih,i,j)=p(i)*a(j)+a(i)*p(j)-c1*gee(i,j)+c2(i,j)
450  continue

460  continue

nqp=nqp+1

return

end

subroutine compt3(q,nqp,pb)
c      * components of t3 *

integer q,nqp
real pb(5,4)
real a(4),b(4),p1(4),p2(4)
real a1,a2,a3,b1(4),c1(4,4),c2(4,4),c3(4,4),d1(4,4,4)
real z1,z2,z3,z4,z5,z6,z7,z8
real gee(4,4),eps(4,4,4,4)
integer fm(4),dr(4)
real az(-1:1,-1:1,4)
real t1(4,-1:1,4),t2(4,-1:1,4,4),t3(4,-1:1,4,4,4)
real t3g(6,4,4,4),t4g(6,4,4,4,4)
```

```
common/compt/ gee,eps,fm,dr,az
```

```
common/tensor/ t1,t2,t3,t3g,t4g
```

```
do 490 ih=-1,1,2
```

```
do 460 i=1,4
```

```
  a(i)=az(dr(q),ih,i)
```

```
  b(i)=az(dr(q),ih,i)*real(ih)
```

```
  p1(i)=pb((nqp+1),i)
```

```
  p2(i)=pb(nqp,i)
```

```
460  continue
```

```
  a1=0.
```

```
  a2=0.
```

```
  a3=0.
```

```
do 465 i=1,4
```

```
  a1=a1+gee(i,i)*p1(i)*a(i)
```

```
  a2=a2+gee(i,i)*p2(i)*a(i)
```

```
  a3=a3+gee(i,i)*p1(i)*p2(i)
```

```
465  continue
```

```
do 470 i=1,4
```

```
  b1(i)=0.
```

```
do 470 j=1,4
```

```
  c1(i,j)=0.
```

```
  c2(i,j)=0.
```

```
  c3(i,j)=0.
```

```

do 470 k=1,4
    d1(i,j,k)=0.
do 470 l=1,4
    b1(i)=b1(i)+gee(j,j)*gee(k,k)*gee(l,l)*eps(j,i,k,l)
1      *p1(j)*p2(k)*b(l)
    c1(i,j)=c1(i,j)+gee(k,k)*gee(l,l)*eps(i,k,j,l)*p1(k)*b(l)
    c2(i,j)=c2(i,j)+gee(k,k)*gee(l,l)*eps(i,k,j,l)*p2(k)*b(l)
    c3(i,j)=c3(i,j)+gee(k,k)*gee(l,l)*eps(k,i,l,j)
1      *p1(k)*p2(l)
    d1(i,j,k)=d1(i,j,k)+gee(l,l)*eps(i,j,k,l)*b(l)
470  continue

do 480 i=1,4
do 480 j=1,4
do 480 k=1,4
    z1=a(i)*(p1(j)*p2(k)+p2(j)*p1(k))
    z2=a(j)*(p1(i)*p2(k)-p2(i)*p1(k))
    z3=a(k)*(p1(i)*p2(j)+p2(i)*p1(j))
    z4=a1*(-gee(i,j)*p2(k)+gee(j,k)*p2(i)-gee(i,k)*p2(j))
    z5=a2*( gee(i,j)*p1(k)-gee(j,k)*p1(i)-gee(i,k)*p1(j))
    z6=a3*( gee(i,j)*a(k)+gee(j,k)*a(i)-gee(i,k)*a(j))
    z7=c1(i,k)*p2(j)+c2(i,k)*p1(j)-a3*d1(i,j,k)
    z8=c3(j,i)*b(k)+c3(j,k)*b(i)-gee(i,k)*b1(j)
    t3(q,ih,i,j,k)=(z1+z2+z3+z4+z5-z6+z7-z8)*real(fm(q))
480  continue

490  continue

```



```
nqp=nqp+2

return
end

subroutine cmpt3g(q,pb)
c      * components of t3g *

integer q
real pb(5,4)
real p1(4),p2(4),p3(4)
real gee(4,4),eps(4,4,4,4)
integer fm(4),dr(4)
real az(-1:1,-1:1,4)
integer ng(6,4),sg(6,4)
real t1(4,-1:1,4),t2(4,-1:1,4,4),t3(4,-1:1,4,4,4)
real t3g(6,4,4,4),t4g(6,4,4,4,4)
common/compt/ gee,eps,fm,dr,az
common/ngsg/ ng,sg
common/tensor/ t1,t2,t3,t3g,t4g

do 485 i=1,4
  p1(i)=pb(ng(q,1),i)*sg(q,1)
  p2(i)=pb(ng(q,2),i)*sg(q,2)
  p3(i)=pb(ng(q,3),i)*sg(q,3)
485 continue
```

```

do 490 i=1,4
do 490 j=1,4
do 490 k=1,4
    t3g(q,i,j,k)= (p1(k)-p2(k))*gee(i,j)
1      +(p2(i)-p3(i))*gee(j,k)
2      +(p3(j)-p1(j))*gee(i,k)
490 continue

return
end

subroutine cmpt4g(q)
c      * components of t4g *

integer q
real gee(4,4),eps(4,4,4,4)
integer fm(4),dr(4)
real az(-1:1,-1:1,4)
real t1(4,-1:1,4),t2(4,-1:1,4,4),t3(4,-1:1,4,4,4)
real t3g(6,4,4,4),t4g(6,4,4,4,4)
common/compt/ gee,eps,fm,dr,az
common/tensor/ t1,t2,t3,t3g,t4g

do 490 i=1,4
do 490 j=1,4
do 490 k=1,4

```

```

do 490 l=1,4
    t4g(q,i,j,k,l)=gee(i,k)*gee(j,l)-gee(i,l)*gee(j,k)
490 continue

return

end

subroutine cont3(gee,num)
c      * contraction of quark-line tensor-amplitudes *

    real gee(4,4),num
    integer id(6,4),q,ih
    real tc(4,-1:1),tcx(6)
    real sgn,term1,term2,term3,term
    real t1(4,-1:1,4),t2(4,-1:1,4,4),t3(4,-1:1,4,4,4)
    real t3g(6,4,4,4),t4g(6,4,4,4,4)
    integer nq(5,-1:1),nv(5,-1:1),tv(6),tq,tqx
    common/tensor/ t1,t2,t3,t3g,t4g
    common/nqnv/ nq,nv,tv,tq,tqx

    num=0.

do 551 i1=1,4
    id(nq(1,+1),nv(1,+1))=i1
    id(nq(1,-1),nv(1,-1))=i1
do 552 i2=1,4
    id(nq(2,+1),nv(2,+1))=i2

```

```
      id(nq(2,-1),nv(2,-1))=i2
do 553 i3=1,4
      id(nq(3,+1),nv(3,+1))=i3
      id(nq(3,-1),nv(3,-1))=i3

do 530 q=1,tq
do 520 ih=-1,1,2
      if (tv(q).eq.1) tc(q,ih)=t1(q,ih,id(q,1))
      if (tv(q).eq.2) tc(q,ih)=t2(q,ih,id(q,2),id(q,1))
      if (tv(q).eq.3) tc(q,ih)=t3(q,ih,id(q,3),id(q,2),id(q,1))
520  continue
530  continue
      do 531 q=(tq+1),tqx
          if (tv(q).eq.3) tcx(q)=t3g(q,id(q,1),id(q,2),id(q,3))
          if (tv(q).eq.4) tcx(q)=t4g(q,id(q,1),id(q,2),id(q,3),
1              id(q,4))
531  continue

      sgn=gee(i1,i1)*gee(i2,i2)*gee(i3,i3)
      term1=tc(1,+1)*tc(2,-1)+tc(1,-1)*tc(2,+1)
      term2=tc(3,+1)*tc(4,-1)+tc(3,-1)*tc(4,+1)
      term3=1.
      do 535 q=(tq+1),tqx
          term3=term3*tcx(q)
535  continue
      term=sgn*term1*term2*term3
```

```
num=num+term

553 continue
552 continue
551 continue

return
end

subroutine cont4(gee,num)
c      * contraction of quark-line tensor-amplitudes *

real gee(4,4),num
integer id(6,4),q,ih
real tc(4,-1:1),tcx(6)
real sgn,term1,term2,term3,term
real t1(4,-1:1,4),t2(4,-1:1,4,4),t3(4,-1:1,4,4,4)
real t3g(6,4,4,4),t4g(6,4,4,4,4)
integer nq(5,-1:1),nv(5,-1:1),tv(6),tq,tqx
common/tensor/ t1,t2,t3,t3g,t4g
common/nqnv/ nq,nv,tv,tq,tqx

num=0.
do 551 i1=1,4
  id(nq(1,+1),nv(1,+1))=i1
  id(nq(1,-1),nv(1,-1))=i1
```

```
do 552 i2=1,4
    id(nq(2,+1),nv(2,+1))=i2
    id(nq(2,-1),nv(2,-1))=i2
do 553 i3=1,4
    id(nq(3,+1),nv(3,+1))=i3
    id(nq(3,-1),nv(3,-1))=i3
do 554 i4=1,4
    id(nq(4,+1),nv(4,+1))=i4
    id(nq(4,-1),nv(4,-1))=i4

do 530 q=1,tq
do 520 ih=-1,1,2
    if (tv(q).eq.1) tc(q,ih)=t1(q,ih,id(q,1))
    if (tv(q).eq.2) tc(q,ih)=t2(q,ih,id(q,2),id(q,1))
    if (tv(q).eq.3) tc(q,ih)=t3(q,ih,id(q,3),id(q,2),id(q,1))
520 continue
530 continue
do 531 q=(tq+1),tqx
    if (tv(q).eq.3) tcx(q)=t3g(q,id(q,1),id(q,2),id(q,3))
    if (tv(q).eq.4) tcx(q)=t4g(q,id(q,1),id(q,2),id(q,3),
1          id(q,4))
531 continue

sgn=gee(i1,i1)*gee(i2,i2)*gee(i3,i3)*gee(i4,i4)
term1=tc(1,+1)*tc(2,-1)+tc(1,-1)*tc(2,+1)
term2=tc(3,+1)*tc(4,-1)+tc(3,-1)*tc(4,+1)
term3=1.
```

```
do 535 q=(tq+1),tqx
    term3=term3*tcx(q)
535 continue
    term=sgn*term1*term2*term3

    num=num+term

554 continue
553 continue
552 continue
551 continue

return
end

subroutine cont5(gee,num)
c      * contraction of quark-line tensor-amplitudes *

    real gee(4,4),num
    integer id(6,4),q,ih
    real tc(4,-1:1),tcx(6)
    real sgn,term1,term2,term3,term
    real t1(4,-1:1,4),t2(4,-1:1,4,4),t3(4,-1:1,4,4,4)
    real t3g(6,4,4,4),t4g(6,4,4,4,4)
    integer nq(5,-1:1),nv(5,-1:1),tv(6),tq,tqx
    common/tensor/ t1,t2,t3,t3g,t4g
```

```
common/nqnv/ nq,nv,tv,tq,tqx

num=0.

do 551 i1=1,4
    id(nq(1,+1),nv(1,+1))=i1
    id(nq(1,-1),nv(1,-1))=i1
do 552 i2=1,4
    id(nq(2,+1),nv(2,+1))=i2
    id(nq(2,-1),nv(2,-1))=i2
do 553 i3=1,4
    id(nq(3,+1),nv(3,+1))=i3
    id(nq(3,-1),nv(3,-1))=i3
do 554 i4=1,4
    id(nq(4,+1),nv(4,+1))=i4
    id(nq(4,-1),nv(4,-1))=i4
do 555 i5=1,4
    id(nq(5,+1),nv(5,+1))=i5
    id(nq(5,-1),nv(5,-1))=i5

do 530 q=1,tq
do 520 ih=-1,1,2
    if (tv(q).eq.1) tc(q,ih)=t1(q,ih,id(q,1))
    if (tv(q).eq.2) tc(q,ih)=t2(q,ih,id(q,2),id(q,1))
    if (tv(q).eq.3) tc(q,ih)=t3(q,ih,id(q,3),id(q,2),id(q,1))
520 continue
530 continue
do 531 q=(tq+1),txx
```



```
      if (tv(q).eq.3) tcx(q)=t3g(q,id(q,1),id(q,2),id(q,3))
      if (tv(q).eq.4) tcx(q)=t4g(q,id(q,1),id(q,2),id(q,3),
1          id(q,4))
531  continue

      sgn=gee(i1,i1)*gee(i2,i2)*gee(i3,i3)*gee(i4,i4)*gee(i5,i5)
      term1=tc(1,+1)*tc(2,-1)+tc(1,-1)*tc(2,+1)
      term2=tc(3,+1)*tc(4,-1)+tc(3,-1)*tc(4,+1)
      term3=1.
      do 535 q=(tq+1),tqx
          term3=term3*tcx(q)
535  continue

      term=sgn*term1*term2*term3

      num=num+term

555  continue
554  continue
553  continue
552  continue
551  continue

      return
      end

      subroutine fmdr(fm,dr)
```

c        \* fermion no. and direction of quark lines \*

integer fm(4),dr(4)

fm(1)=+1

fm(2)=-1

fm(3)=+1

fm(4)=-1

dr(1)=+1

dr(2)=+1

dr(3)=-1

dr(4)=-1

return

end

subroutine hadmom(trad,p1i,p1f,p2i,p2f)

c        \* initial and final values of hadron mom. \*

real trad,sn,cs

real p1i(4),p1f(4),p2i(4),p2f(4)

sn=sin(trad)

cs=cos(trad)

p1i(1)= 1.0

p1i(2)= 0.0

p1i(3)= 0.0

p1i(4)= 1.0

p1f(1)= 1.0

p1f(2)= sn

p1f(3)= 0.0

p1f(4)= cs

p2i(1)= 1.0

p2i(2)=-0.0

p2i(3)=-0.0

p2i(4)=-1.0

p2f(1)= 1.0

p2f(2)=-sn

p2f(3)=-0.0

p2f(4)=-cs

return

end

subroutine levciv(eps)

c        \* specification of levi-civita tensor \*

real ex,ey,eps(4,4,4,4)

```
logical lg

ex=-1.
ey=1.
do 320 i=1,4
do 320 j=1,4
do 320 k=1,4
do 320 l=1,4
    lg=(i.eq.j).or.(i.eq.k).or.(i.eq.l).or.(j.eq.k).or.
1  (j.eq.l).or.(k.eq.l)

    if (lg) then
        eps(i,j,k,l)=0.
    else
        ex=ex*-1.
        ey=ey*ex
        eps(i,j,k,l)=ey
    end if
320 continue

return
end

subroutine metric(gee)
c      * specification of metric tensor *

real gee(4,4)
```

```

    gee(1,1)= 1.
    gee(2,2)=-1.
    gee(3,3)= 1.
    gee(4,4)=-1.
    do 310 i=1,4
    do 310 j=1,4
        if (i.ne.j) gee(i,j)=0.
310  continue

    return
end

subroutine setp3g(i,q)
c      * three-gluon vertex *

    integer i,q
    integer ng(6,4),sg(6,4),tp
    real pa(5,5),pb(5,4),pi(4,4),pf(4,4)
    common/setup/ pa,pb,pi,pf,tp
    common/ngsg/ ng,sg

    if (i.gt.tp) return

    do 14 j=1,tp
        if (j.eq.ng(q,1)) then
            pa(i,j)=sg(q,1)
        else if (j.eq.ng(q,2)) then

```

```

        pa(i,j)=sg(q,2)
    else if (j.eq.ng(q,3)) then
        pa(i,j)=sg(q,3)
    else
        pa(i,j)=0
    end if
14  continue

do 24 j=1,4
    pb(i,j)=0
24  continue

i=i+1

return

end

subroutine setp4g(i,q)
c      * four-gluon vertex *

integer i,q
integer ng(6,4),sg(6,4),tp
real pa(5,5),pb(5,4),pi(4,4),pf(4,4)
common/setup/ pa,pb,pi,pf,tp
common/ngsg/ ng,sg

if (i.gt.tp) return

```

```
do 14 j=1,tp
  if (j.eq.ng(q,1)) then
    pa(i,j)=sg(q,1)
  else if (j.eq.ng(q,2)) then
    pa(i,j)=sg(q,2)
  else if (j.eq.ng(q,3)) then
    pa(i,j)=sg(q,3)
  else if (j.eq.ng(q,4)) then
    pa(i,j)=sg(q,4)
  else
    pa(i,j)=0
  end if
14 continue

do 24 j=1,4
  pb(i,j)=0
24 continue

i=i+1

return

end

subroutine setupl(i,nqp,q,v)
c      * left vertex *

integer i,nqp,q,v
```

```
integer ng(6,4),sg(6,4),tp
real pa(5,5),pb(5,4),pi(4,4),pf(4,4)
common/setup/ pa,pb,pi,pf,tp
common/ngsg/ ng,sg

if (i.gt.tp) return

do 11 j=1,tp
  if (j.eq.ng(q,v)) then
    pa(i,j)=sg(q,v)
  else if (j.eq.nqp) then
    pa(i,j)=+1
  else
    pa(i,j)=0
  end if
11 continue

do 21 j=1,4
  pb(i,j)=pi(q,j)
21 continue

i=i+1

return
end

subroutine setupr(i,nqp,q,v)
```



c        \* right vertex \*

integer i,nqp,q,v

integer ng(6,4),sg(6,4),tp

real pa(5,5),pb(5,4),pi(4,4),pf(4,4)

common/setup/ pa,pb,pi,pf,tp

common/ngsg/ ng,sg

if (i.gt.tp) return

do 12 j=1,tp

  if (j.eq.ng(q,v)) then

    pa(i,j)=sg(q,v)

  else if (j.eq.nqp) then

    pa(i,j)=-1

  else

    pa(i,j)=0

  end if

12 continue

do 22 j=1,4

  pb(i,j)=-pf(q,j)

22 continue

i=i+1

nqp=nqp+1

```
return
end

subroutine setupm(i,nqp,q,v)
c      * middle vertex *

integer i,nqp,q,v
integer ng(6,4),sg(6,4),tp
real pa(5,5),pb(5,4),pi(4,4),pf(4,4)
common/setup/ pa,pb,pi,pf,tp
common/ngsg/ ng,sg

if (i.gt.tp) return

do 13 j=1,tp
  if (j.eq.ng(q,v)) then
    pa(i,j)=sg(q,v)
  else if (j.eq.nqp) then
    pa(i,j)=-1
  else if (j.eq.(nqp+1)) then
    pa(i,j)=+1
  else
    pa(i,j)=0
  end if
13 continue

do 23 j=1,4
```

```
        pb(i,j)=0
23  continue

        i=i+1
        nqp=nqp+1

        return
    end

    subroutine setupx(i,q)
c      * single vertex *

        integer i,q
        integer ng(6,4),sg(6,4),tp
        real pa(5,5),pb(5,4),pi(4,4),pf(4,4)
        common/setup/ pa,pb,pi,pf,tp
        common/ngsg/ ng,sg

        if (i.gt.tp) return

        do 10 j=1,tp
            if (j.eq.ng(q,1)) then
                pa(i,j)=sg(q,1)
            else
                pa(i,j)=0
            end if
10  continue
```

```
do 20 j=1,4
    pb(i,j)=pi(q,j)-pf(q,j)
20  continue

i=i+1

return

end

subroutine vecamp(trad,az)
c      * specification of quark-line vector-amplitudes *

real trad,s,c
real az(-1:1,-1:1,4)

s=sin(trad/2.)
c=cos(trad/2.)

az(+1,+1,1)= c
az(+1,+1,2)= s
az(+1,+1,3)= s
az(+1,+1,4)= c

az(+1,-1,1)= c
az(+1,-1,2)= s
az(+1,-1,3)=-s
az(+1,-1,4)= c
```

$az(-1,+1,1) = c$

$az(-1,+1,2) = -s$

$az(-1,+1,3) = s$

$az(-1,+1,4) = -c$

$az(-1,-1,1) = c$

$az(-1,-1,2) = -s$

$az(-1,-1,3) = -s$

$az(-1,-1,4) = -c$

return

end

## REFERENCES

- [1] D. Sivers, S. J. Brodsky and R. Blankenbecler, Phys. Rep. 23C, No.1 (1976)
- [2] G. P. Lepage and S. J. Brodsky, Phys. Rev. D22, 2157 (1980)
- [3] A. H. Mueller, Phys. Rep. 73, No. 4 (1981)
- [4] P. V. Landshoff, Phys. Rev. D10, 1024 (1974)
- [5] G. R. Farrar and C. C. Wu, Nucl. Phys. B85, 50 (1975)
- [6] J. F. Gunion, S. J. Brodsky and R. Blankenbecler, Phys. Rev. D8, 287 (1973)
- [7] P. V. Landshoff and J. C. Polkinghorne, Phys. Lett. 44B, 293 (1973)
- [8] K. A. Jenkins *et. al.*, Phys. Rev. D21, 2445 (1980)
- [9] B. Schrempp and F. Schrempp, Phys. Lett. 55B, 303 (1975)
- [10] A. W. Hendry, Phys. Rev. D10, 2300 (1974)
- [11] V. Barger, F. Halzen and J. Luthe, Phys. Lett. 42B, 428 (1972)
- [12] R. Almas *et. al.*, Phys. Lett. 93B, 199 (1980)
- [13] D. P. Owen *et. al.*, Phys. Rev. 181, 1974 (1978)
- [14] J. L. Stone *et. al.*, Nucl. Phys. B143,1 (1978)
- [15] W. F. Baker *et. al.*, Phys. Rev. Lett. 47, 1683 (1981)
- [16] J. L. Hartmann *et. al.*, Phys. Rev. Lett. 39, 975 (1977)
- [17] S. Connetti *et. al.*, Phys. Rev. Lett. 41, 924 (1978)
- [18] H. De Kerret *et. al.*, Phys. Lett. 68B, 374 (1977)
- [19] A. Donnachie and P.V. Landshoff, Z. Phys. C2, 55 (1979)
- [20] P. Cornillon *et. al.*, Phys. Rev. Lett. 30, 403 (1973)
- [21] G. R. Farrar and G. C. Fox, Nucl. Phys. B167, 205 (1980)